SLAC-R-805

A Search for the Rare Decay B->tau+tau- at the BaBar Experiment

Christopher Thomas Potter

Stanford Linear Accelerator Center
Stanford University
Stanford, CA 94309

SLAC-Report-805

Prepared for the Department of Energy
under contract number DE-AC02-76SF00515

Printed in the United States of America. Available from the National Technical Information Service, U.S. Department of Commerce, 5285 Port Royal Road, Springfield, VA 22161.

This document, and the material and data contained therein, was developed under sponsorship of the United States Government. Neither the United States nor the Department of Energy, nor the Leland Stanford Junior University, nor their employees, nor their respective contractors, subcontractors, or their employees, makes an warranty, express or implied, or assumes any liability of responsibility for accuracy, completeness or usefulness of any information, apparatus, product or process disclosed, or represents that its use will not infringe privately owned rights. Mention of any product, its manufacturer, or suppliers shall not, nor is it intended to, imply approval, disapproval, or fitness of any particular use. A royalty-free, nonexclusive right to use and disseminate same of whatsoever, is expressly reserved to the United States and the University.

A SEARCH FOR THE RARE DECAY $B^0 \to \tau^+\tau^-$ AT THE BABAR EXPERIMENT

by

CHRISTOPHER THOMAS POTTER

A DISSERTATION

Presented to the Department of Physics
and the Graduate School of the University of Oregon
in partial fulfillment of the requirements
for the degree of
Doctor of Philosophy

June 2005

A Search for the Rare Decay $B^0 \to \tau^+\tau^-$ at the Babar Experiment

Copyright June 2005

by

Christopher Thomas Potter

An Abstract of the Dissertation of

Christopher Thomas Potter for the degree of Doctor of Philosophy

in the Department of Physics to be taken June 2005

Title: A SEARCH FOR THE RARE DECAY $B^0 \rightarrow \tau^+\tau^-$ AT THE BABAR EXPERIMENT

Approved: ______________________________

Dr. James Brau

The Standard Model of particle physics predicts that the branching ratio for the rare decay $B^0 \rightarrow \tau^+\tau^-$ is 3.1×10^{-8}, though untested models which could supersede it predict large enhancements. This dissertation describes the search for this rare decay in 210.4 fb^{-1} of $B^0\bar{B}^0$ data collected at the $\Upsilon(4S)$ resonance in the Babar detector at the Stanford Linear Accelerator Center. In the analysis, one neutral B meson is fully reconstructed in a hadronic mode and recoil events which are consistent with each tau decaying in a mode $\tau \rightarrow \pi\nu, \rho\nu$, or $l\nu\bar{\nu}$ are selected. There is no evidence for signal. The result is consistent with a downward fluctuation by 1.1 statistical standard deviations of the expected Standard Model background. Taking the expected background, the number of observed events and the expected statistical and systematic errors into account yields 2.7×10^{-3} as the upper limit for $B^0 \rightarrow \tau^+\tau^-$ at the 90% confidence level.

ACKNOWLEDGEMENTS

I gratefully acknowledge the advice and instruction I received from my advisor, Professor David Strom, and from Professor Jim Brau, the principal investigator in the University of Oregon HEP research group. I further acknowledge all members of the Oregon HEP group for providing a very positive work environment. I also acknowledge the excellent training I received while working at the Babar experiment with colleagues in the Leptonic B&c analysis working group. I gratefully acknowledge the Babar Collaboration members and the Stanford Linear Accelerator Center staff who work on PEPII and the SLAC linac. Finally, I gratefully acknowledge the US Department of Energy Office of Science, without whose generous support this research would not have been possible.

TABLE OF CONTENTS

Chapter Page

1. **INTRODUCTION** 1

    1.1. **New Physics in Dilepton Neutral Meson Decays** 1
    1.2. **CP Violation and the Babar Detector** 4
    1.3. **$\mathbf{B^0} \rightarrow \tau^+\tau^-$ Background at Babar** 8
    1.4. **Outline of the Dissertation** 11

2. $B^0 \rightarrow \tau^+\tau^-$ **THEORY** 13

    2.1. **Introduction** 13
    2.2. **The Standard Model** 15
    2.3. **The Two-Higgs-Doublet Model** 29
    2.4. **Supersymmetry** 35
    2.5. **Leptoquarks** 48

3. **THE BABAR DETECTOR** 54

    3.1. **Introduction** 54
    3.2. **Charged Particle Tracking** 64
    3.3. **Electromagnetic and Hadronic Calorimetry** 73
    3.4. **Particle Identification** 80
    3.5. **Global Detector Operation** 84

4. **SIMULATION AT BABAR** 90

    4.1. **Introduction** 90
    4.2. **Primary Event Simulation** 92
    4.3. **Detector Physics Simulation** 119

5. $B^0 \rightarrow \tau^+\tau^-$ **SELECTION** 129

    5.1. **Data and Simulation Samples** 129
    5.2. **Particle Candidate Selection** 133

5.3. **Tag B Selection** 139
5.4. **Signal B Selection** 145
5.5. **The Neural Network** 157
5.6. **Data Control Sample** 164

6. **STATISTICAL ANALYSIS** 168

6.1. **Analysis Chain Efficiencies** 169
6.2. **Limit Setting Procedure** 174
6.3. **Systematic Errors** 176
6.4. **Upper Limit Optimization** 182

7. **RESULTS** 186

7.1. **Blinded Expectation and Unblinded Results** 186
7.2. **Implications for Theoretical Models** 189
7.3. **Conclusion** 192

APPENDICES 195

A. **DISTRIBUTIONS BEFORE AND AFTER PRESELECTION** . 195

B. **$\mathbf{m_{ES}}$ FITS FOR EXTRACTING EFFICIENCIES** 210

BIBLIOGRAPHY 219

LIST OF FIGURES

Figure Page

2.1 Standard Model box (middle), penguin (top left and right) and self-energy (bottom left and right) processes responsible for $B^0 \to \tau^+\tau^-$. 27

2.2 Dominant 2HDM processes responsible for $B^0 \to \tau^+\tau^-$. These are similar to the SM diagrams but with a $qtW^\pm$ ($q = b, d$) vertex replaced by a $qtH^\pm$ or $qtG^\pm$ vertex. 33

2.3 Branching ratio $\mathcal{B}^{2HDM}(B^0 \to \tau^+\tau^-)$ plotted against $m_{H^\pm}$ (left) and against $\tan\beta$ (right) in the large $\tan\beta$ limit. The SM value is shown in bold. 34

2.4 Dominant MSSM processes responsible for $B^0 \to \tau^+\tau^-$. At left is the penguin with gluino exchange with flavor changing mass insertion. At right is the penguin with chargino exchange. 46

2.5 Vector (left) and scalar (right) leptoquark processes which mediate $B^0 \to \tau^+\tau^-$. The quark and lepton chirality labels have been suppressed. . . . 51

2.6 Branching ratio $\mathcal{B}^{LQ}(B^0 \to \tau^+\tau^-)$ plotted against m_{V_0} (left) and against $\lambda_{31R}^{V_0}\lambda_{33L}^{V_0}$ (right). The SM value is shown in bold. 53

3.1 The linear accelerator and PEPII storage ring at SLAC. 55

3.2 Side view of the Babar detector. 59

3.3 End view of the Babar detector. 60

3.4 Longitudinal section of the Silicon Vertex Tracker.. 65

3.5 Longitudinal section of the Drift Chamber. 69

3.6 Track parameter resolutions obtained from two halves of a cosmic ray event [1]. 71

3.7 Electromagnetic calorimeter in longitudinal section. 73

3.8 The flux return steel barrel (left) and endcaps (right). 78

3.9 The Detector for Internally Reflected Cherenkov radiation.. 80

3.10 Measurement performance for the photon energy in the EMC (a), Cherenkov angle and timing in the DIRC (b) and dE/dx in the DCH (c) [1]. . . . 83

3.11 Schematic diagram of trigger, data acquisition, event reconstruction and event logging. 84

4.1 The three stages of simulation at Babar. 91

4.2 Feynman diagrams for the two dominant classes of tau decay. Leptonic decays ($\tau \to e\nu_e\nu_\tau$ and $\tau \to \mu\nu_\mu\nu_\tau$) account for approximately 35.2% of all tau decays, while hadronic decays of the type depicted ($\tau \to \pi\nu_\tau$, $\tau \to \rho\nu_\tau$, $\tau \to a_1\nu_\tau$, $\tau \to K\nu_\tau$ and $\tau \to K^\star\nu_\tau$) account for approximately 57.2% of all tau decays. 98

4.3 Tau momentum in the B frame with EvtGen (solid line) and Tauola (error bars). Clockwise from top left are $\tau\tau \to ee\nu_e\bar{\nu}_e\nu_\tau\bar{\nu}_\tau$, $\tau\tau \to \mu\mu\nu_\mu\bar{\nu}_\mu\nu_\tau\bar{\nu}_\tau$, $\tau\tau \to \rho\rho\nu_\tau\bar{\nu}_\tau$ and $\tau\tau \to \pi\pi\nu_\tau\bar{\nu}_\tau$. For the ρ mode, the EvtGen results using TAUHADNU and TAUVECTORNU are superimposed. 106

4.4 Cosine of the angle between tau daughters in the B frame with EvtGen (solid line) and Tauola (error bars). Clockwise from top left are $\tau\tau \to ee\nu_e\bar{\nu}_e\nu_\tau\bar{\nu}_\tau$, $\tau\tau \to \mu\mu\nu_\mu\bar{\nu}_\mu\nu_\tau\bar{\nu}_\tau$, $\tau\tau \to \rho\rho\nu_\tau\bar{\nu}_\tau$ and $\tau\tau \to \pi\pi\nu_\tau\bar{\nu}_\tau$. For the ρ mode, the EvtGen results using TAUHADNU and TAUVECTORNU are superimposed. 106

4.5 Tau momentum in the B frame with EvtGen (solid line) and Tauola (error bars). From top to bottom are $\tau\tau \to e\pi\nu_e\nu_\tau\bar{\nu}_\tau$, $\tau\tau \to e\rho\nu_e\nu_\tau\bar{\nu}_\tau$ and $\tau\tau \to \pi\rho\nu_\tau\bar{\nu}_\tau$. Charge conjugate modes are horizontally opposed. Charge conjugate modes are horizontally opposed. For the ρ mode, the EvtGen results using TAUHADNU and TAUVECTORNU are superimposed. . . 107

4.6 Cosine of the angle between tau daughters in the B frame with EvtGen (solid line) and Tauola (error bars). From top to bottom are $\tau\tau \to e\pi\nu_e\nu_\tau\bar{\nu}_\tau$, $\tau\tau \to e\rho\nu_e\nu_\tau\bar{\nu}_\tau$ and $\tau\tau \to \pi\rho\nu_\tau\bar{\nu}_\tau$. Charge conjugate modes are horizontally opposed. For the ρ mode, the EvtGen results using TAUHADNU and TAUVECTORNU are superimposed. 107

4.7 The τ^+ momentum plotted against the τ^- momentum in EvtGen with the TAUHADNU model for the ρ mode. Clockwise from top left are $\tau\tau \to ee\nu_e\bar{\nu}_e\nu_\tau\bar{\nu}_\tau$, $\tau\tau \to \mu\mu\nu_\mu\bar{\nu}_\mu\nu_\tau\bar{\nu}_\tau$, $\tau\tau \to \rho\rho\nu_\tau\bar{\nu}_\tau$ and $\tau\tau \to \pi\pi\nu_\tau\bar{\nu}_\tau$. . . 108

4.8 The τ^+ momentum plotted against the τ^- momentum in Tauola. Clockwise from top left are $\tau\tau \to ee\nu_e\bar{\nu}_e\nu_\tau\bar{\nu}_\tau$, $\tau\tau \to \mu\mu\nu_\mu\bar{\nu}_\mu\nu_\tau\bar{\nu}_\tau$, $\tau\tau \to \rho\rho\nu_\tau\bar{\nu}_\tau$ and $\tau\tau \to \pi\pi\nu_\tau\bar{\nu}_\tau$. 108

4.9 Feynman diagrams for four classes of B decay. Leptonic decays are rare in the Standard Model and have not yet been observed. The internal and external hadronic diagrams add constructively for two-body decay modes with branching ratios of order 2%. The semileptonic decay branching ratio for the neutral B is approximately 24%. Most B decays are considerably more complex, with many gluons connecting internal and external quarks. 109

5.1 At left, the reconstructed mass of the seed D or $D^\star$ used in reconstructing the tag B. At right, the ΔE of the tag B. Only the *peaking components* of data (dots), generic neutral B (solid) and the signal cocktail (dashed) are plotted. 141

5.2 At left, Runs 1-4 data (dots) and from top to bottom generic neutral B, `BpBm`, `ccbar`, `uds` and `e+e- -> tau+tau-` Monte carlo simulation samples (solids). The `e+e- -> tau+tau-` component is not large enough to be visible. At right, a four Argus fit to the m_{ES} data distribution. 144

5.3 At left, the very loose track multiplicity on the signal side. At right, the loose photon muliplicity on the signal side. Only the *peaking components* of data (dots), generic neutral B (solid) and the signal cocktail (dashed) are plotted. The generic neutral B histograms are normalized to the data histograms. 146

5.4 Tag yield in the semiexclusive sample after preselection. Clockwise from top left are the generic neutral B, data, signal generic, and signal cocktail samples 147

5.5 Clockwise from top left, the net loose track charge on the signal side, loose kaon, default K_S and tight K_L multiplicity on the signal side after all preceding requirements in the analysis chain have been imposed. Only the *peaking components* of data (dots), generic neutral B (solid) and the signal cocktail (dashed) are plotted. The dark shaded solid (here and in subsequent plots) is the component of the neutral B containing a truth verified K_L. 149

5.6 At top left, the remaining neutral energy after neutral pion reconstruction (blind). At top right, the ditau reconstruction mode (blind). At bottom left, the mass of the rho candidate. At bottom right, the mass of the K_S candidate in the extra K_S control sample. Only the *peaking components* of data (dots), `B0B0bar` (solid) are plotted. The dark shaded histogram (here and in subsequent control sample plots) indicates events in which the K_S reconstruction is verified with Monte Carlo truth. 151

5.7 Candidate tau daughter pair momenta by mode in the signal (top) and background (bottom) cocktail Monte Carlo sample. All tag B and background rejection requirements are applied. For signal, the signal side mode reconstruction is required to be correct using Monte Carlo truth. 155

5.8 The selection for $B \to \tau^+\tau^-$. At left, the m_{ES} distribution in Monte Carlo simulation. At right, the neural network output in Monte Carlo simulation. Only the *peaking components* of generic neutral B (solid) and the signal cocktail (dashed) are plotted. For the unblinded version of these plots, see Figure 7.2. 156

5.9 Inputs to the neural network for the $B \to \tau^+\tau^-$ selection. Clockwise from top left are the signal multiplicity mode, cosine subtended by tau daughter candidate momenta, remaining neutral energy and magnitude of the tau daughter candidate momentum. Only the *peaking components* of data (dots), generic neutral B (solid) and the signal cocktail (dashed) are plotted. or the unblinded version of these plots, see Figure 7.3. 156

5.10 The neural network topology. From left to right are input, hidden and output units. The activation level a_i for each node i is displayed. 158

5.11 The minimum RMSE plotted against number of training cycles. The cumulative miminum is 0.474054, obtained at cycle 75416. 162

5.12 Performance of the neural network in the cocktail (top) and generic (bottom) samples. All preceding requirements in the analysis chain are imposed. No background subtraction is performed. 163

5.13 The selection for the extra K_S control sample. At left, the m_{ES} distributions in data. At right, the neural network output in data and Monte Carlo samples. Only the *peaking components* of data (dots), `B0B0bar` (solid) and the signal cocktail (dashed) are plotted. 167

5.14 Inputs to the neural network for the extra K_S control sample. Clockwise from top left are the signal multiplicity mode, cosine subtended by tau daughter candidate momenta, remaining neutral energy and magnitude of the tau daughter candidate momentum. Only the *peaking components* of data (dots), generic neutral B (solid) and the signal cocktail (dashed) are plotted. 167

6.1 The expected 90% upper limit plotted against the error on the background expectation (in units of the nominal error, 37.2 events). Both the tag B yield error and the signal efficiency errors are varied. 181

6.2 Contour plots of the expected 90% confidence level upper limit R_{ul}^{90} plotted versus mode subset number m. Mode subsets $m = 9, 27, 43$ and 59 generate $R_{ul}^{90} < 4 \times 10^{-3}$. The first contours are rejected as marking statistical outliers. 183

6.3 Contour plots of the expected 90% confidence level upper limit R_{ul}^{90} plotted versus cut values for lower bound for the neural network output (left) and upper bound for unassigned photon energy (right). The first contours are rejected as marking statistical outliers. 184

7.1 The distribution of the 90% confidence level upper limit in 10^5 Poisson trials with mean 281 assuming zero signal events. 187

7.2 The selection for $B \to \tau^+\tau^-$. At left, the m_{ES} distribution in Monte Carlo simulation. At right, the neural network output in Monte Carlo simulation. Only the *peaking components* of generic neutral B (solid) and the signal cocktail (dashed) are plotted. The mode selection has not been applied at right. 191

7.3 Inputs to the neural network for the $B \to \tau^+\tau^-$ selection. Clockwise from top left are the signal multiplicity mode, cosine subtended by tau daughter candidate momenta, remaining neutral energy and magnitude of the tau daughter candidate momentum. Only the *peaking components* of data (dots), generic neutral B (solid) and the signal cocktail (dashed) are plotted. 191

7.4 The regions of the $\tan\beta - m_{H^+}$ plane which are excluded at the 90% confidence level by the upper limit measurements on $\mathcal{B}(B^0 \to \mu^+\mu^-)$ and $\mathcal{B}(B^0 \to \tau^+\tau^-)$. 193

7.5 The regions of the $m_{LQ} - \lambda_{31}^{LQ}\lambda_{33}^{LQ}$ plane which are excluded at the 90% confidence level by the upper limit measurements on $\mathcal{B}(B^0 \to \tau^+\tau^-)$. . . . 193

LIST OF APPENDIX FIGURES

Figure Page

A.1 Tag B ΔE before (left) and after (right) preselection. Only the *peaking components* of data (error bars) and generic neutral B (solid) and signal cocktail (dashed) have been plotted. 197

A.2 Tag B ΔE after preselection for Runs 1-3 (left) and Run 4 (right). Only the *peaking components* of data (error bars) and generic neutral B (solid) and signal cocktail (dashed) have been plotted. 197

A.3 The cosine of the angle between the tag B and the rest of the event before (left) and after (right) preselection. Only the *peaking components* of data (error bars) and generic neutral B (solid) and signal cocktail (dashed) have been plotted. 198

A.4 The cosine of the angle between the tag B and the rest of the event after preselection for Runs 1-3 (left) and Run 4 (right). Only the *peaking components* of data (error bars) and generic neutral B (solid) and signal cocktail (dashed) have been plotted. 198

A.5 The mass of the D or $D^\star$ used for reconstructing the tag B before (left) and after (right) preselection. Only the *peaking components* of data (error bars) and generic neutral B (solid) and signal cocktail (dashed) have been plotted. 199

A.6 The mass of the D or $D^\star$ used for reconstructing the tag B after preselection for Runs 1-3 (left) and Run 4 (right). Only the *peaking components* of data (error bars) and generic neutral B (solid) and signal cocktail (dashed) have been plotted. 199

A.7 The signal side energy in all `GoodPhotonsLoose` candidates before (left) and after (right) preselection. Only the *peaking components* of data (error bars) and generic neutral B (solid) and signal cocktail (dashed) have been plotted. 200

A.8 The signal side energy in all `GoodPhotonsLoose` candidates after preselection for Runs 1-3 (left) and Run 4 (right). Only the *peaking components* of data (error bars) and generic neutral B (solid) and signal cocktail (dashed) have been plotted. 200

A.9 The signal side `GoodPhotonsLoose` multiplicity before (left) and after (right) preselection. Only the *peaking components* of data (error bars) and generic neutral B (solid) and signal cocktail (dashed) have been plotted. 201

A.10 The signal side `GoodPhotonsLoose` multiplicity after preselection for Runs 1-3 (left) and Run 4 (right). Only the *peaking components* of data (error bars) and generic neutral B (solid) and signal cocktail (dashed) have been plotted. 201

A.11 The signal side energy in the `pi0DefaultMass` candidates before (left) and after (right) preselection. Only the *peaking components* of data (error bars) and generic neutral B (solid) and signal cocktail (dashed) have been plotted. 202

A.12 The signal side energy in the `pi0DefaultMass` candidates after preselection for Runs 1-3 (left) and Run 4 (right). Only the *peaking components* of data (error bars) and generic neutral B (solid) and signal cocktail (dashed) have been plotted. 202

A.13 The signal side `pi0DefaultMass` multiplicity before (left) and after (right) preselection. Only the *peaking components* of data (error bars) and generic neutral B (solid) and signal cocktail (dashed) have been plotted. 203

A.14 The signal side `pi0DefaultMass` multiplicity after preselection for Runs 1-3 (left) and Run 4 (right). Only the *peaking components* of data (error bars) and generic neutral B (solid) and signal cocktail (dashed) have been plotted. 203

A.15 The signal side `GoodTracksVeryLoose` multiplicity before (left) and after (right) preselection. Only the *peaking components* of data (error bars) and generic neutral B (solid) and signal cocktail (dashed) have been plotted. 204

A.16 The signal side `GoodTracksVeryLoose` multiplicity after preselection for Runs 1-3 (left) and Run 4 (right). Only the *peaking components* of data (error bars) and generic neutral B (solid) and signal cocktail (dashed) have been plotted. 204

A.17 The signal side `GoodTracksLoose` multiplicity before (left) and after (right) preselection. Only the *peaking components* of data (error bars) and generic neutral B (solid) and signal cocktail (dashed) have been plotted. 205

A.18 The signal side `GoodTracksLoose` multiplicity after preselection for Runs 1-3 (left) and Run 4 (right). Only the *peaking components* of data (error bars) and generic neutral B (solid) and signal cocktail (dashed) have been plotted. 205

A.19 The total signal side charge in `GoodTracksLoose` before (left) and after (right) preselection. Only the *peaking components* of data (error bars) and generic neutral B (solid) and signal cocktail (dashed) have been plotted. 206

A.20 The total signal side charge in `GoodTracksLoose` after preselection for Runs 1-3 (left) and Run 4 (right). Only the *peaking components* of data (error bars) and generic neutral B (solid) and signal cocktail (dashed) have been plotted. 206

A.21 The signal side `eMicroTight` multiplicity before (left) and after (right) preselection. Only the *peaking components* of data (error bars) and generic neutral B (solid) and signal cocktail (dashed) have been plotted. 207

A.22 The signal side `eMicroTight` multiplicity after preselection for Runs 1-3 (left) and Run 4 (right). Only the *peaking components* of data (error bars) and generic neutral B (solid) and signal cocktail (dashed) have been plotted.207

A.23 The signal side `muMicroTight` multiplicity before (left) and after (right) preselection. Only the *peaking components* of data (error bars) and generic neutral B (solid) and signal cocktail (dashed) have been plotted. 208

A.24 The signal side `muMicroTight` multiplicity after preselection for Runs 1-3 (left) and Run 4 (right). Only the *peaking components* of data (error bars) and generic neutral B (solid) and signal cocktail (dashed) have been plotted. 208

A.25 The signal side `KMicroLoose` multiplicity before (left) and after (right) preselection. Only the *peaking components* of data (error bars) and generic neutral B (solid) and signal cocktail (dashed) have been plotted. 209

A.26 The signal side `KMicroLoose` multiplicity after preselection for Runs 1-3 (left) and Run 4 (right). Only the *peaking components* of data (error bars) and generic neutral B (solid) and signal cocktail (dashed) have been plotted. 209

B.1 Cumulative $Q_{GTL} = 0$ 210

B.2 Exclusive $Q_{GTL} = 0$ 211

B.3 Cumulative $N_{GTL} = 2$ 211

B.4 Exclusive $N_{GTL} = 2$ 212

B.5 Cumulative $N_{KML} = 0$ 212

B.6 Exclusive $N_{KML} = 0$ 213

B.7 Cumulative $N_{KsD} = 0$ 213

B.8 Exclusive $N_{KsD} = 0$ 214

B.9 Cumulative $N_{KlET} = 0$ 214

B.10 Exclusive $N_{KlET} = 0$ 215

B.11 Cumulative $E_{GPL} - E_{pDM} < 0.11$ GeV 215

B.12 Exclusive $E_{GPL} - E_{pDM} < 0.11$ GeV 216

B.13 Cumulative mode subset M_{43} 216

B.14 Exclusive mode subset M_{43} 217

B.15 Cumulative $NN > 0.52$ 217

B.16 Exclusive $NN > 0.52$ 218

LIST OF TABLES

Table Page

1.1 Branching ratio measurements of FCNC- and helicity-suppressed neutral pseudoscalar meson decays to dilepton pairs from [2] unless otherwise indicated. Limits are 90% confidence limits. An x indicates that the decay is kinematically forbidden while a - indicates that no measurement has been reported. All three B^0 measurements were made at Babar. . . 2

1.2 The 90% confidence intervals for the proportions of background by type remaining in the `B0B0bar generic` simulation sample after all $B^0 \to \tau^+\tau^-$ requirements are imposed. 9

1.3 Typical background modes to a $B^0 \to \tau^+\tau^-$ analysis and their branching ratios. Kinematic background is rejected either by rejecting high momentum candidates or by using a neural network analysis. 11

2.1 The charge and spin of fermion (left) and boson (right) fields in the SM Lagrangian. The W, Z and A fields are generated by the electroweak group ($U(1) \times SU(2)$) generators, and the eight fields G_k are generated by the strong interaction group $SU(3)$ generators. 16

2.2 The interactions allowed in the Standard Model. 25

2.3 The minimal additional field content of the MSSM, excluding the Higgs sector. These are the superpartners of the leptons, quarks and gauge vectors from Table 2.1 (which are also included in the MSSM). 41

2.4 The MSSM Higgs sector. 42

2.5 The spin J, fermion number $F = 3B + L$ and charge Q for leptoquarks allowed for renormalizable SM gauge group invariant interactions. 50

2.6 Leptoquark couplings which enter the Wilson coefficients for $B^0 \to \tau^+\tau^-$. 52

3.1 Cross sections, production rates (for $\mathcal{L} = 3 \times 10^{33}$ cm^{-2} s^{-1}) and trigger efficiencies at the $\Upsilon(4S)$ resonance [1] [3]. 58

3.2 Masses, lifetimes and detection method for particles typically detected in Babar. Longlived particles (above) are directly detected, while shortlived particles (below) are detected by their decay products. 64

3.3 Composition of the L3 Physics Accept sample at $\mathcal{L} = 2.6 \times 10^{33}$ cm^{-2} s^{-1} [1]. 88

4.1 Particle properties used by EvtGen for a few select particles. Taken from the EvtGen evt.pdl file. 93

4.2 The complete list of tau decay modes simulated by EvtGen together with their branching ratios and decay models. The branching ratios sum to unity. The parameters in the TAUHADNU decay model are β, the ρ mass and width, the ρ' mass and width, and the a_1 mass and width. The branching ratios in brackets () signify that the models for $\tau \to \rho\nu_\tau$ and $\tau \to a_1\nu_\tau$ were changed from TAUVECTORNU to TAUHADNU between simulation production cycles. Taken from the EvtGen DECAY.DEC file. 104

4.3 Above, a select list of semileptonic $\bar{B}^0$ decay modes simulated by EvtGen together with their branching ratios and decay models. The three parameters in the HQET decay model are the form factor slope ρ_A^2 and form factor ratios R_1 and R_2, with values taken from CLEO measurements [4]. Below, a select list of hadronic $\bar{B}^0$ decay modes simulated by EvtGen together with their branching ratios and decay models. The parameters in the SVV_HELAMP decay models are the magnitude and phase of the amplitudes in the helicity state expansion of the D. Taken from the EvtGen DECAY.DEC file. 114

4.4 The complete list of hadronic $D^\star$ decay modes simulated by EvtGen together with their branching ratios and decay models. The branching ratios sum to unity. Taken from the EvtGen DECAY.DEC file. 117

4.5 Above, a select list of hadronic D^+ decay modes with one kaon in the final state simulated by EvtGen together with their branching ratios and decay models. Below, a select list of hadronic D^0 decay modes with one kaon in the final state simulated by EvtGen together with their branching ratios and decay models. The branching ratios sum to $< 77.525\%$. Taken from the EvtGen DECAY.DEC file. 120

4.6 The `Construct` method for the `BgsDchFullModel` class in Bogus. This method defines the geometry for the DCH in GEANT4. The code has been simplified for ease of reading. 127

5.1 Data samples used in this analysis. Runs 1-4 correspond to data taken from startup in 1999 to summer shutdown in 2004. The effective cross section is obtained from the B count to luminosity ratio. 130

5.2 Signal and generic background Monte Carlo simulation samples from the `BSemiExcl` skim used in this analysis. Cross sections are obtained from [3]. The Standard Model expectation $\mathcal{B}^{SM}(B^0 \rightarrow \tau^+\tau^-) = 3.1 \times 10^{-8}$ is assumed. 133

5.3 Cuts used by the selectors employed in this analysis. For comparison, the cuts used by the selector with different criteria are also listed. 135

5.4 At top, the prescribed signal and background cocktail tag B decays $B^0 \rightarrow D^{(\star)}x$. At bottom, the decay modes reconstructed. 140

5.5 Branching ratio, signal mode requirements, reconstruction efficiencies and sample composition with respect to all tau pair decay modes in the signal cocktail. The composition is the fraction of events reconstructed in a given mode which are truth verified to be that mode. All requirements are imposed except the neural network selection. 152

5.6 The inputs for the neural network and their scale maps. The scale maps faciliatate training by mapping the inputs to the unit interval 157

5.7 Cumulative yields and efficiencies for the extra K_S control sample in data and Monte Carlo simulation. Here E_{res} is the residual neutral energy $E_{GPL} - E_{pDM}$. The preselection requires four or fewer loose signal side photons and *four* very loose signal side tracks. 165

6.1 Cumulative yields and efficiencies (in %) for the analysis chain in the Monte Carlo and data samples. The statistical error is added in quadrature with the fit uncertainty. For the unblinded version, see Table 7.3. . 171

6.2 Exclusive yields and efficiencies (in %) for the analysis chain in the Monte Carlo and data samples. The statistical error is added in quadrature with the fit uncertainty. 171

6.3 Cumulative survival fraction $y_i \equiv N_i/N_0$ and purities p_i (in %) in the data and background samples. The statistical error is added in quadrature with the fit uncertainty. For the unblinded version, see Table 7.4 171

6.4 Cumulative yields and efficiencies for the analysis chain in the signal samples. The statistical error is added in quadrature with the fit uncertainty. 172

6.5 Exclusive yields and efficiencies for the analysis chain in the signal samples. The statistical error is added in quadrature with the fit uncertainty. . . 172

6.6 Cumulative survival fraction $y_i \equiv N_i/N_0$ and purities p_i in the signal samples. The statistical error is added in quadrature with the fit uncertainty. 172

6.7 Relative systematic errors δ_ϵ/ϵ (in %) for the signal cocktail efficiency, signal generic efficiency and generic neutral B efficiency. Column three indicates the larger of the two signal systematic errors. 177

7.1 The upper limit R^{90}_{ul} for a 99.7% coverage range of outcomes n_{obs}. The number of trial experiments for each result is 10^5. The background expectation is obtained from the data preselection yield and the background efficiency from Table 6.1. The signal efficiency is obtained from Table 6.4. Systematic errors, which include simulation sample statistical error, are taken from Table 6.7. 188

7.2 The signal efficiency, expected background and observed number of events by signal mode. The errors are statistical and fit error added in quadrature. The systematic errors are not included. 190

7.3 Unblinded cumulative yields and efficiencies (in %) for the analysis chain in the Monte Carlo and data samples. E_{res} is the residual neutral energy $E_{GPL} - E_{pDM}$ The statistical error is added in quadrature with the fit uncertainty. The systematic errors are not included. Note in particular that the $3\sigma^{stat+fit}$ discrepancy after applying the residual energy requirement is well below $1\sigma^{stat+syst}$. 190

7.4 Unblinded survival fraction $y_i \equiv N_i/N_0$ and purities p_i (in %) for the analysis chain in the Monte Carlo and data samples. E_{res} is the residual neutral energy $E_{GPL} - E_{pDM}$ The statistical error is added in quadrature with the fit uncertainty. The systematic errors are not included. 190

Chapter 1

INTRODUCTION

1.1. New Physics in Dilepton Neutral Meson Decays

The search for new physics in neutral pseudoscalar meson decays to a lepton pair has a hallowed history. The charm quark was discovered by direct production in 1974 [7, 8], but its possible existence had been inferred four years earlier through its effect on the neutral meson decay $K_L \to \mu^+\mu^-$ [9]. Do undiscovered particles from new models of particle physics alter the expected rate for $B^0 \to \tau^+\tau^-$?

See Table 1.1 for the measured branching ratios for neutral meson decays to a lepton pair. These decays are examples of flavor changing neutral processes in which the final state flavor quantum number is different than the initial state flavor, and they are mediated by *flavor changing neutral currents* (FCNCs). These processes can proceed in the Standard Model (SM) only at higher order in perturbation theory and are therefore characterized by low branching ratios. Discovery has only been claimed for the decays $K_L \to e^+e^-$ and $K_L \to \mu^+\mu^-$. In all other kinematically allowed neutral pseudoscalar meson decays to a lepton pair, only upper limits on the branching ratios have been established. The K_S decays to a lepton pair violate CP conservation (see the following section) and are therefore even further suppressed.

Meson	e^+e^-	$\mu^+\mu^-$	$\tau^+\tau^-$	$\nu\bar{\nu}$
K_S	$< 1.4 \times 10^{-7}$	$< 3.2 \times 10^{-7}$	x	-
K_L	$(9^{+6}_{-4}) \times 10^{-12}$	$(7.27 \pm 0.14) \times 10^{-9}$	x	-
D^0	$< 6.2 \times 10^{-6}$	$< 4.1 \times 10^{-6}$	x	-
B^0	$< 6.1 \times 10^{-8}$ [5]	$< 8.3 \times 10^{-8}$ [5]	-	$< 2.2 \times 10^{-4}$ [6]

Table 1.1: Branching ratio measurements of FCNC- and helicity-suppressed neutral pseudoscalar meson decays to dilepton pairs from [2] unless otherwise indicated. Limits are 90% confidence limits. An x indicates that the decay is kinematically forbidden while a - indicates that no measurement has been reported. All three B^0 measurements were made at Babar.

In addition to FCNC suppression, neutral pseudoscalar decays to a lepton pair are also suppressed by kinematic constraints. A spin zero meson decay to spin 1/2 fermions must produce fermions in the same helicity eigenstate: either both are lefthanded or both are righthanded. Otherwise the decay violates angular momentum conservation. But all observed processes change flavor only through the electroweak process of W boson emission. In the relativistic limit of zero mass leptons, these processes create only lefthanded leptons l^- and righthanded antileptons l^+ so that the total angular momentum is one. This *helicity suppression* is total in the case of massless a lepton pair, but is not total in the case of massive leptons. The branching ratios for a given pseudoscalar are ordered by mass in ratios $m_\tau^2 : m_\mu^2 : m_e^2 : m_\nu^2$.

Despite FCNC and helicity suppression, particle physics as it was known in 1970 predicted the occurrence of the decay $K_L \to \mu^+\mu^-$ at a far higher rate than was observed experimentally. Undiscovered particles are generally discovered either by direct onshell production, typically at the high energy frontier of accelerator technology, or through their effects as offshell virtual particles in loop processes at low energies. The latter type of discovery requires precision measurements to detect the often subtle influence of virtual particles. Glashow, Iliopolous and Maiani posited [9] that the unexpectedly low rate for $K_L \to \mu^+\mu^-$ was due an undiscovered particle, the charm quark, which contributed to the $K_L \to \mu^+\mu^-$ amplitude and nearly exactly canceled the expected amplitude. This interference, they surmised, accounted for the low rate for $K_L \to \mu^+\mu^-$ in what came to be known as the GIM mechanism. Four years later, in 1974, the charm quark was directly produced and observed in a bound state $J/\psi(c\bar{c})$.

For K^0 and D^0, the decay to a tau pair is prohibited by energy conservation. With the direct production of B mesons, a neutral meson decay to a tau pair first becomes kinematically possible. The helicity suppression in $B^0 \to \tau^+\tau^-$ is milder than in any other lepton pair case, with the enhancement over $B^0 \to e^+e^-$ of order $m_\tau^2/m_e^2 \approx 10^7$. But the greatest cause for interest in $B^0 \to \tau^+\tau^-$ is the potential for discovery of particles in physics beyond the SM.

The Higgs mechanism in the SM employs a single $SU(2)$ doublet which yields, after electroweak symmetry breaking, a single neutral scalar Higgs boson. In some models beyond the SM, at least two Higgs doublets are required. Their residue after symmetry breaking includes two charged scalars which could provide a new tree level flavor changing interaction. Models beyond the SM can yield $B^0 \to \tau^+\tau^-$ branching ratio predictions at up to two orders of magnitude larger than in the SM.

In the SM, the prediction is [3]

$$\mathcal{B}^{SM}(B^0 \to \tau^+\tau^-) = 3.1 \times 10^{-8} \left[\frac{\tau_B}{1.55\text{ps}}\right] \left[\frac{f_B}{180\text{MeV}}\right]^2 \left[\frac{|V_{td}|}{0.004}\right]^2 \tag{1.1}$$

This is the same order of magnitude as the current upper bound on $\mathcal{B}(B^0 \to e^+e^-)$ and $\mathcal{B}(B^0 \to \mu^+\mu^-)$. But electrons and muons are both longlived and directly observable. Unfortunately, the tau decay length ($c\tau$) is only about 0.1 mm, making it difficult to detect directly, and a tau pair decays to final states involving at least two and up to four undetectable neutrinos. This makes tau pair reconstruction difficult as there are no kinematic constraints which force the observable parameters into isolated regions of phase space. The consequences for measuring $B^0 \to \tau^+\tau^-$ will be considered in the next two sections.

1.2. CP Violation and the Babar Detector

The Babar detector was not built to measure $B^0 \to \tau^+\tau^-$. It was built to optimally measure the phenomenon of charge-parity conservation violation (CP-violation), which explains why matter rather than antimatter has come to dominate the particle content of the universe. Had physical interactions respected CP symmetry, no mechanism could have produced the imbalance between the two forms of matter we observe today. The magnitude of the asymmetry provides clues about whether the SM alone can account for all of the asymmetry or if there exists undiscovered physics which must account for part of it.

In the SM, CP-violation can occur in the electroweak interaction of quarks. The electroweak flavor eigenstates are actually mixed version of the physically realized mass eigenstates: $q_i^{flav} = V_{ij} q_j^{mass}$ where V_{ij} is the Cabibbo-Kobayashi-Maiani (CKM) matrix. The CKM matrix is a complex unitary rotation matrix whose 18 free parameters are reduced to four by unitarity and arbitrary quark phases. These free parameters are not fixed by SM theory. In a standard parameterization [2], one parameter δ is an imaginary phase which appears as $e^{i\delta}$ in five of the elements V_{ij}. One can show that CP-conservation in the SM cannot occur unless all CKM elements are real and, in fact, the magnitude of the CP asymmetry depends on δ. If $\delta = 0$, CP-violation cannot occur in the SM. Since $V^{\dagger}V = 1$, there are nine unitarity constraints relating the elements V_{ij}. One of them involves terms which are a product $V_{id}V_{ib}^{\star}$:

$$V_{ud}V_{ub}^{\star} + V_{uc}V_{cb}^{\star} + V_{td}V_{tb}^{\star} \;=\; 0 \tag{1.2}$$

In the complex plane, this equation represents a so-called *unitarity triangle.* One of the interior angles of this triangle, $\beta \equiv \arg(-V_{cd}V_{cb}^{\star}/V_{td}V_{tb}^{\star})$ is accessible experimentally through observation of neutral $B(\bar{b}d)$ meson decays. β is a function of all four CKM parameters, but in particular if δ vanishes so does β.

Neutral B mesons oscillate between B and $\bar{B}$ states with a frequency $\Delta m_B = m_B - m_{\bar{B}}$ through an electroweak process. The oscillation occurs by double W boson emission from quark vertices, so the amplitude for the process depends on the CKM elements V_{id} and V_{ib}. If two neutral Bs are produced simultaneously, as they are at Babar, and one is reconstructed in a CP eigenstate, then the other must also be a CP eigenstate. The decay rate $f(\Delta t)$ depends on the proper time Δt which has elapsed between the two decays. Due to neutral B oscillation, the decay rates are damped harmonic functions of Δt with amplitudes determined by the CKM elements. If one denotes the by f_+ the decay rate for B and by f_- the decay rate for $\bar{B}$, then one can define the CP asymmetry $(f_+ - f_-)/(f_+ + f_-)$. This asymmetry can be shown to be [3]

$$A_{CP}(\Delta t) \quad = \quad -\eta_f \sin 2\beta \sin(\Delta m_B \Delta t) \tag{1.3}$$

where $\eta_f = +1$ for CP even modes and $\eta_f = -1$ for CP odd modes. The flavor of the B meson ($\bar{B}$ or B) can be determined experimentally by observation of its decay products.

The amplitude of oscillation $\sin 2\beta$ can be measured if the proper time between B decays can be measured in many events. Since the required time resolution is unobtainable through experiment in the center of mass Lorentz frame, Δt must be measured indirectly by the displacement of the two vertices in a frame in which the entire event is boosted. The Babar detector and PEPII storage rings were built to produce a displacement of B decay vertices with a boost of $\beta\gamma = 0.56$. Then if the displacement Δz can be sufficiently well resolved, $\Delta t = \beta\gamma\Delta z/c$ can be measured.

The Babar Collaboration published its first result with 529 CP eigenstate events in 2001 [10] measuring $\sin 2\beta$ to be inconsistent with zero and thereby observing CP violation in B meson decays, but at a level consistent with the SM. In 2005, with 7730 CP eigenstate events, the preliminary unpublished result is $\sin 2\beta = 0.722 \pm 0.040(stat) \pm 0.023(syst)$.

The primary design goal of the Babar detector has been achieved in measuring $\sin 2\beta$, leaving many other phenomena of interest to measure. A good measurement for any signal phenomenon of interest requires that the signal be separated from the background by observable parameters. Since the decay products of $B^0 \to \tau^+\tau^-$ contain between two and four neutrinos, which are undetectable in collider detectors, measuring it requires that all decay products from background B decays are carefully accounted for in each event. The design goal of the Babar detector had two negative consequences for measuring $B^0 \to \tau^+\tau^-$ with respect to careful accounting of particles.

First, the large boost required to separate B decay vertices has the effect of boosting many B decay products out the uninstrumented forward end of the detector, where the beam pipe and steering magnets must be placed. Second, while Babar was built to detect K_L mesons from $B \to J/\psi K_L$ decays, these K_Ls typically have high momentum and are therefore more likely to interact at detectable levels with sensitive areas in the detector. Babar was not built to detect low momentum K_Ls. Therefore many B decays which lose particles through the forward end of the detector or produce low momentum K_Ls may mimic $B^0 \to \tau^+\tau^-$ decays with multiple neutrinos. The consequences for measuring $B^0 \to \tau^+\tau^-$ will be explored more fully in the following section.

1.3. $\mathbf{B^0} \to \tau^+\tau^-$ **Background at Babar**

Before elaborating a full analysis of $B^0 \to \tau^+\tau^-$, we first investigated the nature of the background to this mode in the Babar detector. We studied the simulation truth versions of decays in the generic neutral B simulation sample which passed a simplified $B^0 \to \tau^+\tau^-$ analysis after detector simulation. The rough analysis first reconstructed a neutral B from a hadronic decay and then searched in the recoil for the electron, muon and pion multiplicities required for a ditau decay.

The background sources are categorized as events with K_L which have not been detected but are within the detector acceptance, events with extra particles which have gone outside the detector acceptance, events which may be classed as kinematic

Category	90% Confidence Interval
Unidentified K_L	0.54 ± 0.14
Acceptance	0.30 ± 0.13
Kinematic	0.09 ± 0.08
Unidentified $K^{\pm}, K_S, \pi^0$	0.06 ± 0.07

Table 1.2: The 90% confidence intervals for the proportions of background by type remaining in the `B0B0bar generic` simulation sample after all $B^0 \to \tau^+\tau^-$ requirements are imposed.

background and events with an undetected K_S, charged kaon or neutral pion. See Table 1.2 for the proportions represented by each of these categories in the background sample.

We next used a simplified set of $B^0 \to \tau^+\tau^-$ requirements which reconstructed tau pair modes with four and six (as well as two) tracks to study the background sample. Due to the abundance of high multiplicity neutral B decays, the signal to background ratio for the four and six track modes was considerably higher than for the two track modes. These higher multiplicity modes were therefore abandoned.

The branching ratios [2] for typical background modes with undetected K_L are of order 10^{-3} and 10^{-4}. These modes are easily generalized: the b quark in the signal B candidate undergoes a cascade decay $b \to W^- c(\to W^+ s)$ which produces two oppositely charged virtual W bosons and a strange quark. The strange quark hadronizes into a K_L which does not interact sufficiently with the detector material to be identified. For the $ll'4\nu$ modes, the typical background due to particles lost outside the detector acceptance come from hadronic modes in which a γ from a π^0 is lost. For the other two modes, two oppositely charged tracks are lost forward. These modes are typically of order 10^{-3} and 10^{-4}. Many of the events categorized as irreducible, which have branching ratios of oder 10^{-4} and 10^{-5} might by eliminated by the neural net selection, which is sensitive to kinematics. A few typical background modes, their category and branching ratio are found in Table 1.3.

The two principal sources of background arise due to deficiencies inherent in the design of the Babar detector. Both exhibit the large missing energy and signal side multiplicities found in the signal ditau decay. The K_L background arises from very low momentum K_L which are not distinguishable from electronics noise in the IFR or EMC. The acceptance background arises from the $\gamma\beta = 0.56$ boost necessary for the study of CP violation and the large opening in the forward region of the detector mandated by the PEPII dipole magnets.

See [11] for a full description of the neutral hadron selector criteria and performance, where a study found that 28% of all K_L are expected to produce zero hits in the neutral hadron detectors (Resistive Plate Chambers). The authors found that in a sample of inclusive $B^0 \rightarrow J/\psi$ events, the K_L efficiency was found to rise from 0.05 linearly with momentum up to a peak at 0.65 at approximately 2.2 GeV.

Mode	Category	Branching Ratio [2]
$B^0 \to D(\to \boxed{K_L} \pi\pi^0)\pi\pi^0$	Missing K_L	7.7×10^{-4}
$B^0 \to D(\to \boxed{K_L} \pi\pi^0)l\nu$	Missing K_L	2.0×10^{-3}
$B^0 \to D(\to \boxed{K_L} l'\nu' l\nu)$	Missing K_L	1.4×10^{-3}
$B^0 \to D(\to K_L\pi\pi^0(\gamma\boxed{\gamma}))l\nu$	Acceptance	1.0×10^{-3}
$B^0 \to D(\to \boxed{K\pi} \pi\pi^0)l\nu$	Acceptance	1.4×10^{-3}
$B^0 \to D(\to \boxed{K\pi} \pi\pi^0)\pi\pi^0$	Acceptance	5.0×10^{-4}
$B^0 \to \rho l\nu$	Kinematic	2.5×10^{-4}
$B^0 \to D(\to \pi\pi^0)l\nu$	Kinematic	5.0×10^{-5}
$B^0 \to \pi l\nu$	Kinematic	1.8×10^{-4}

Table 1.3: Typical background modes to a $B^0 \to \tau^+\tau^-$ analysis and their branching ratios. Kinematic background is rejected either by rejecting high momentum candidates or by using a neural network analysis.

1.4. **Outline of the Dissertation**

This dissertation is divided into seven chapters. The first four chapters are primarily background material describing the process $B^0 \to \tau^+\tau^-$ and the experimental apparatus used to measure it. Chapter 1 (this chapter) introduces the measurement, provides some historical context and gives a brief description of the limitations inherent in measuring $B^0 \to \tau^+\tau^-$ with the Babar detector.

Chapter 2 outlines several models of particles physics, including the currently accepted paradigm, and reviews the literature for theoretical predictions for $B^0 \to \tau^+\tau^-$ in each model. Chapter 3 describes the Babar detector design, function and performance. Chapter 4 covers the simulation of both the underlying physics events (for signal $B^0 \to \tau^+\tau^-$ and background events) and the propagation of these events through the Babar detector in time. It should be emphasized that none of the material in Chapters 1-4 is original research. Rather, it is descriptive material necessary for an understanding of the material in Chapters 5-7. These latter chapters document the original research carried out by the author and present the techniques used to measure the rare decay $B^0 \to \tau^+\tau^-$ at Babar.

Chapter 5 details the strategy for isolating the signal $B^0 \to \tau^+\tau^-$ events away from the background events as far as this is possible in the Babar detector. The strategy evolved from a deeper and deeper understanding of the characteristic signature of the signal event simulation as it appears in the detector, together with an understanding of how the typical events can mimic the signal events. Chapter 6 outlines the methods used to obtain a branching ratio measurement which incorporates the statistical uncertainties and systematic biases inherent in the measurement.

The analysis was a *blind* analysis, so that the selection and limit setting procedure are finalized before observing the data yield with the full selection. Blind analyses help remove systematic biases which result from tuning too closely to data, and when coupled with data control samples they also help disentangle systematic biases from statistical fluctuations in the data background. Chapters 5 and 6 therefore do not include data with the full selection. Chapter 7 presents the unblinded data and the results of the world's first measurement of the rare decay $B^0 \to \tau^+\tau^-$.

Chapter 2

$B^0 \to \tau^+\tau^-$ THEORY

2.1. Introduction

The partial width Γ for any two body decay is determined by Fermi's Golden Rule to be $\Gamma = p\mathcal{M}^2/8\pi m^2$ where p is the momentum of either daughter in the center-of-mass frame, m is the mother mass and $\mathcal{M}$ is the amplitude for the process mediating the decay. The branching ratio is then $\mathcal{B} = \tau\Gamma$ where τ is the lifetime of the mother. For $B^0 \to \tau^+\tau^-$,

$$\mathcal{B}(B^0 \to \tau^+\tau^-) \;=\; \frac{\tau_B}{16\pi m_B}|\mathcal{M}_{B^0\to\tau^+\tau^-}|^2\sqrt{1-4m_\tau^2/m_B^2} \qquad (2.1)$$

This holds regardless of which physics model one adopts. Variations in predictions for the branching ratio for this unobserved decay in different models manifest themselves in the amplitude $\mathcal{M}_{B^0\to\tau^+\tau^-}$.

A general amplitude can be constructed by factoring the amplitude into a product of a tau current and a quark current [12]. The amplitude is then decomposed into tau scalar, pseudoscalar, vector, axial vector and tensor components with Wilson coefficients C_S, C_P, C_V, C_A and C_T. Since the B meson is a pseudoscalar (parity odd), the vector quark current is zero. The vector tau current vanishes on contraction with the axial quark current. Therefore $C_V = 0$. The tensor quark current is zero, so $C_T = 0$. From [12], the amplitude is given to be

$$\mathcal{M}_{B^0 \to \tau^+\tau^-} = i f_B m_B G_F \left[\left(C_P + \frac{2m_\tau}{m_B} C_A \right) (\bar{\tau}\gamma_5\tau) + C_S \bar{\tau}\tau \right] \tag{2.2}$$

where τ and $\bar{\tau}$ are the tau spinor and tau adjoint spinor, f_B is the B meson decay constant and G_F is the Fermi constant employed to scale the Wilson coefficients.

The branching ratio is then

$$\mathcal{B}(B^0 \to \tau^+\tau^-) = \frac{G_F^2}{16\pi} \tau_B m_B f_B^2 \sqrt{1 - 4m_\tau^2/m_B^2} \tag{2.3}$$

$$\times \left[\left(C_P + \frac{2m_\tau}{m_B} C_A \right) (\bar{\tau}\gamma_5\tau) + C_S \bar{\tau}\tau \right]^2 \tag{2.4}$$

Variations in the predicted rate for $B^0 \to \tau^+\tau^-$ will manifest themselves in the Wilson coefficients C_A, C_P and C_S.

This chapter considers the decay $B^0 \to \tau^+\tau^-$ in several models for fundamental particle interactions. In the Standard Model, the decay is helicity suppressed. This leads to a low prediction ($\mathcal{O}(10^{-8})$) for the branching ratio. In the Two-Higgs-Doublet model, a new mechanism for the decay (charged Higgs exchange) allows an enhancement in the branching ratio by a factor $\tan^4\beta$, where $\tan\beta$ is a free parameter of the model. In the minimal supersymmetric model, which subsumes the Two-Higgs-Doublet Model, a further mechanism for $B^0 \to \tau^+\tau^-$ (chargino and gluino exchange) allows for an enhancement by a factor $\tan^6 \beta$. Many models contain leptoquarks, hypothetical particles which carry both lepton and baryon number and couple leptons directly to quarks. In these models the rate for $B^0 \to \tau^+\tau^-$ is enhanced by the square of the coupling of the b to the τ (λ_{33}) and the coupling of the d to the τ (λ_{31}).

2.2. The Standard Model

Outline of the Standard Model

The Standard Model (SM) of the electroweak and strong interactions in particle physics is defined by the Lagrangian $\mathcal{L}_{SM}$. The guiding principle in constructing $\mathcal{L}_{SM}$ is local gauge symmetry: it is invariant under an arbitrary local gauge transformation of the underlying symmetry group $U(1) \times SU(2) \times SU(3)$ of the SM [13] [14]. This principle ensures that the interactions contained in the SM are renormalizable, an indispensable property of any viable theory because it allows the perturbative calculation of observable quantities. Most SM predictions for observables have been verified by experimental observation, and no experimental result has decisively contradicted the SM [15].

Lepton	Q	J	Quark	Q	J	Boson	Q	J
e	-1	1/2	u	2/3	1/2	$\Phi(h)$	0	0
ν_e	0	1/2	d	-1/3	1/2	$A(\gamma)$	0	1
μ	-1	1/2	c	2/3	1/2	Z	0	1
ν_μ	0	1/2	s	-1/3	1/2	W^+	+1	1
τ	-1	1/2	t	2/3	1/2	W^-	-1	1
ν_τ	0	1/2	b	-1/3	1/2	$G_k(g)$	0	1

Table 2.1: The charge and spin of fermion (left) and boson (right) fields in the SM Lagrangian. The W, Z and A fields are generated by the electroweak group ($U(1) \times SU(2)$) generators, and the eight fields G_k are generated by the strong interaction group $SU(3)$ generators.

In the underlying symmetry group of the SM , the subgroup $U(1)$ is Abelian, but the subgroups $SU(2)$ and $SU(3)$ are not. If τ_j ($j = 1, 2, 3$) and λ_k ($k = 1, ..., 8$) are the generators for $SU(2)$ and $SU(3)$ respectively, then $[\tau^i, \tau^j] = i\epsilon_{ijk}\tau^k$ and $[\lambda^i, \lambda^j] = if_{ijk}\lambda^k$ define the Lie Algebra for $SU(2)$ and $SU(3)$. The ϵ and f are the *structure constants* for $SU(2)$ and $SU(3)$ respectively. Then any element of the SM gauge group can be written $u_1u_2u_3$ where $u_1 = \exp(-i\theta(x^\mu))$, $u_2 = \exp(-i\alpha_j(x^\mu)\tau^j)$ and $u_3 = \exp(-i\beta_k(x^\mu)\lambda^k)$ are the elements of $U(1)$, $SU(2)$ and $SU(3)$ respectively. The functions $\theta(x^\mu)$, $\alpha_j(x^\mu)$ and $\beta_k(x^\mu)$ are explicitly space and time dependent, as demanded by local gauge symmetry.

The field content of the SM is summarized in Table 2.1[1]. The only scalar field in the SM, the Higgs field Φ, is vital to the theory since, by virtue of its coupling to other fields it generates the mass of the particles associated with the fields. The fermionic fields are the leptons and quarks. The vector fields are generated by requiring gauge symmetry: one distinct vector field is required for each generator of the underlying symmetry group. For the $U(1) \times SU(2)$ electroweak transformations, the Higgs field and the fermionic fields which undergo electroweak interactions are arranged into $SU(2)$ doublets or singlets. The Higgs field is a complex doublet

---

[1] The notation in this section follows closely that of [13].

$$\Phi = \begin{pmatrix} \Phi_0 + i\Phi_1 \\ \Phi_2 + i\Phi_3 \end{pmatrix}. \tag{2.5}$$

The lefthanded lepton fields are arranged in doublets, while the righthanded fields are arranged in singlets. Similarly, the quarks are arranged into lefthanded doublets and righthanded singlets. The $SU(3)$ strong transformations act on quark $SU(3)$ color triplets. Explicitly,

$$\begin{pmatrix} \nu_{eL} \\ e_L \end{pmatrix}, \begin{pmatrix} \nu_{\mu L} \\ \mu_L \end{pmatrix}, \begin{pmatrix} \nu_{\tau L} \\ \tau_L \end{pmatrix}, e_R, \mu_R, \tau_R \tag{2.6}$$

$$\begin{pmatrix} u_L \\ d_L \end{pmatrix}, \begin{pmatrix} c_L \\ s_L \end{pmatrix}, \begin{pmatrix} t_L \\ b_L \end{pmatrix}, u_R, d_R, c_R, s_R, t_R, b_R \tag{2.7}$$

$$\begin{pmatrix} q_r & q_g & q_b \end{pmatrix}^T (q = u, d, c, s, t, b) \tag{2.8}$$

where r, g, b denote red, green and blue color charge. Since leptons do not carry color charge, they do not participate in the strong interaction and are therefore not subject to $SU(3)$ transformations.

Local gauge invariance means that when the fields are transformed by a local gauge transformation, the Lagrangian remains invariant. This requires the introduction of gauge derivatives which incorporate the vector boson fields in such a way as to counteract the effect of gauge transforming the fields. Also introduced in the gauge derivatives are the gauge group $U(1) \times SU(2) \times SU(3)$ coupling constants g_1, g_2, g_3, which are undetermined in the SM and must be measured by experiment. The SM Lagrangian contains terms for each field:

$$\mathcal{L}_{SM} = \mathcal{L}_{\Phi} + \mathcal{L}_{vectors} + \mathcal{L}_{leptons} + \mathcal{L}_{quarks}^{electroweak} + \mathcal{L}_{quarks}^{strong} \tag{2.9}$$

and the term due to the scalar field is

$$\mathcal{L}_{\Phi} = (D_\mu \Phi)^\dagger (D^\mu \Phi) - \frac{m}{2\phi_0}(\Phi^\dagger \Phi - \phi_0^2)^2 \tag{2.10}$$

where m is the Higgs boson mass and ϕ_0 is the vacuum expectation value of the Higgs field. D_μ is the $U(1) \times SU(2)$ gauge derivative described below. The remaining terms in the SM Lagrangian will be developed below.

After transforming the Higgs field in $U(1)$ space, $\Phi \rightarrow \Phi' = u_1 \Phi$, the $U(1)$ symmetry is obtained by requiring the existence of a vector gauge field B_μ and the use of the $U(1)$ gauge derivative. The transformations which preserve the Lagrangian are

$$\Phi \rightarrow \Phi' = u_1 \Phi \tag{2.11}$$

$$B_\mu \rightarrow B'_\mu = B_\mu + \frac{2}{g_1 Y} \partial_\mu \theta \tag{2.12}$$

$$\partial_\mu \rightarrow D_\mu^{U(1)} = \partial_\mu + \frac{1}{2} i g_1 Y B_\mu \tag{2.13}$$

where g_1 is the $U(1)$ coupling and Y is the $U(1)$ charge (also called *weak hypercharge*).

Transforming the Higgs field in $SU(2)$ space $\Phi \rightarrow \Phi' = u_2 \Phi$ requires the existence of three further vector gauge fields W_μ^1, W_μ^2 and W_μ^3, combined together as the $SU(2)$ operator $W_\mu = W_\mu^i \tau^i$ $(i = 1, 2, 3)$ where the τ^i are the $SU(2)$ generators. Then

$$\Phi \rightarrow \Phi' = u_2 \Phi \tag{2.14}$$

$$W_\mu \rightarrow W'_\mu = u_2 W_\mu u_2^\dagger + \frac{2}{g_2 T} i (\partial_\mu u_2) u_2^\dagger \tag{2.15}$$

$$\partial_\mu \rightarrow D_\mu^{SU(2)} = \partial_\mu + \frac{1}{2} i g_2 T W_\mu \tag{2.16}$$

where g_2 is the $SU(2)$ coupling and T is the $SU(2)$ charge (also called *weak isospin charge*). Weak isospin T is 1/2 for weak isospin doublets and 0 for weak isospin singlets. The third component of T, denoted T_3, is $+1/2$ for neutrino and up type quark fields and $-1/2$ for lepton and down type quark fields. Weak hypercharge is related to weak isospin charge T_3 and electric charge Q by $Y = 2(Q - T_3)$.

Finally, rotating the quark triplets in $SU(3)$ space requires the existence of eight vector gauge fields $G_\mu^1, ..., G_\mu^8$, one for each generator of $SU(3)$. The $SU(3)$ operator

$G_\mu = G^i_\mu \lambda^i$, where the λ^i $(i = 1, ..., 8)$ are the $SU(3)$ generators. The simultaneous gauge transformation required to preserve the Lagrangian is

$$\Phi \to \Phi' = u_3 \Phi \tag{2.17}$$

$$G_\mu \to G'_\mu = u_3 G_\mu u_3^\dagger + \frac{2}{g_3} i (\partial_\mu u_3) u_3^\dagger \tag{2.18}$$

$$\partial_\mu \to D_\mu^{SU(3)} = \partial_\mu + \frac{1}{2} i g_3 G_\mu \tag{2.19}$$

where g_3 is the $SU(3)$ charge. The introduction of the vector bosons B_μ, W_μ and G_μ requires that there be a dynamical term in the Lagrangian

$$\mathcal{L}_{dynamical} = -\frac{1}{4} B_{\mu\nu} B^{\mu\nu} - \frac{1}{8} Tr(W_{\mu\nu} W^{\mu\nu}) - \frac{1}{2} Tr(G_{\mu\nu} G^{\mu\nu}) \tag{2.20}$$

since these are the dynamical terms in the Lagrangian for vector bosons. The field strength tensors are defined by

$$B_{\mu\nu} = \partial_\mu B_\nu - \partial_\nu B_\mu \tag{2.21}$$

$$W_{\mu\nu} = \partial_\mu W_\nu - \partial_\nu W_\mu + \frac{1}{2} i g_2 [W_\mu, W_\nu] \tag{2.22}$$

$$G_{\mu\nu} = \partial_\mu G_\nu - \partial_\nu G_\mu + \frac{1}{2} i g_3 [G_\mu, G_\nu]. \tag{2.23}$$

The commutator term in $B_{\mu\nu}$ is zero since $U(1)$ is Abelian. Since $SU(2)$ and $SU(3)$ are non-Abelian the commutators $[W_\mu, W_\nu]$ and $[G_\mu, G_\nu]$ are nonzero. As a consequence, there are no self-couplings of the B_μ field but there are cubic and quartic self-couplings of the W_μ and G_μ fields.

The vector mass terms are generated by $SU(2)$ symmetry breaking, discussed below. Together the dynamical term and the mass terms for the vector fields comprise the vector boson Lagrangian $\mathcal{L}_{vectors}$.

According to the SM, nature chose to physically realize the fields mixed versions of B_μ and W_μ: the fields A_μ, Z_μ, W_μ^+ and W_μ^-. These fields are related by

$$\begin{pmatrix} A_\mu \\ Z_\mu \end{pmatrix} = \begin{pmatrix} \sin\theta_W & \cos\theta_W \\ \cos\theta_W & -\sin\theta_W \end{pmatrix} \begin{pmatrix} W_\mu^3 \\ B_\mu \end{pmatrix} \tag{2.24}$$

$$\begin{pmatrix} W_\mu^+ \\ W_\mu^- \end{pmatrix} = \begin{pmatrix} 1 & i \\ i & -1 \end{pmatrix} \begin{pmatrix} W_\mu^1 \\ W_\mu^2 \end{pmatrix} \tag{2.25}$$

The mixing angle θ_W is one of the undetermined parameters of the SM which has been measured experimentally. When these definitions are used to solve for the fields B_μ and W_μ in terms of the physical fields, the terms $B_{\mu\nu}B^{\mu\nu}$ and $W_{\mu\nu}W^{\mu\nu}$ in $\mathcal{L}_{dynamical}$ yield the interactions of the physical fields: the cubic interactions AW^+W^- and ZW^+W^- and the quartic interactions $WWZZ$, $WWAA$, and $WWZA$. The term $G_{\mu\nu}G^{\mu\nu}$ yields the cubic GGG and quartic $GGGG$ gluonic self-interactions.

The B_μ, W_μ and G_μ vector boson mass terms are explicitly excluded from the Lagrangian term $\mathcal{L}_{dynamical}$. In the SM they are generated when the $SU(2)$ symmetry is broken when the Higgs field chooses a particular orientation in $SU(2)$ space. This electroweak space symmetry breaking takes the form

$$\Phi \rightarrow \begin{pmatrix} 0 \\ \phi_0 + \frac{1}{\sqrt{2}} h(x_\mu) \end{pmatrix} \tag{2.26}$$

where ϕ_0 is the vacuum expectation for Φ and $h(x_\mu)$ is a local excitation above the vacuum. With this expression for Φ and the $U(1)$ and $SU(2)$ gauge derivatives, the Lagrangian $\mathcal{L}_\Phi$ contains W and Z mass terms as well as hW^+W^- and hZZ direct couplings which are proportional to the masses. The A mass term is zero (as required for photons), and there is no tree level hAA coupling. Likewise, the G mass term is zero (rendering gluons massless) and there is no tree level hGG coupling. These properties of $\mathcal{L}_\Phi$ are due to the unbroken $U(1)$ and $SU(3)$ symmetries. Also appearing in $\mathcal{L}_\Phi$ is the term $\partial_\mu h \partial^\mu h - m^2 h^2$, the Klein-Gordon Lagrangian for a scalar field h with mass m, and the cubic and quartic self-interactions hhh and $hhhh$ of the Higgs scalar.

The fermions obtain mass by coupling to the Higgs field Φ. The electroweak Lagrangian for leptons $\mathcal{L}_{leptons}$ gives mass to e, μ, τ (but not their neutrinos) with the terms $m_l(l_L^\dagger l_R + l_R^\dagger l_L)$ for $l = e, \mu, \tau$. Together with the dynamical term, this yields

$$\begin{aligned}\mathcal{L}_{leptons} &= \sum_{l=e,\mu,\tau} \left[\begin{pmatrix} \nu_{lL} \\ l_L \end{pmatrix}^\dagger (\tilde{\sigma}^\mu i D_\mu) \begin{pmatrix} \nu_{eL} \\ e_L \end{pmatrix} + l_R^\dagger (\sigma^\mu i D_\mu) l_R \right] \\ &\quad - \sum_{l=e,\mu,\tau} \left[c_l \left(\begin{pmatrix} \nu_{lL} \\ l_L \end{pmatrix}^\dagger \Phi l_R + CC \right) \right] \end{aligned} \tag{2.27}$$

where the symbols $\sigma^\mu = (1, \sigma)$ and $\tilde{\sigma}^\mu = (1, -\sigma)$ are defined by the Pauli matrices $\sigma_1, \sigma_2, \sigma_3$. Note that the $SU(2)$ gauge derivative does not act on righthanded leptons, which are not arranged in $SU(2)$ doublets as the lefthanded leptons are. This corresponds to the experimental observation that righthanded lepton fields do not couple to the W field. After $SU(2)$ symmetry breaking, and using the $U(1) \times SU(2)$ gauge derivative, $\mathcal{L}_{leptons}$ contains Dirac Lagrangians for all leptons with mass terms determined by the constants c_l as well as the direct couplings $hl_L^\dagger l_R + CC$, $Wl_L^\dagger \nu_{lL} + CC$, $Zl_L^\dagger l_L$, $Zl_R^\dagger l_R$, $Al_L^\dagger l_L$ and $Al_R^\dagger l_R$. The Higgs couplings are proportional to the mass terms c_l. The lepton masses (or, equivalently, their couplings to the Higgs scalar) are undetermined in the SM.

The electroweak Lagrangian for quarks is similar to that for the leptons, but two factors somewhat complicate it. Whereas neutrinos are massless in $\mathcal{L}_{leptons}$, up type quarks u_i (u, c, t) must be given mass by coupling to Φ. Furthermore, while generational mixing of leptons is disallowed in $\mathcal{L}_{leptons}$, it is required in $\mathcal{L}_{quarks}^{electroweak}$ in order to conform to experimental observations. The electroweak quark Lagrangian is

$$\begin{aligned}
\mathcal{L}_{quarks}^{electroweak} \;=\; & \sum_i \left[\begin{pmatrix} u_{iL} \\ d_{iL} \end{pmatrix}^{\dagger} (\tilde{\sigma}^{\mu} i D_{\mu}) \begin{pmatrix} u_{iL} \\ d_{iL} \end{pmatrix} + u_{iR}^{\dagger}(\sigma^{\mu} i D_{\mu}) u_{iR} + d_{iR}^{\dagger}(\sigma^{\mu} i D_{\mu}) d_{iR} \right] \\
& - \sum_i c_i \left(G_{ij}^{d} \begin{pmatrix} u_{jL} \\ d_{iL} \end{pmatrix}^{\dagger} \Phi d_{iR} + CC \right) && (2.28) \\
& - \sum_i b_i \left(G_{ij}^{u} \epsilon_{ab} \begin{pmatrix} u_{iL} \\ d_{jL} \end{pmatrix}_{b}^{\dagger} \Phi_a u_{iR} + CC \right) && (2.29)
\end{aligned}$$

The introduction of the matrices G^u and G^d (which operate in flavor space) account for the mixing of flavor eigenstates in mass eigenstates, and the use of the antisymmetric tensor ϵ ($\epsilon_{11} = \epsilon_{22} = 0$ and $\epsilon_{12} = -\epsilon_{21} = 1$) allows up type quarks to couple to Φ and thereby obtain mass. After symmetry breaking, $\mathcal{L}_{quarks}^{electroweak}$ contains the Dirac Lagrangian for quarks (with mass terms) as well as the interactions $hq_L^{\dagger}q_R + CC$, $Zq_L^{\dagger}q_L$, $Zq_R^{\dagger}q_R$, $Aq_L^{\dagger}q_L$, $Aq_R^{\dagger}q_R$, and $Wu_{iL}^{\dagger}d_{jL}$. The G^u and G^d mixing matrices can be diagonalized with unitary matrices $G^u = U_L^{\dagger}M^u U_R$ and $G^d = D_L^{\dagger}M^d D_R$ where the mass matrices M are diagonal. Then the quark interactions with the W gauge boson can be written $Wu_{iL}^{\dagger}V_{ij}d_{jL}$ where $V = U_L D_L^{\dagger}$ is the Cabibbo-Kobayashi-Maskawa (CKM) matrix. The strength of each interaction is determined by the weak hypercharge Y, weak isospin T and the CKM elements V_{ij}.

Leptons	Quarks	Bosons (Cubic)	Bosons (Quartic)
$hl_L^\dagger l_R + CC$	$hq_L^\dagger q_R + CC$	hWW	$WWZZ$
$Zl_L^\dagger l_L + Zl_R^\dagger l_R$	$Zq_L^\dagger q_L + Zq_R^\dagger q_R$	hZZ	$WWAA$
$Al_L^\dagger l_L + Al_R^\dagger l_R$	$Aq_L^\dagger q_L + Aq_R^\dagger q_R$	AWW	$WWZA$
$Wl_L^\dagger \nu_{lL} + CC$	$Wu_{iL}^\dagger d_{jL} + CC$	ZWW	$WWWW$
	$G_{ij} q_{iL}^\dagger q_{jL}$	GGG	$GGGG$
		hhh	$hhhh$

Table 2.2: The interactions allowed in the Standard Model.

Finally, the strong interaction Lagrangian involves only the $SU(3)$ vector bosons G_μ^i. The Lagrangian is

$$\mathcal{L}_{quarks}^{strong} = \sum_{q=u,d,s,c,b,t} \left[\begin{pmatrix} q_r \\ q_g \\ q_b \end{pmatrix}^\dagger (\tilde{\sigma}^\mu i D_\mu) \begin{pmatrix} q_r \\ q_g \\ q_b \end{pmatrix} - m_q \begin{pmatrix} q_r \\ q_g \\ q_b \end{pmatrix}^\dagger \begin{pmatrix} q_r \\ q_g \\ q_b \end{pmatrix} \right] \tag{2.30}$$

where the quark masses m_q are generated by coupling to the Higgs field above. $\mathcal{L}_{quarks}^{strong}$ gives the qqG couplings and the Dirac equation for quarks. Properties of this and the dynamical Lagrangian term $G_{\mu\nu}G^{\mu\nu}$ have had success in explaining the strong interaction properties of confinement and asymptotic freedom. See Table 2.2 for a complete list of interactions allowed by the SM Lagrangian.

$\mathbf{B^0} \rightarrow \tau^+\tau^-$ in the Standard Model

Since the SM is a renormalizable field theory, the amplitude for $B^0 \rightarrow \tau^+\tau^-$ may be calculated perturbatively. If an interaction is not explicitly prohibited by kinematic or conservation considerations, it is expected to occur in the SM. We can therefore proceed from first order in perturbation theory to higher orders to discover the dominant process which mediates $B^0 \to \tau^+\tau^-$.

Three observations from Table 2.2 are most helpful in determining the process by which $B^0 \to \tau^+\tau^-$ proceeds in the SM. First, the only interactions involving quarks or leptons are cubic interactions. Second, there is no cubic interaction $qq'X$ where X is neutral. An interaction $qq'X$ would give rise to a tree level flavor-changing neutral current (FCNC), which the SM does not admit. This forces the initial state quarks to interact at distinct interaction vertices. Third, there is no direct interaction involving both a quark and a lepton. The following argument applies to the general case of a neutral meson decaying to a lepton pair.

The process cannot occur at first order in perturbation theory because there is no quartic interaction in the SM involving either quark or lepton fields. Nor can it occur at second order: there is no cubic interaction $qq'X$ where X is neutral (for an $s-$channel process), and there is no cubic interaction involving a quark and lepton field (for a $t-$ or $u-$channel process). At third order, the final state leptons must meet at the same interaction vertex. But since the only allowed quark interactions are cubic, this forces the lepton vertex to be a quartic interaction. But this cannot be in the SM since there are no quartic lepton interactions.

The process can proceed with four interaction vertices. Since the only tree level flavor changing interaction in the SM ($Wu^\dagger_{iL}d_{jL}$) is charged and the meson is neutral, there must be at least two such interactions (one mediated by W^+ and the other

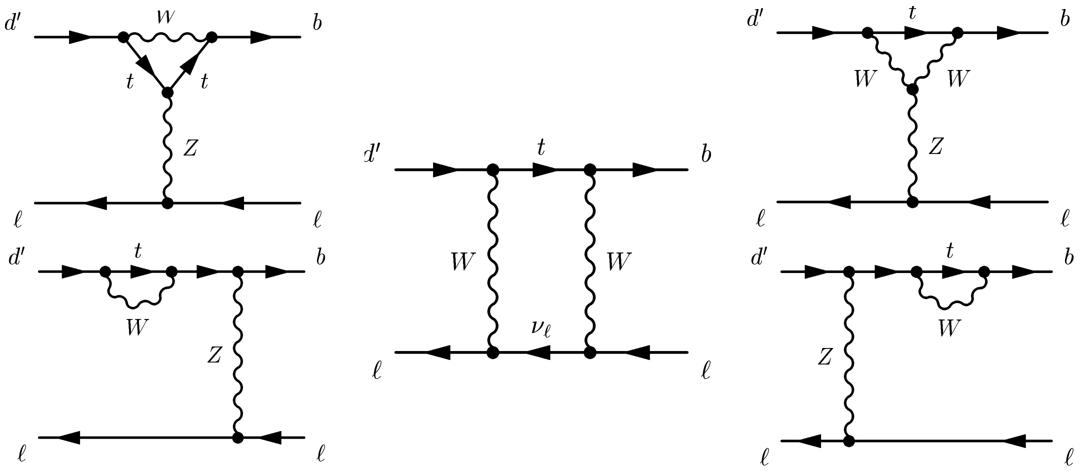

Figure 2.1: Standard Model box (middle), penguin (top left and right) and self-energy (bottom left and right) processes responsible for $B^0 \to \tau^+\tau^-$.

by W^-), one each at the initial state quark vertices. Then either the Ws or the undetermined quarks meet at the two remaining free vertices. If the final state leptons share a common interaction vertex, then either the undetermined quarks may proceed to the last free vertex (in which case the Ws connect the initial state quark vertices) or the Ws may proceed to the last free vertex (in which case the undetermined quarks connect the initial state quark vertices). In either case, the $q\bar{q}$ or W^+W^- vertex must connect to the final state lepton pair vertex with a h, A or Z line. The resulting diagrams are called *penguin* diagrams. See Figure 2.1 (top left and right) for the penguin diagrams which mediate $B^0 \to \tau^+\tau^-$.

Note also that if a penguin diagram with W emission from the d quark line reabsorbs the W, such a diagram is called a *self-energy* diagram. See Figure 2.1 (bottom left and right) for the diagrams. Self-energy diagrams contributing to $B^0 \to$

$\tau^+\tau^-$ are also allowed at fourth order in the SM.

If the final state leptons do not share the same vertex, then the undetermined quarks must connect the initial state quark vertices and the Ws proceed to the lepton vertices (since there is no SM interaction involving both a quark and a lepton). The only interaction available for the lepton vertices is $Wl_L^\dagger \nu_{lL}$, in which case the resultant neutrino connects the final state lepton vertices. Such a diagram is called a *box* diagram. See Figure 2.1 (middle) for the box diagram which mediates $B^0 \to \tau^+\tau^-$.

The SM amplitude for a neutral meson decay to a lepton pair was calculated in [16] for $K_L \to \mu^+\mu^-$. In [17] the amplitude was calculated for $B_q \to \tau^+\tau^-$ $(q = d, s)$, and in [18] QCD corrections at first order in α_s were calculated. The QCD corrections account for single gluon emission and reabsorption by quark lines in both box and penguin diagrams, and for $B^0 \to l^+l^-$ were found at most to be 13% effects by the authors of [18]. A more recent estimate for $B^0 \to \tau^+\tau^-$ in [19] found the correction to be a 3% effect.

In the SM, the penguin diagrams contribute to C_P and C_S, but these are suppressed relative to C_A by a factor of $(m_b/m_W)^2 \approx 2.6 \times 10^{-3}$ [12]. The box diagram dominates through its contribution to C_A. Box top exchange diagrams dominate the contribution from box diagrams with up and charm exchange. From [12],

$$C_A^{SM} = |V_{td}^\star V_{tb}| \frac{\alpha_{em}(m_W)}{\sqrt{8}\pi \sin^2 \theta_W} Y((m_t/m_W)^2) \tag{2.31}$$

where $Y(x) = Y_0(x) + \frac{\alpha_s}{4\pi} Y_1(x)$ includes the order α_s correction term. The terms $C_P^{SM} \approx C_S^{SM} \approx 0$ relative to C_A^{SM}. From [19], the numerical expression for Y is

$$Y((m_t/m_W)^2) = 0.997 \left[\frac{m_t(m_t)}{166 GeV}\right]^{1.55} \tag{2.32}$$

Collecting together these elements and inserting them into the expression for the branching ratio in Equation 2.4, from [3]

$$\mathcal{B}^{SM}(B^0 \to \tau^+\tau^-) = 3.1 \times 10^{-8} \left[\frac{\tau_B}{1.55 ps}\right] \left[\frac{f_B}{180 MeV}\right]^2 \left[\frac{|V_{td}|}{0.004}\right]^2 . \tag{2.33}$$

2.3. The Two-Higgs-Doublet Model

Outline of the Two-Higgs-Doublet Model (2HDM)

While no experimental observation has successfully challenged the SM as a model of fundamental particle interactions, there is still a key component which has not yet been observed: the Higgs scalar h. And while the simplest assumption of a single $SU(2)$ doublet Higgs field is sufficient to generate mass and thereby explain $SU(2)$

symmetry breaking, it is not necessary. Nature may have chosen a more elaborate scheme.

In the Two-Higgs-Doublet Model (2HDM), the non-Higgs sector field content is identical to the field content of the SM. But in the Higgs sector, two $SU(2)$ doublets are employed for $SU(2)$ symmetry breaking and mass generation rather than one as in the SM [20]. If only one of the doublets couples to fermions and the other is decoupled, the 2HDM is a 2HDM *type 1*. If one doublet couples to up type fermions and the other couples to down type fermions, the 2HDM is a 2HDM *type 2*. The Higgs sector of the 2HDM type 2 employs the doublets

$$H_u = \begin{pmatrix} H_u^+ \\ H_u^0 \end{pmatrix} \tag{2.34}$$

$$H_d = \begin{pmatrix} H_d^0 \\ H_d^- \end{pmatrix} \tag{2.35}$$

to generate mass. H_u generates mass for the up type quarks and up type leptons. H_d generates mass for the down type quarks and down type leptons. Hereafter 2HDM will refer to 2HDM type 2.

In the 2HDM, as in the SM, particles obtain mass when $SU(2)$ symmetry is broken. In the 2HDM, the Higgs fields H_u and H_d assume particular orientations in $SU(2)$ space:

$$H_u \rightarrow \begin{pmatrix} 0 \\ v_u \end{pmatrix} + \frac{1}{\sqrt{2}} \begin{pmatrix} h_u^+ \\ h_u^0 \end{pmatrix} \tag{2.36}$$

$$H_d \rightarrow \begin{pmatrix} v_d \\ 0 \end{pmatrix} + \frac{1}{\sqrt{2}} \begin{pmatrix} h_d^0 \\ h_d^- \end{pmatrix} \tag{2.37}$$

where h_u and h_d are excitations above the vacuum expectations v_u and v_d. Since there is no *a priori* connection between the vacuum expectation values v_u and v_d, their relative magnitudes are encoded in a free parameter of the 2HDM, $\tan\beta \equiv v_u/v_d$. There is no experimentally preferred value for $\tan\beta$, but in grand unified theories with $SO(10)$ as the unification gauge group it is found that the third generation Yukawa couplings unify at the unification scale when $\tan\beta$ is large (of order m_t/m_b) [**?**].

The fields H_u and H_d couple to the SM fermions in the natural way (see Equation 2.55). But in the 2HDM, the quark Yukawa coupling matrix is not necessarily diagonalizable in the same basis as the quark mass matrix. This is the case for large $\tan\beta$ [21]. This generates off-diagonal entries in the Yukawa matrix, which introduces flavor changing interaction vertices $qq'H^{\pm}$.

The physically realized particles of the 2HDM Higgs sector are mixed versions of the scalar excitations h_u^+, h_u^0, h_d^0 and h_d^-. Goldstone bosons $G^{\pm}$ and G^0 are absorbed by gauge vectors. The physical fields are

$$\begin{pmatrix} G^+ \\ H^+ \end{pmatrix} = \begin{pmatrix} \sin\beta & -\cos\beta \\ \cos\beta & \sin\beta \end{pmatrix} \begin{pmatrix} h_u^+ \\ h_d^+ \end{pmatrix} \tag{2.38}$$

$$\begin{pmatrix} G^0 \\ A^0 \end{pmatrix} = \sqrt{2} \begin{pmatrix} \sin\beta & -\cos\beta \\ \cos\beta & \sin\beta \end{pmatrix} Im \begin{pmatrix} h_u^0 \\ h_d^0 \end{pmatrix} \tag{2.39}$$

$$\begin{pmatrix} h^0 \\ H^0 \end{pmatrix} = \sqrt{2} \begin{pmatrix} \sin\alpha & -\cos\alpha \\ \cos\alpha & \sin\alpha \end{pmatrix} Re \begin{pmatrix} h_u^0 \\ h_d^0 \end{pmatrix} \tag{2.40}$$

where the mixing angle α is another free parameter in the 2HDM. Since the Goldstone bosons are unphysical and are only required in Feynman-t'Hooft gauge, this leaves the charged Higgs H^+ and H^-, the scalar Higgs h^0 and H^0 and the pseudoscalar A^0.

$\mathbf{B^0} \to \tau^+\tau^-$ in the 2HDM

The 2HDM provides a mechanism for the enhancement of $B^0 \to \tau^+\tau^-$ over the SM rate, but not at less than fourth order in perturbation theory. The introduction of new 2HDM flavor changing couplings $qq'H^\pm$ and $qq'G^\pm$ allow for additional processes similar to those in the SM. Thus any $W^\pm$ boson in the SM box and penguin diagrams may be replaced by a charged Higgs boson $H^\pm$ or a charged Goldstone boson $G^\pm$. In addition, there are three neutral Higgs scalars A^0, H^0 and h^0 in the 2HDM which may replace a Z^0 or photon line. The amplitude $\mathcal{M}^{2HDM}_{B^0\to\tau^+\tau^-}$ was first calculated in [17] and later in [19]. The authors of [19] found the results in [17] to be gauge dependent

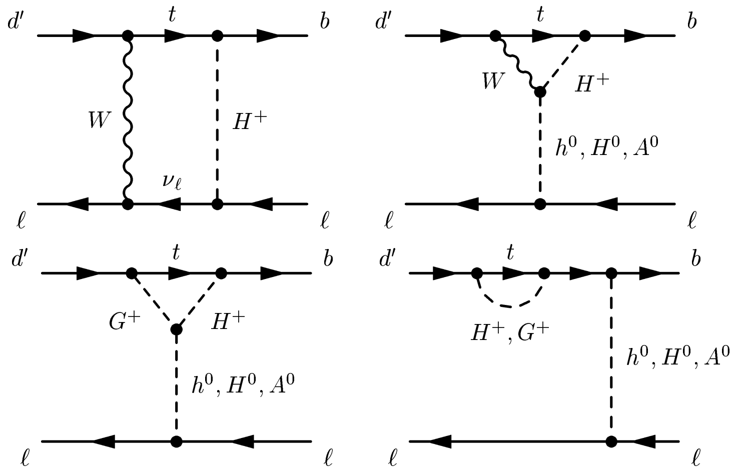

Figure 2.2: Dominant 2HDM processes responsible for $B^0 \to \tau^+\tau^-$. These are similar to the SM diagrams but with a $qtW^\pm$ $(q = b, d)$ vertex replaced by a $qtH^\pm$ or $qtG^\pm$ vertex.

and therefore necessarily incorrect.

The dominant 2HDM diagrams which mediate $B^0 \to \tau^+\tau^-$ are shown in Figure 2.2. They are variations of the box and penguin diagrams in the SM but with contributions from the 2HDM Higgs sector. The first is the SM box diagram but with a single $qtW^\pm$ $(q = b, d)$ vertex replaced by a $qtH^\pm$ or $qtG^\pm$, the second is the SM penguin but with a single $qtW^\pm$ vertex replaced by a $qtH^\pm$ or $qtG^\pm$ and the third is the SM self-energy diagram with a single $qtW^\pm$ vertex replaced by a $qtH^\pm$ or $qtG^\pm$ so that the d quark line changes into a b line by emission and reabsorption of a $H^\pm$ or $G^\pm$. Diagrams in which both $btW^\pm$ and $dtW^\pm$ vertices are replaced by $qtH^\pm$ or $qtG^\pm$ vertices are suppressed by $(m_\tau/m_W)^2 \approx 4.9 \times 10^{-4}$ [22]. According to [19], there are no new contributions to the axial vector Wilson constant C_A in the 2HDM. But the

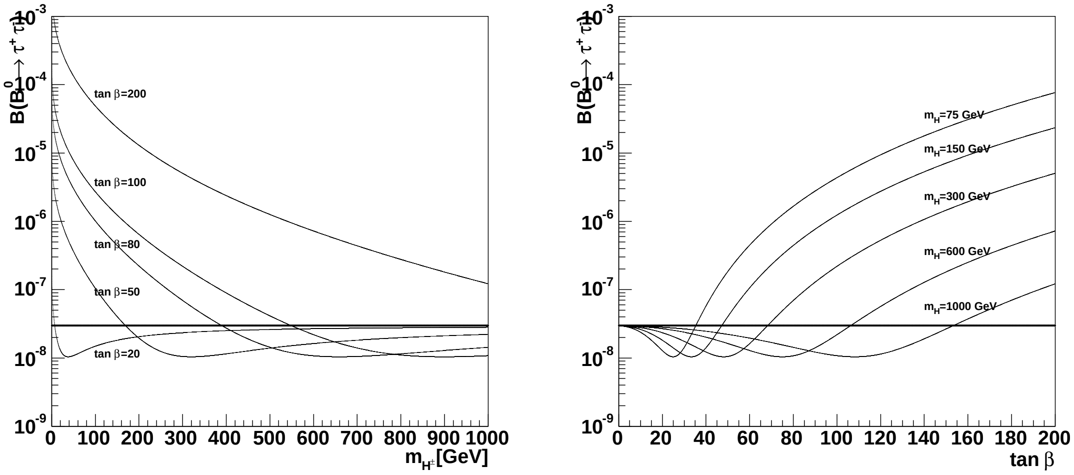

Figure 2.3: Branching ratio $\mathcal{B}^{2HDM}(B^0 \to \tau^+\tau^-)$ plotted against $m_{H^\pm}$ (left) and against $\tan\beta$ (right) in the large $\tan\beta$ limit. The SM value is shown in bold.

constants C_P and C_S are modified due to the 2HDM box, penguin and self-energy processes so that, for large $\tan\beta$, $C_A^{2HDM} = C_A^{SM}$ and

$$C_S^{2HDM} = C_S^{2HDM} = \frac{m_\tau}{2m_W^2}\tan^2\beta\frac{\log r}{r-1} \tag{2.41}$$

where $r = m_{H^\pm}^2/m_t^2(m_t)$. The 2HDM branching ratio is then [19]

$$\mathcal{B}^{2HDM}(B^0 \to \tau^+\tau^-) = 2.4\times10^{-8}\left[\frac{\tau_B}{1.54ps}\right]\left[\frac{f_B}{210MeV}\right]^2\left[\frac{|V_{td}|}{0.008}\right]^2 \times \left(a^2+b^2\right) \tag{2.42}$$

$$a = 5.4\times10^{-4}\tan^2\beta\frac{\log r}{1-r} - Y((m_t/m_W)^2) \tag{2.43}$$

$$b = 4.0\times10^{-4}\tan^2\beta\frac{\log r}{1-r} \tag{2.44}$$

where $Y(x_t)$ is defined in Equation 2.32. See Figure 2.3 for a plot of the branching ratio versus the charged Higgs mass $m_{H^\pm}$ and versus $\tan\beta$. The SM and 2HDM amplitudes interfere destructively, but for large $\tan\beta$ the 2HDM enhancement dominates.

2.4. Supersymmetry

Outline of Supersymmetry

While the SM remains experimentally unchallenged as a model for fundamental particle interactions, there is a strong motivation to revise it on theoretical grounds. While experiment has determined that the vacuum expectation value for m_h must be of order 100 GeV, theoretical calculations show that first order corrections to m_h^2 are of order $M_{Pl}^2 = (2.4 \times 10^{18}\ \text{GeV})^2$, the energy scale at which quantum gravity must alter the SM if it is to be a complete theory. Keeping the Higgs mass at the electroweak scale despite an unavoidable Planck scale correction is known as the *hierarchy problem.*

Supersymmetry theory [23] introduces a new symmetry Q and develops much in the spirit of the gauge symmetry of the SM. The supersymmetry Q

acts on bosonic particle to create fermionic superpartner, and acts on fermionic particles to create bosonic superpartners. The commutation relations [2]

$$\{Q, Q^\dagger\} = P^\mu \tag{2.45}$$

$$\left[Q^\dagger, Q^\dagger\right] = [Q, Q] = 0 \tag{2.46}$$

$$\left[P^\mu, Q^\dagger\right] = [P^\mu, Q] = 0 \tag{2.47}$$

define the supersymmetry algebra [23]. Since P^μ commutes with Q, the superparticle mass is equal to the particle mass if the supersymmetry is unbroken. But the symmetry is slightly broken, causing the difference in particle and super partner masses. Thus in supersymmetry, particles acquire mass after $SU(2)$ symmetry breaking, and their superpartners acquire different masses from their partners after supersymmetry breaking.

The huge SM correction to m_h^2 comes from the fermionic quark loop in the Higgs propagator. This diagram arises from the $hq_R^\dagger q_L$ interaction in Table 2.2. Unless this diagram is miraculously cancelled by higher order corrections, the experimentally preferred value for m_h is excluded. Supersymmetry solves the hierarchy problem since, for each fermionic loop correction to m_h^2, there is a scalar loop correction with the opposite sign which exactly cancels it. If the supersymmetry is broken, the cancellation is not exact. But if it is only mildly broken, the Higgs mass remains at the electroweak scale. The cancellation only occurs if the superpartner of the fermion quark is a scalar.

---

[2] The notation in this section follows [23]. Throughout, ϕ represents a scalar, ψ a chiral fermion, λ a gaugino fermion and F a vector.

From $\{Q, Q^\dagger\} = P^\mu$ one can show [23] that the number of degrees of freedom in a particle must equal the number of degrees of freedom in the superpartner. From this requirement and that of renormalizability, it can be shown that there are only two ways of grouping particles with superpartners: chiral or gauge supermultiplets. Chiral supermultiplets group Weyl fermions with complex scalars. Gauge supermultiplets group massless vectors with Weyl fermions. Only chiral supermultiplets allow different gauge transformation rules for lefthanded and righthanded fermions, so quarks and leptons must be grouped together with their *squark* and *slepton* scalar superpartners in a chiral supermultiplet. The gauge vectors must be grouped together with their fermionic *gaugino* superpartners in a gauge supermultiplet. Supersymmetry posits that the gauge group generators commute with Q, so that the superpartner gauge quantum numbers (electric charge, weak hypercharge, weak isospin) are the same as those of the partner.

Whereas a single Higgs doublet was sufficient in the SM to generate mass, supersymmetry requires at least two. This is due to a divergence (the *triangle anomaly*) [23] which is uncancelled in supersymmetry with one Higgs doublet but cancelled with two. Minimally, supersymmetry employs two Higgs doublets (as in the 2HDM) to generate mass for the chiral fields. H_u generate mass for the up type (s)quarks and up type (s)leptons. H_d generate mass for the down type (s)quarks and down type (s)leptons.

The general supersymmetric Lagrangian $\mathcal{L}_{SS}$ allows for undiscovered fermions and bosons and their superpartners. But beyond the superpartners of the fields already discovered and the Higgs sector, it does not require them. The Lagrangian is

$$\mathcal{L}_{SS} = \mathcal{L}_{chiral} + \mathcal{L}_{gauge} + \mathcal{L}_{int}^{\phi\psi\lambda}. \tag{2.48}$$

The chiral supermultiplet Lagrangian contains kinetic terms for all scalars (Higgs, sleptons and squarks) and chiral fermions (higgsinos, leptons and quarks), a scalar-fermion interaction term and a term for an *auxiliary* field F:

$$\mathcal{L}_{chiral} = -(D^{\mu}\phi_i)^{\dagger}(D_{\mu}\phi_i) - i\psi_j^{\dagger}(\bar{\sigma}^{\mu}D_{\mu})\psi_j + \mathcal{L}_{int}^{\phi\psi} + F_i F^{i\star}. \tag{2.49}$$

All scalar fields are indexed by i and all chiral fermions are indexed by j. The auxilliary fields are necessary to maintain the required balance between fermionic and bosonic degrees of freedom in the supermultiplet when the field particles are offshell. The interaction term is determined by the *superpotential* W

$$\mathcal{L}_{int}^{\phi\psi} = -\frac{1}{2}W^{ij}\psi_i\psi_j + W^{i\star}W_i + CC \tag{2.50}$$

$$W = \frac{1}{2}M^{ij}\phi_i\phi_j + y^{ijk}\phi_i\phi_j\phi_k. \tag{2.51}$$

This is the maximal set of renormalizable interactions between scalars and chiral fermions [23]. Here $W^i = \partial_{\phi_i}W$ and $W^{ij} = \partial_{\phi_i}\partial_{\phi_j}W$. The M^{ij} are mass terms and the y^{ijk} are Yukawa couplings: the $W^{i\star}W_i$ term contains cubic and quartic interactions among scalars as well as scalar mass terms, and the $W^{ij}\psi_i\psi_j$ term contains fermion mass terms as well as cubic Yukawa interactions. $\mathcal{L}_{chiral}$ contains the SM Lagrangian terms $\mathcal{L}_{leptons}$, $\mathcal{L}_{quarks}^{electroweak}$ and $\mathcal{L}_{quarks}^{strong}$, as well as their equivalents for sleptons and squarks. It also contains the supersymmetric analog of $\mathcal{L}_{\Phi}$, which involves the doublets H_u and H_d.

The gauge supermultiplet Lagrangian contains kinetic terms for the gauge vectors (B, W, G) as well as gaugino fermions ($\tilde{B}$, $\tilde{W}$, $\tilde{G}$). It also contains an auxiliary field D for the gauge fields:

$$\mathcal{L}_{gauge} = \frac{1}{4}F^{i}_{\mu\nu}F^{i\mu\nu} - i\lambda^{j\dagger}(\tilde{\sigma}^{\mu}D_{\mu})\lambda^{j} + \frac{1}{2}D^{i}D_{i} \tag{2.52}$$

where i indexes gauge fields and j indexes gaugino fields. The gauge fields and gauginos are massless before $SU(2)$ symmetry breaking. The D field is required again in order to maintain the equality betwen the fermionic and bosonic degrees of freedom. $\mathcal{L}_{gauge}$ contains the term $\mathcal{L}_{dynamical}$ from the SM Lagrangian. Using the equations of motion for the auxiliary fields, they can be replaced by $F_i = W_i^{\star}$ and $D_j = -g_j(\phi^{\star}T^{j}\phi)$ where T^j is the jth generator and g_j is the jth coupling of the gauge group.

The superpotential defines all Yukawa interactions in the MSSM. The gauge and gaugino interactions are determined by the action of gauge covariant derivatives on the fields as in the SM. The only remaining term in $\mathcal{L}_{SS}$ contains all gauge invariant and renormalizable interactions between scalars, chiral fermions and gauginos which are not generated by the covariant derivatives D^{μ}:

$$\mathcal{L}_{int}^{\phi\psi\lambda} = -\sqrt{2}g_j((\phi^{\star}T^j\psi)\lambda^j) + CC) + g_j^2(\phi^{\star}T^j\phi)(\phi^{\star}T^j\phi). \tag{2.53}$$

$\mathcal{L}_{SS}$ is the most general renormalizable Lagrangian which is invariant under a supersymmetric transformation $\phi \to Q\phi$, $\psi \to Q\psi$, $\lambda \to Q\lambda$, $F \to QF$ [23]. It remains general until the field content $\{\phi, \psi, \lambda, F\}$ and superpotential W are specified.

The Minimal Supersymmetric Model (MSSM)

Any supersymmetry model must be phenomenologically viable. This means that it must include all fields which are already known to exist, it must specify a superpotential which excludes interactions in $\mathcal{L}_{SS}$ which violate conservation laws already observed to hold true, and it must specify the terms in $\mathcal{L}_{SS}$ which break the symmetry and render sparticle masses at values above the current experimental reach.

At a minimum, the supersymmetry field content must include all SM fields (less the Higgs doublet Φ) and the SM interactions. It must also include all supersymmetric partners of the SM fields as well as the two Higgs doublets H_u and H_d. See Tables 2.3 and 2.4 for the minimal additional content in the MSSM.

The scalar content ϕ of the MSSM includes squark fields, slepton fields and Higgs fields H_u and H_d. The chiral fermion content ψ includes the SM quark fields, SM

Slepton	Q	J	Squark	Q	J	Gaugino	Q	J
$\tilde{e}$	-1	0	$\tilde{u}$	2/3	0			
$\tilde{\nu}_e$	0	0	$\tilde{d}$	-1/3	0	$\tilde{A}(\gamma)$	0	1/2
$\tilde{\mu}$	-1	0	$\tilde{c}$	2/3	0	$\tilde{Z}$	0	1/2
$\tilde{\nu}_\mu$	0	0	$\tilde{s}$	-1/3	0	$\tilde{W}^+$	+1	1/2
$\tilde{\tau}$	-1	0	$\tilde{t}$	2/3	0	$\tilde{W}^-$	-1	1/2
$\tilde{\nu}_\tau$	0	0	$\tilde{b}$	-1/3	0	$\tilde{G}_k(g)$	0	1/2

Table 2.3: The minimal additional field content of the MSSM, excluding the Higgs sector. These are the superpartners of the leptons, quarks and gauge vectors from Table 2.1 (which are also included in the MSSM).

lepton fields and the higgsino fields $\tilde{H}_u$ and $\tilde{H}_d$. The gaugino fermion content λ includes the superpartners of the SM gauge fields $\tilde{B}$, $\tilde{W}^+$, $\tilde{W}^-$, $\tilde{W}^0$ and $\tilde{G}$. The gaugino vector content includes the SM gauge fields B, W^+, W^- W^0 and G.

The superpotential for the MSSM is

$$W_{MSSM} = \tilde{u}_{jR} y_j^u \begin{pmatrix} \tilde{u}_{jL} \\ \tilde{d}_{jL} \end{pmatrix}^\dagger \epsilon H_u - \tilde{d}_{jR} y_j^d \begin{pmatrix} \tilde{u}_{jL} \\ \tilde{d}_{jL} \end{pmatrix}^\dagger H_d \tag{2.54}$$

$$- \tilde{l}_{jR} y_j^l \begin{pmatrix} \tilde{\nu}_{jL} \\ \tilde{l}_{jL} \end{pmatrix}^\dagger H_d + \mu (\epsilon H_u)^\dagger H_d \tag{2.55}$$

Here y_j^u, y_j^d and y_j^l are Yukawa couplings. Note in particular the flavor changing Yukawa interactions involving the scalars H_u and H_d, which are not present in the SM.

While there are many interactions in the MSSM, and therefore many potentially free parameters, large subgroups of interactions occur with the same coupling

Higgs	Q	J	Higgsino	Q	J
H_u^+	+1	0	$\tilde{H}_u^+$	+1	1/2
H_u^0	0	0	$\tilde{H}_u^0$	0	1/2
H_d^0	0	0	$\tilde{H}_d^0$	0	1/2
H_d^-	-1	0	$\tilde{H}_d^-$	-1	1/2

Table 2.4: The MSSM Higgs sector.

strength. For example, consider three flavor changing (s)quark interactions mediated by a charged H_u or its superpartner: $y_j^d \tilde{d}_{jL}^\dagger H_u^+ \tilde{u}_{jR}$, $y_j^d \tilde{d}_{jL}^\dagger \tilde{H}_u^+ u_{jR}$, and $y_j^d d_{jL}^\dagger \tilde{H}_u^+ \tilde{u}_{jR}$. All three interactions occur with the same coupling y_j^d.

In all observed processes, lepton number L and baryon number B are conserved. The MSSM explicitly excludes interactions which violate L or B conservation by postulating a new conservation law. It first defines R-parity $P_R = (-1)^{3(B-L)+2S}$ where S is spin. If this multiplicative quantum number is conserved, as the MSSM stipulates, then B and L are also conserved. Since particles have $P_R = +1$ and sparticles have $P_R = -1$, P_R conservation has some interesting phenomenological consequences: the lightest supersymmetric partner (the *LSP*) is stable against decay, sparticles are produced in even numbers at colliders colliding $P_R = +1$ particles, and sparticle decays contain an odd number of sparticles in the final state.

The MSSM adopts the 2HDM Higgs sector in its entirety. At tree-level, the masses of h^0, H^0, A^0, and $H^\pm$ are fixed by MSSM parameters. Radiative corrections impose an upper limit of 130 GeV on m_{h^0} given reasonable assumptions about the stop masses [23]. As this upper limit is approached, the remaining Higgs sector masses become large and the MSSM couplings approach those of the SM in what is called the *decoupling limit*.

In principle, any sparticles in Tables 2.3 and 2.4 which share the same spin, electric charge and color charge may mix to produce mass eigenstates. The neutral gauginos $\tilde{B}$ and $\tilde{W}$ may mix with the neutral higgsinos $\tilde{H}_u^0$ and $\tilde{H}_d^0$ to form any of four *neutralinos* $\tilde{N}_1$, $\tilde{N}_2$, $\tilde{N}_3$ or $\tilde{N}_4$. The charged gauginos $\tilde{W}^+$ and $\tilde{W}^-$ may mix with charged higgsinos $\tilde{H}_u^+$ and $\tilde{H}_d^-$ to form any of four *charginos* $\tilde{C}_1^+$, $\tilde{C}_1^-$, $\tilde{C}_2^+$ or $\tilde{C}_2^-$. The gluino cannot mix because it is the only neutral fermion which carries color charge. The squarks and sleptons are not expected to mix except in the third generation, where the left- and righthanded fields mix to produce mass eigenstates $\tilde{t}_1$, $\tilde{t}_2$, $\tilde{b}_1$, $\tilde{b}_2$, $\tilde{\tau}_1$ and $\tilde{\tau}_2$.

$\mathbf{B^0} \to \tau^+\tau^-$ in the MSSM

The amplitude for $B^0 \to \mu^+\mu^-$ in the MSSM was first calculated in [21], again in [22] and again in [24]. It is easily translated to $B^0 \to \tau^+\tau^-$.

The MSSM incorporates the 2HDM and therefore inherits the 2HDM mechanism for enhancing $B^0 \to \tau^+\tau^-$ over the SM rate. In addition, the MSSM introduces two further mechanisms: the flavor changing supersymmetrized $q\tilde{q}'\tilde{H}^\pm$, $q\tilde{q}'\tilde{G}^\pm$ and $q\tilde{q}'\tilde{W}^\pm$ couplings, and the flavor changing mass insertion $\tilde{q}\tilde{q}'$ due to off-diagonal entries in the squark mass matrix. Neither mechanism occurs at less than fourth order in perturbation theory or in processes with Feynman diagrams topologically distinct from those of the SM.

The MSSM couplings $q\tilde{q}'\tilde{H}^{\pm}$, $q\tilde{q}'\tilde{G}^{\pm}$ and $q\tilde{q}'\tilde{W}^{\pm}$ allow for the decay of a quark into a squark of a different flavor with the emission of a chargino with higgsino, goldstino or wino content. Thus any $qq'W$ vertex in the SM box and penguin diagrams could be replaced by a $q\tilde{q}'\tilde{C}_1$ or a $q\tilde{q}'\tilde{C}_2$ vertex. Moreover, if the MSSM squark mass matrix is not diagonalizable in the same basis as the quark mass matrix, off-diagonal entries in the squark mass matrix entries induce flavor changing mass insertions $\tilde{q}\tilde{q}'$ [21]. A neutral Higgs penguin diagram with gluino exchange between initial quark lines (with $d\tilde{d}\tilde{g}$ and $b\tilde{b}\tilde{g}$ vertices) and a mass insertion $\tilde{b}\tilde{d}$ also contributes to $B^0 \to l^+l^-$ in the MSSM. See Figure 2.4 for Feynman diagrams of $B^0 \to \tau^+\tau^-$ through chargino and gluino exchange.

The authors of [22] found that the box diagram with chargino or gluino exchange does not appreciably alter the Wilson coefficient C_A over the SM value. Nor do the Z penguin diagrams with chargino or gluino exchange alter C_P or C_A over the 2HDM values. But for large $\tan\beta$, the neutral Higgs (h^0, H^0, A^0) penguin diagrams with chargino exchange or gluino exchange with mass insertion enhance C_P and C_S by a factor of $\tan^3\beta$.

For simplicity, we consider only the case when the gluino exchange diagram is negligible. In the limit of diagonal squark matrix, the gluino exchange penguin contributes nothing to the process $B^0 \to \tau^+\tau^-$ and the chargino exchange penguin dominates.

The Wilson coefficients for chargino exchange are found to be $C_A^{MSSM} = C_A^{SM}$ and [22]

$$C_P^{MSSM} = C_S^{MSSM} = C_P^{2HDM} + \frac{m_\tau}{2m_W^2}\frac{m_t^2}{m_A^2}\tan^3\beta\,\tilde{A}_t m_{\tilde{C}_1} C_0(m_{\tilde{C}_1}, m_{\tilde{t}_1}, m_{\tilde{t}_2}) \tag{2.56}$$

where the three point function C_0 is

$$C_0(x,y,z) = \frac{1}{x-y}\left[\frac{x}{x-z}\log\frac{x}{z} - \frac{y}{y-z}\log\frac{y}{z}\right] \tag{2.57}$$

and $\tilde{A}_t = A_t + \mu\cot\beta$. Here A_t is the top Yukawa coupling. The corresponding branching ratio is enhanced by a factor of $\tan^6\beta$ in the MSSM, and is calculated to be [22]

$$\begin{align}
\mathcal{B}^{MSSM}(B^0 \to \tau^+\tau^-) &= 2.4 \times 10^{-8}\left[\frac{\tau_B}{1.54ps}\right]\left[\frac{f_B}{210MeV}\right]^2\left[\frac{|V_{td}|}{0.008}\right]^2 \tag{2.58}\\
&\quad \times \left(c^2 + d^2\right) \tag{2.59}\\
c &= a + 5.4 \times 10^{-4}\frac{m_t^2}{m_A^2}\tan^3\beta\,\tilde{A}_t m_{\tilde{C}_1} C_0(m_{\tilde{C}_1}, m_{\tilde{t}_1}, m_{\tilde{t}_2}) \tag{2.60}\\
d &= b + 4.0 \times 10^{-4}\frac{m_t^2}{m_A^2}\tan^3\beta\,\tilde{A}_t m_{\tilde{C}_1} C_0(m_{\tilde{C}_1}, m_{\tilde{t}_1}, m_{\tilde{t}_2}) \tag{2.61}
\end{align}$$

The gluino exchange penguin amplitude is found also to increase as $\tan^3\beta$ [22]. But this amplitude may interfere either constructively or destructively with the chargino exchange penguin. For some regions of parameter space, the interference is destructive (see the following section).

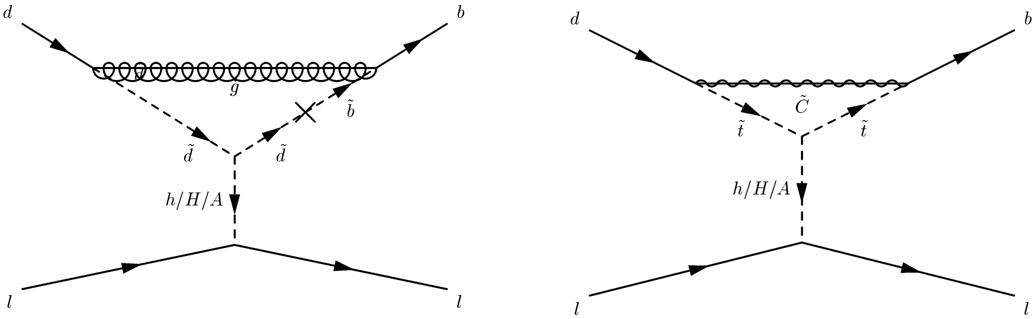

Figure 2.4: Dominant MSSM processes responsible for $B^0 \to \tau^+\tau^-$. At left is the penguin with gluino exchange with flavor changing mass insertion. At right is the penguin with chargino exchange.

$\mathbf{B^0} \to \tau^+\tau^-$ in Constrained MSSMs

In order to account for the mass differences between particles and their superpartners, the terms in $\mathcal{L}_{SS}$ which break supersymmetry at the electroweak scale must be specified. In the MSSM, these are the gaugino, higgsino, slepton and squark mass terms as well as the squark-Higgs and slepton-Higgs couplings. The mechanism of supersymmetry breaking in the MSSM is still unknown, but is thought to be due to radiative corrections to the sparticle masses due to particles in a *hidden sector* which do not interact with the SM particles. One can specify the mechanism of supersymmetry breaking and thereby further constrain the MSSM. Many of the masses and couplings in the MSSM can be seen to originate from common values at the unification scale. When the mechanism of supersymmetry breaking is specified, a specific set of unification scale masses and couplings can then be evolved down to the electroweak scale using the renormalization group equations.

In *gravity-mediated* supersymmetry breaking, the gravitino (the superpartner of the graviton) mediates the radiative corrections. This framework is called minimal Supergravity (*mSUGRA*). In *gauge-mediated* supersymmetry breaking, the *messenger* particles with SM gauge group quantum numbers mediates the radiative corrections, and the framework here is called minimal Gauge Mediated Supersymmetry Breaking (*mGMSB*). Neither mSUGRA nor mGMSB is fully satisfactory, with the Particle Data Group review referring to mSUGRA as "too simplistic" and mGMSB as "not a fully realized model" [25].

Nonetheless, the amplitude for $B^0 \to \mu^+\mu^-$ has been calculated in mSUGRA and mGMSB, first in [26], [27] and [28] and later in [29]. The mechanism for enhancing the rate for $B^0 \to \tau^+\tau^-$ in mSUGRA and mGMSB is the same as it is in the MSSM (chargino and gluino exchange) and the enhancement is also proportional to $\tan^6\beta$. These models simply constrain the electroweak scale masses and couplings to originate in common unification scale values which diverge after renormalization group evolution downward in energy to the electroweak scale.

In mSUGRA, only five parameters are free: the scalar mass m_0 at the unification scale, the gaugino mass $m_{1/2}$ at the unification scale, the scalar cubic coupling A_0 at the unification scale, $\tan\beta$ and the sign of the superpotential parameter $sgn(\mu)$. The authors of [29] found that, after scanning this parameter space, only a very small portion of the $m_0 - m_{1/2}$ plane is excluded by assuming $\tan\beta > 35$ and $B^0 \to \tau^+\tau^- > 10^{-6}$. They further found, however, that the penguin diagrams with gluino exchange and chargino exchange may interfere destructively and therefore decrease the enhancement below the $\tan^6\beta$ expectation. Even so, in the parameter space covered the branching ratio was found never to fall below half the SM expectation.

In mGMSB, the authors of [29] found that the enhancement is much lower than in mSUGRA. Here the free parameters are the sparticle mass scale Λ, the messenger mass scale M, the number of $SU(5)$ vector representations in the messenger sector, $\tan\beta$ and $sgn(\mu)$. In scans of this parameter space, after evolving the parameters down to the electroweak scale, the branching ration for $B^0 \to \tau^+\tau^-$ was found never to exceed 10^{-7}.

2.5. **Leptoquarks**

Models Containing Leptoquarks

The symmetry between quark and lepton generations suggests that there may be a hidden connection between quarks and leptons. There is no compelling theoretical reason in the SM why there should be the same number of quark generations as lepton generations, but the SM relies on the equal and opposite contributions from leptons and quarks to the hypercharge anomaly cancellation [30]. *Leptoquarks* codify this connection in a physically realized object.

The 2HDM and MSSM are only two of many possible extensions of the SM. Other models include:

- Grand Unified Theories (GUTs). GUTs seek to unify the electroweak, strong and gravitational interactions based on the groups $SU(5)$, $SO(10)$ or $SU(15)$.
- Composite Models. These models identify substructure in the SM. Quarks and leptons are made of *preons*.
- Technicolor Theories. Technicolor introduces a new non-Abelian gauge interaction and requires any scalars to be bound states of fermions and anti-fermions.

All of these models incorporate leptoquarks [31], which carry both lepton number L and baryon number B and are $SU(3)$ color triplets. The SM does not.

In the context of GUTs, leptoquarks were first introduced in an $SU(4)$ model in which lepton number is considered to be a fourth strong interaction color charge, extending the $SU(3)$ color symmetry [32]. Pati-Salam leptoquarks are then simply the gauge boson which mediate the $SU(4)$ strong interaction. The $SU(4)$ symmetry is broken down to $SU(3)$ symmetry, giving mass to the leptoquarks but leaving the gluons massless. Technicolor theories require all scalars to be bound states of a fermion and an anti-fermion, and a bound state $l\bar{q}$ or $\bar{l}q$ would be a natural candidate for a leptoquark. Compositie theories build leptons and quarks from preons, which therefore must carry lepton number and baryon number. Bound states of two preons

Leptoquark	J	F	Q	Leptoquark	J	F	Q
S_0	0	-2	1/3	V_0	1	0	2/3
$\tilde{S}_0$	0	-2	4/3	$\tilde{V}_0$	1	0	5/3
$S_{1/2}$	0	0	5/3,2/3	$V_{1/2}$	1	-2	4/3,1/3
$\tilde{S}_{1/2}$	0	0	2/3,-1/3	$\tilde{V}_{1/2}$	1	-2	1/3,-2/3
S_1	0	-2	4/3,1/3,-2/3	V_1	1	0	5/3,2/3,-1/3

Table 2.5: The spin J, fermion number $F = 3B + L$ and charge Q for leptoquarks allowed for renormalizable SM gauge group invariant interactions.

could then carry both lepton and baryon number and would also be natural candidates for leptoquarks.

Assuming that the leptoquark interactions are renormalizable and invariant under the SM gauge group transformation, the number of leptoquark $SU(2)$ multiplets is fixed at ten: the scalars $S_0, \tilde{S}_0, S_{1/2}, \tilde{S}_{1/2}, S_1$ and the vectors $V_0, \tilde{V}_0, V_{1/2}, \tilde{V}_{1/2}, V_1$ [30]. The subscripts indicate the weak isospin quantum number of the leptoquark. Leptoquarks are either scalars or vectors and carry fermion number $F = -2$ or $F = 0$ ($F = L + 3B$). Different models incorporate different subsets: superstring E_6 includes only S_0 while the $SU(15)$ GUT includes all ten leptoquarks. See Table 2.5 for the leptoquarks and their quantum numbers. The Lagrangian which includes all interactions of the leptoquarks with leptons and quarks is given by

$$\mathcal{L}_{LQ} = \sum_{i,j} \sum_{m,n} \sum_{LQ} \lambda_{ijn}^{LQ} l_i^m q_j^n \tag{2.62}$$

where λ_{ijn}^{LQ} is the coupling of the lepton from generation i to the quark of generation j with chirality n to the leptoquark LQ. The lepton chirality m is determined by

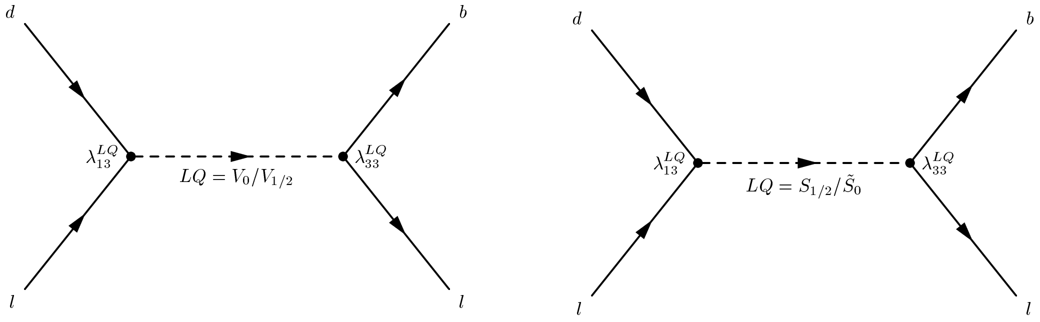

Figure 2.5: Vector (left) and scalar (right) leptoquark processes which mediate $B^0 \to \tau^+\tau^-$. The quark and lepton chirality labels have been suppressed.

angular momentum conservation and J_{LQ}. The $F = -2$ leptoquarks couple lq and the $F = 0$ leptoquarks couple $l\bar{q}$.

Phenomenological viability requires that some constraints must be placed on some leptoquark couplings and masses. A given interaction involving a given leptoquark can be suppressed by i) requiring separate B and L conservation, ii) requiring a sufficiently small coupling λ, iii) requiring the leptoquark mass to be sufficiently large or iv) requiring the leptoquark to couple only to one generation. For example, FCNC constraints from the upper limit on $\mathcal{B}(K^0 \to \mu e)$ are satisfied if the leptoquark is not allowed to couple to both the first and second generation.

$\mathbf{B^0} \to \tau^+\tau^-$ in Models Containing Leptoquarks

In contrast to the SM, 2HDM and the MSSM, leptoquarks couple quarks and leptons directly at tree level and therefore provide a mechanism for $B^0 \to \tau^+\tau^-$ at second order in perturbation theory. The process occurs by t-channel exchange of a leptoquark. The authors of [12] identify four leptoquarks ($S_{1/2}, \tilde{S}_0, V_0$ and $V_{1/2}$)

g_0^{RR}	$\frac{\lambda_{31R}^{\tilde{S}_0}\lambda_{33R}^{\tilde{S}_0}}{8G_F m_{\tilde{S}_0}^2}, \frac{\lambda_{31R}^{V_0}\lambda_{33R}^{V_0}}{4G_F m_{V_0}^2}$	g_0^{LR}	$\frac{\lambda_{31R}^{S_{1/2}}\lambda_{33R}^{S_{1/2}}}{8G_F m_{S_{1/2}}^2}, \frac{\lambda_{31R}^{V_{1/2}}\lambda_{33R}^{V_{1/2}}}{4G_F m_{V_{1/2}}^2}$
$g_0^{\prime LL}$	$\frac{\lambda_{31L}^{V_0}\lambda_{33L}^{V)}}{4G_F m_{V_0}^2}$	$g_{1/2}^{RL}$	$\frac{\lambda_{31R}^{V_0}\lambda_{33L}^{V_0}}{2G_F m_{V_0}^2}$
$g_{1/2}^{LR}$	$\frac{\lambda_{31L}^{V_0}\lambda_{33L}^{V_0}}{2G_F m_{V_0}^2}$		

Table 2.6: Leptoquark couplings which enter the Wilson coefficients for $B^0 \to \tau^+\tau^-$.

which mediate $B^0 \to \tau^+\tau^-$ with couplings which are not already constrained by other measurements. See Figure 2.5 for the diagrams. The Wilson coefficients are given to be [12]

$$C_S^{LQ} = C_A^{SM} + (g_{1/2}^{LR} - g_{1/2}^{RL}) \tag{2.63}$$

$$C_P^{LQ} = C_P^{SM} + (-g_{1/2}^{LR} - g_{1/2}^{RL}) \tag{2.64}$$

$$C_A^{LQ} = C_S^{SM} + (g_0^{LL} + g_0^{RR} - g_0^{LR} - g_0^{RL} - g_0^{\prime LL} + g_1^{LL}) \tag{2.65}$$

where the superscripts mn indicate the chirality of the lepton and quark fields respectively. The g which contain the unconstrained couplings are given in Table 2.6. This leads to the corresponding branching ratio [12]

$$\begin{aligned}\mathcal{B}^{LQ}(B^0 \to \tau^+\tau^-) &= 5.5 \times 10^{-7}\left[\frac{\tau_B}{1.5ps}\right]\left[\frac{f_B}{200MeV}\right]^2\left[\frac{100\text{ GeV}}{m_{LQ}}\right]^4 \\ &\quad \times \left[|m_{LQ}^2 C_P^{LQ} + \frac{2}{3}m_{LQ}^2 C_A^{LQ}|^2 + \frac{5}{9}|m_{LQ}^2 C_S^{LQ}|^2\right]\end{aligned} \tag{2.66}$$

Thus the branching ratio is enhanced by a factor $(\lambda_{31}\lambda_{33})^2$ but suppressed by a factor $1/m_{LQ}^4$ where LQ is the leptoquark which mediates the decay.

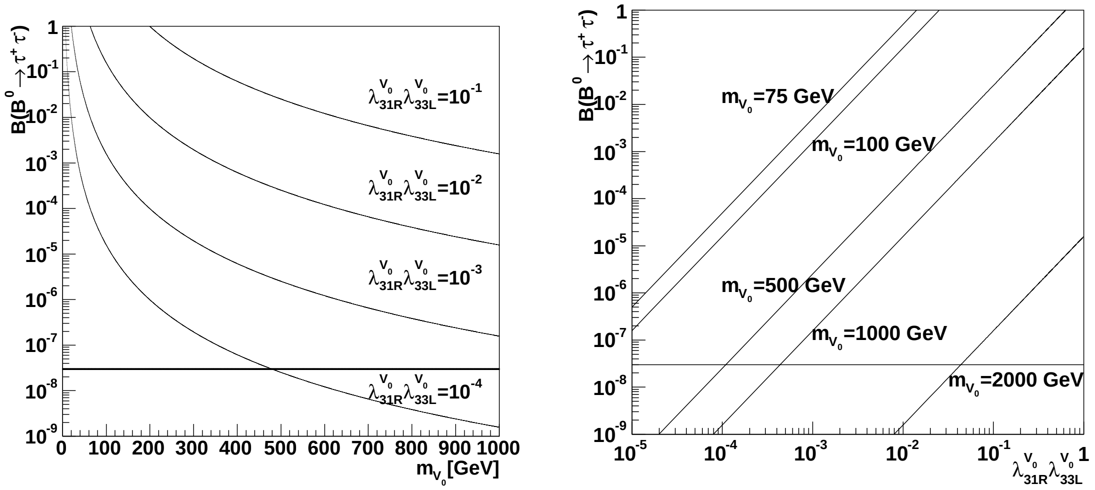

Figure 2.6: Branching ratio $\mathcal{B}^{LQ}(B^0 \to \tau^+\tau^-)$ plotted against m_{V_0} (left) and against $\lambda^{V_0}_{31R}\lambda^{V_0}_{33L}$ (right). The SM value is shown in bold.

If one assumes that the couplings are real and that no more than one leptoquark mediates the decay, the branching ratio for $B^0 \to \tau^+\tau^-$ due to leptoquark exchange can be unambiguously calculated. For example, if the d quark has chirality R and the $\bar{b}$ quark has chirality L, and the vector $SU(2)$ singlet V_0 mediates the decay, then the branching ratio is

$$\mathcal{B}^{LQ}(B^0 \to \tau^+\tau^-) \;=\; 0.28 \times \left[\frac{\lambda^{V_0}_{31R}\lambda^{V_0}_{33L}}{0.01}\right]^2 \left[\frac{100 \text{ GeV}}{m_{V_0}}\right]^4 \qquad (2.67)$$

See Figure 2.6 for the branching ratio as a function of V_0 mass and $\lambda^{V_0}_{31R}\lambda^{V_0}_{33L}$.

Chapter 3

THE BABAR DETECTOR

3.1. Introduction

Overview

In order to measure any B meson property, the B must first be produced in a reliable and cost efficient way. Since the lifetime of the B is too short for direct observation, its properties must be inferred from its stable decay products using particle detection techniques developed over preceding decades in many experimental environments. [33]

B mesons are produced at the Stanford Linear Accelerator Center (SLAC) at the Positron-Electron Project II (PEPII) storage ring by colliding high energy bunches of electron with bunches of positrons. The total number of $B\bar{B}$ events produced is the production cross section times the integrated luminosity, and at the time of writing was approximately 2.3×10^8.

The purpose of the Babar detector is to reconstruct each $B\bar{B}$ event initiated by a collision of the e^+ and e^-. This requires reconstructing particles originating in decays which typically occur on timescales of the weak, electromagnetic and strong

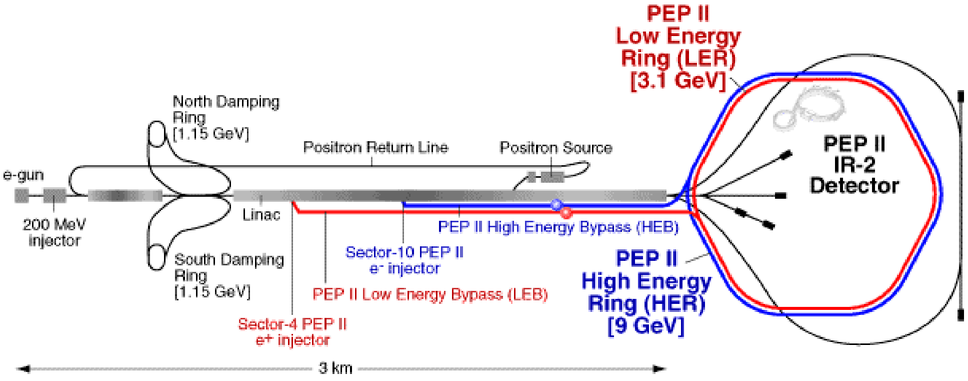
PEP II
Low Energy
Ring (LER)
[3.1 GeV]
North Damping
Ring
[1.15 GeV]
Positron Return Line
Positron Source
e-gun
PEP II
IR-2
Detector
200 MeV
injector
Linac
PEP II High Energy Bypass (HEB)
South Damping
Ring
[1.15 GeV]
Sector-10 PEP II
e- injector
PEP II
High Energy
Ring (HER)
[9 GeV]
PEP II Low Energy Bypass (LEB)
Sector-4 PEP II
e+ injector
3 km

Figure 3.1: The linear accelerator and PEPII storage ring at SLAC.

interactions ($10^{-6}, 10^{-15}, 10^{-22}$ s respectively). This is accomplished by precisely measuring the four vectors x^μ and p^μ and identifying the flavor of particles which live on timescales larger than the time resolution of reliably obtained detector measurements (10^{-9} s). Particles which live on shorter timescales are reconstructed by four vector addition from the longlived particle measurements.

Babar detector design, described in detail in [34] and [1], was optimized primarily for measuring the time dependent CP asymmetry and secondarily for measuring a broad variety of other B meson properties [34]. Unless otherwise specified, design and performance parameters are taken from [1].

The e^+e^- Interaction at PEPII

At PEPII, electrons and positrons bunches are prepared such that their center of mass energy is at the $\Upsilon(4S)$ resonance peak in the reaction $e^+e^- \to \Upsilon(4S) \to B\bar{B}$. The rate of $B\bar{B}$ production is given by $R = \mathcal{L}\sigma_{B\bar{B}}$, where $\mathcal{L}$ is the luminosity and

$\sigma_{B\bar{B}}$ is the production cross section. If f is the frequency of bunch collision, n_i are the bunch populations and σ_i are the transverse bunch dimensions, the luminosity is

$$\mathcal{L} = f\frac{n_1 n_2}{4\pi\sigma_x\sigma_y}. \tag{3.1}$$

Thus a higher event rate is obtained by increasing the bunch populations, increasing the bunch collision frequency and reducing the bunch size. The transverse beam dimension σ_i can be written as a geometric mean of of the emittance ϵ_i, which is determined by the bunch structure and history, and the amplitude $\beta_i^\star$, which is determined by the quadrupole focusing at the interaction point: $\sigma_i = \sqrt{\epsilon_i\beta_i^\star}$.

The Babar detector is located at Interaction Region 2 (IR2) in the collider storage ring PEPII. The design goal of PEPII is to provide as high a luminosity as possible for stable $B\bar{B}$ production at the $\Upsilon(4S)$ resonance while remaining sensitive to the radiation tolerances of the Babar detector. Luminosities are typically of order 10^{33} cm^{-2} s^{-1} but have been sustained at 10^{34} cm^{-2} s^{-1} for extended periods.

The 3 km long linear accelerator at SLAC injects electrons and positrons into the PEPII storage rings, where the beams are stored in stable orbits with bending dipole and focusing quadrupole magnets. The high energy ring (HER) electron current is maintained at 0.7 A while the low energy ring (LER) positron current is maintained at 1.3 A. The electrons and positrons are stored in bunches ordered into a *train*. Each bunch is constrained to occupy a single wavelength, so the maximum number of bunches in a train at PEPII is the circumference divided by the wavelength or about 3500 (PEPII operates at 476 MHz and has a circumference of 2.2 km). In practice, a train carries $\sim$ 1600 bunches spaced temporally at $\sim$ 4 ns intervals. Each bunch typically has populations n of order $10^{10} - 10^{11}$ and transverse widths $\sigma_x = 147$ mm, $\sigma_y = 5$ mm [35].

The LER is injected at lower nominal energy (3.1 GeV) than the HER (9 GeV) so that collisions at the interaction point are boosted forward in order to measure the CP asymmetry in the Babar detector. These beam energies are chosen in order to provide a center of mass energy of 10.58 GeV, the energy of the $\Upsilon(4S)$ resonance peak. For background $e^+e^- \to q\bar{q}$ $(q \neq b)$ and $e^+e^- \to l^+l^-$ studies the beam energies are slightly lowered to produce nominal 10.54 GeV in the center of mass. See Table 3.1 for cross sections for these processes at the $\Upsilon(4S)$ peak.

Since they provide the initial conditions for all events of interest at Babar, the beam energy, luminosity and direction must all be measured to within small error and recorded regularly in a database. The absolute luminosity (to within 1% error) and beam direction (to within 1 MRad) are determined with the frequency and kinematic distributions in e^+e^- and $\mu^+\mu^-$ events in the Babar detector. The beam energies are measured by observing the magnetic field strengths required to bend the beams into collision and yield $5 - 10$MeV systematic errors with 2.3 MeV (LER) and 5.5 MeV (HER) distribution widths.

$e^+e^- \to$	σ/nb	σL/Hz	Trigger Efficiency/%
$b\bar{b}$	1.1	3.2	99.9
$q\bar{q}(q \neq b)$	3.4	10.2	95.8(uds),98.9(c)
e^+e^-	~ 53	159	–
$\mu^+\mu^-$	1.2	3.5	–
$\tau^+\tau^-$	0.9	2.8	92

Table 3.1: Cross sections, production rates (for $\mathcal{L} = 3 \times 10^{33}$ cm^{-2} s^{-1}) and trigger efficiencies at the $\Upsilon(4S)$ resonance [1] [3].

Particle Detection at Babar

The program for any particle detector is, for each stable particle in a given event, to measure the four vectors x^μ and p^μ and identify the particle flavor. For charged particles, three vectors x^i and p^i are obtained by the measuring a *track*, manifested as signals generated by electron-ion or electron-hole pairs, left by the particle traveling in a magnetic field. In a magnetic field B, the three momentum p_t transverse to the magnetic field line is

$$p_t = aqBR \tag{3.2}$$

where the constant $a = 0.3$ GeV^{-1} T^{-1} m^{-1}, q is the charge of the particle, B is the magnetic field strength and R is the described radius of curvature. Thus if B is well mapped and R is obtained with a mathematical track fit, the momentum p_t is known to high accuracy.

In the Babar detector, the tracking system comprises a small silicon vertex tracker located close to the e^+e^- interaction point surrounded by a larger gas and wire drift

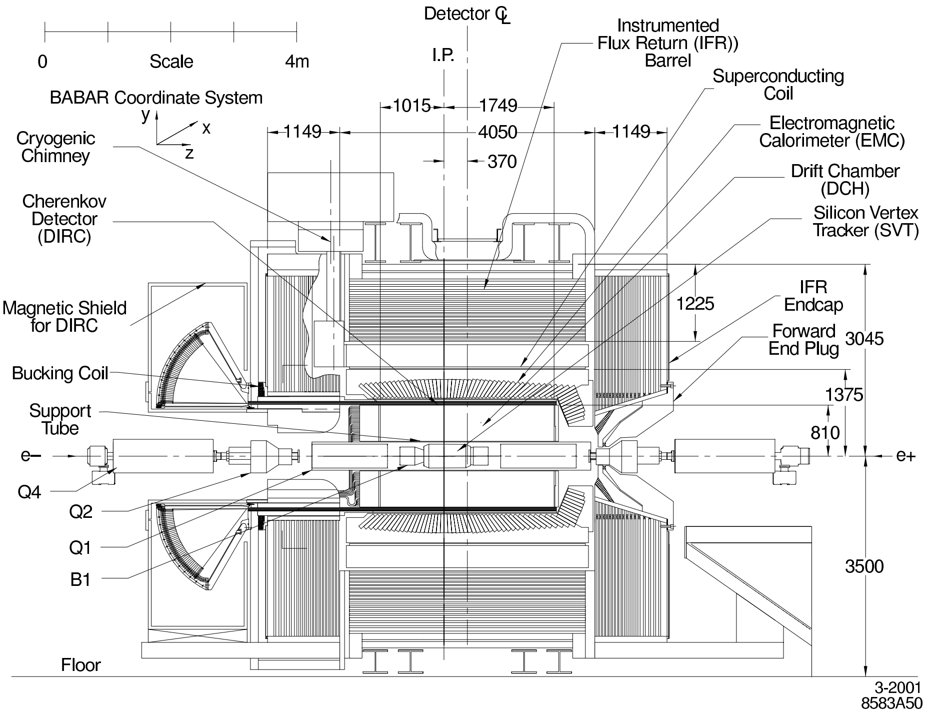
0
Scale
4m
BABAR Coordinate System
y
x
z
Detector ℄
I.P.
Instrumented Flux Return (IFR)) Barrel
Superconducting Coil
Electromagnetic Calorimeter (EMC)
Drift Chamber (DCH)
Silicon Vertex Tracker (SVT)
IFR Endcap
Forward End Plug
Cryogenic Chimney
Cherenkov Detector (DIRC)
Magnetic Shield for DIRC
Bucking Coil
Support Tube
e−
e+
Q4
Q2
Q1
B1
Floor
1015
1749
1149
4050
1149
370
1225
3045
1375
810
3500
3-2001
8583A50

Figure 3.2: Side view of the Babar detector.

chamber which extends radially from the beamline to 81 cm. See Figures 3.2 and 3.3 for side and end views of the Babar detector. The drift chamber provides precise location measurements by measuring the time required for the electron to drift in an electric field to the sense wire. A superconducting solenoid provides the magnetic field necessary for measuring the momentum of transiting charged particles which leave signal tracks of electron-hole pairs (in the vertex tracker) and electron-ion pairs (in the drift chamber).

For neutral particles, the energy p^0 and three vector x^i are measured with the aid of calorimeters. A neutral particle is not deflected by a magnetic field, so the

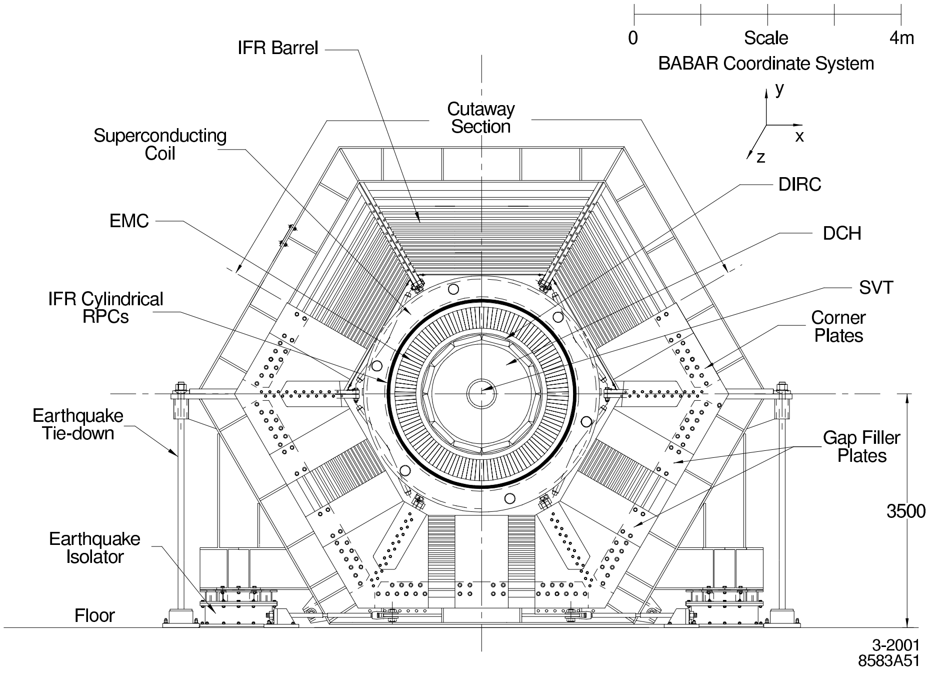
0
Scale
4m
BABAR Coordinate System
y
x
z
IFR Barrel
Cutaway Section
Superconducting Coil
EMC
IFR Cylindrical RPCs
Earthquake Tie-down
Earthquake Isolator
Floor
DIRC
DCH
SVT
Corner Plates
Gap Filler Plates
3500
3-2001
8583A51

Figure 3.3: End view of the Babar detector.

direction of the three momentum can be inferred from the three vector x^i. Electromagnetic calorimeter material induces photons to pair produce e^+e^-, each of which then undergo bremsstrahlung whose daughter photons induce pair production. The process repeats until the mean energy of the electrons is too low to undergo further bremsstrahlung. Thus most of the energy of the incident photon can be fully contained and detected as a *cluster* of bremsstrahlung photons in the calorimeter. The photon energy spatial distribution in clusters of signals also provides information useful in identifying the particle flavor.

Hadronic calorimeters are designed to induce strong interactions in the calorimeter between calorimeter material nuclei and the transiting neutral hadron. The direction x^i of neutral hadrons can be inferred from the spatial distribution of resulting shower energy deposits in a hadronic calorimeter, but in contrast to the electromagnetic calorimeter, only a small and unmeasurable fraction of the incident hadron is detected due to losses to nuclear binding energy.

Surrounding the Babar tracking system and extending radially to about 132 cm is the electromagnetic calorimeter, made up of scintillating crystals which convert bremsstrahlung photons from electromagnetic showers to photons which photomultiplier tubes at the back of each crystal can measure with high efficiency. The hadronic calorimeter extends from the solenoid, which surrounds the electromagnetic calorimeter, to about 4 m. It is a sampling calorimeter which alternates steel plates with active gas filled chambers. Charged particles transiting the chambers create ionization columns which induce a detectable charge on readout strips. Since muons do not interact strongly, they pass through the hadronic calorimeter and thus particle flavor identification is further aided by distinguishing hadronic from muonic tracks.

The four vector measurements x^μ and p^μ are complete (except in the case of neutral hadrons) when a mass hypothesis is assigned with the aid of particle identification devices. At Babar, two processes are exploited for particle identification: Cherenkov radiation of the particle and ionization energy loss due to ionizing atoms adjacent to the particle's trajectory. Both depend on physical processes whose characteristics vary in a known way with the mass of the particle. When a charged particle traverses a medium at higher velocity $v = c\beta$ than light in that medium ($\beta > n^{-1}$), the particle emits Cherenkov radiation at a characteristic angle

$$\theta_C = \cos^{-1}(1/n\beta). \tag{3.3}$$

For Cherenkov particle flavor identification at Babar, quartz bars between the drift chamber and the electromagnetic calorimeter direct Cherenkov photons out to an array of photomultiplier tubes at the backward end of the detector. Additionally, a charged particle with unit charge induces ionization in neighboring atoms along its trajectory with a characteristic energy loss [2]

$$\frac{dE}{dx} = c_1\beta^{-2}\ln\frac{c_2}{\beta^{-2}-1} + c_3\beta^{-2} + c_4 \tag{3.4}$$

where x is the distance traversed and the c_i are constants which depend on the material properties and fundamental physical constants. Charge deposited on sense wires in the Babar drift chamber by ionizing particles aids in particle identification using the dE/dx relation.

Coupled with knowledge of the particle's three momentum, measured by the tracking system, the measured value of β yields the mass of the particle (since $m = p/\gamma c\beta$). If the distributions of these measurements of β are sufficiently narrow, they provide a powerful discriminant between particle with different masses.

The measurements of a particle's x^μ and p^μ at it's origin are fundamentally limited by interactions which occur between the particle's origin and its detection location. Multiple Coulomb scattering of a charged particle in the detector material degrades its energy and introduces an uncertainty in its location. The RMS of the scattering angle is given by [2]

$$\theta_0 = \frac{b_1}{c\beta p}\sqrt{x/X_0}(\ln(x/X_0) + b_2) \tag{3.5}$$

where $b_1 = 0.5168$ MeV, $b_2 = 26.32$ MeV and X_0 is the radiation length of the transited material. Thus, particularly for low momentum particles, a measurement is improved by minimizing the radiation lengths a particle must traverse before it is measured.

An event trigger uses primitive track and cluster information to reject a very large amount of uninteresting beam background from useful physics events. For a list of particles detected in the Babar detector and their properties, see Table 3.2. Detailed descriptions of the Babar tracking, calorimetry, particle identification and trigger systems follow.

Particle	Mass/GeV [2]	$c\tau$/m [2]	Detection
γ	0	∞	Electromagnetic Calorimetry
e	0.000511	∞	Tracking & Particle ID
μ	0.106	659	Tracking & Particle ID
$\pi^{\pm}$	0.140	7.80	Tracking & Particle ID
$K^{\pm}$	0.494	3.71	Tracking & Particle ID
K_L	0.498	15.5	Hadronic Calorimetry
π^0	0.135	2.51×10^{-8}	$\pi^0 \to \gamma\gamma$
K_S	0.498	2.68×10^{-2}	$K_S \to \pi^+\pi^-, 2\pi^0$
D	1.87	3.15×10^{-6}	$D \to vKw\pi$
B	5.28	5.02×10^{-6}	$B \to lDmKn\pi$

Table 3.2: Masses, lifetimes and detection method for particles typically detected in Babar. Longlived particles (above) are directly detected, while shortlived particles (below) are detected by their decay products.

3.2. Charged Particle Tracking

Superconducting Solenoid

The magnetic field necessary for measuring charged particle momenta is generated by a superconducting solenoid located radially at 1.375 m from the beamline. The momentum resolution required for the physics goals yields a design with a 1.5 T magnetic field with uniformity within the active tracking region within 2%. Moreover, the field must not affect the performance of the PEPII dipole bending magnet $B1$ and quadrupole focusing magnets $Q1, Q2$.

The coils making up the solenoid are made of Niobium-Titanium filaments wound into 0.8 mm strands. Sixteen such strands are wound into a cable. The cables are then embedded in aluminum and coiled around the active detector region in two layers,

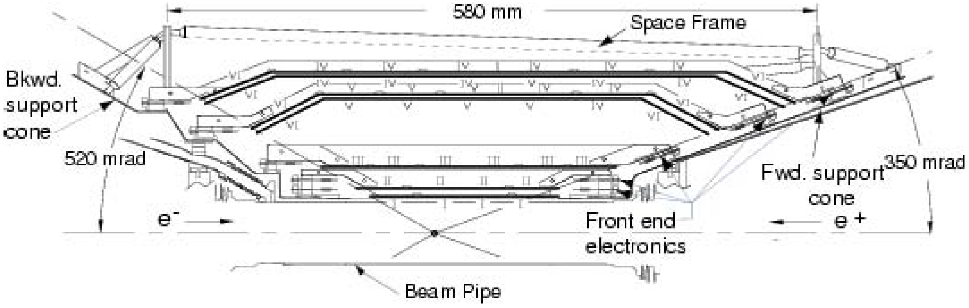

Figure 3.4: Longitudinal section of the Silicon Vertex Tracker..

extending 1.3 km in total. A cryostat filled with liquid He maintains the coils at 4.5 K for superconduction of a 4596 A operating current. A water-cooled bucking coil at the rear of the detector absorbs flux in order to shield the magnets and the Detector for Internally Reflected Cherenkov Radiation. The flux return path outside the coil is provided by a segmented steel structure which also forms the passive component for hadronic calorimetry.

A magnetic field map measured with probes demonstrated that the azimuthal component of the field B_ϕ remained smaller than 1 mT and the field variation in the bend plane of a charged particle in the active tracking area is within 2.5%.

Silicon Vertex Tracker (SVT)

Generally, the goal of the SVT is to measure the position and momentum of charged tracks to high precision as well as providing dE/dx measurements for particle identification. More specifically the primary physics goal of the SVT is to measure the location of B and D meson decay vertices formed by multiple tracks to with single vertex precision of 80 μm along the beamline (or better) in order to measure the time-dependent CP asymmetry to the desired accuracy.

Fitting hits in the SVT together with hits in the DCH yields highly precise track measurements, but a secondary physics goal of the SVT is to measure tracks which pass outside the DCH acceptance yet remain within the SVT acceptance. This standalone tracking enables the measurement of tracks from transition pions from $D^{\star}$ decays, which generally have very low transverse momentum ($p_t < 120$ MeV) in the detector frame due to the high boost $\gamma\beta = 0.56$. Finally, the tracks fitted from hits in the SVT and DCH and extrapolated to the DIRC must yield a low enough error (of the order 1 mr) in order to allow the DIRC to make useful measurements of Cherenkov angles for particle identification.

The design of the SVT is constrained by multiple scattering in the beampipe and silicon of the SVT itself, the Babar-PEPII interface geometry and the expected radiation dose from PEPII beam backgrounds. Material in the beampipe and SVT contributes $4\%X_0$, and Monte Carlo simulations suggest that multiple scattering due to this material imposes a lower useful limit on the intrinsic hit resolution of the silicon microstrip detectors of $10 - 15$ μm. The SVT is mounted on the PEPII $B1$ dipole magnets used for bending the beams, which imposes an acceptance of $\theta \in [20.1^{\circ}, 150.2^{\circ}]$ on the SVT. Finally the detector must withstand an integrated radiation dose of 2 mr from beam backgrounds. For a 1 μs window at $\phi = \pi$, the occupancy peaks at around 15% (5%) in the forward (backward) direction.

Together with the physics goals, these physical constraints and the desire to minimize cost motivated a five-layer SVT design constructed with 340 silicon microstrips with 0.96 m^2 active silicon area covering 90% of the solid angle and reading out approximately 1.5×10^5 channels. The layers are at $32, 40, 54, 91, 114$ mm radially from the beam axis. See Figure 3.4 for a longitudinal profile of the SVT.

In order to measure the spatial location of a hit, each layer has microstrips running parallel to the beam (z-strips) and transverse to the beam (ϕ-strips). For the inner three layers, which require $10 - 15\ \mu m$ hit resolution at normal incidence, simulation studies motivated placing the readout strips at a distance of 100 μm (the *pitch*) from each other and using one floating strip between readout strips in order to reduce the interstrip capacitance. For the outer two layers, which require a lower hit resolution of 40 μm at normal incidence, 200 μm pitch and one floating strip were found to be sufficient. The microstrips comprise 300 μm thick n-type substrates with p^+ and n^+ implants with leakage currents of 50 nA/cm^2, depletion voltages of $25 - 35$ V and bias voltages at 10 V above depletion. These are arranged in modules interconnected mechanically by carbon epoxy rods. Signals are sent from the microstrips via fanouts to ATOM (A Time Over Threshold Machine) integrated circuits mounted on carbon fiber cones which both water cool the integrated circuits and provide the mechanical interface to the $B1$ magnets. The time a microstrip spends over a preset threshold is read out to upon a $L1$ trigger accept signal to the DAQ, enabling a very wide dynamic response due to the quasi-logarithmic relation of time over threshold to signal charge.

Tracks are reconstructed from hits in the SVT by a pattern recognition algorithm. For each microstrip the charge is inferred from the time over threshold signal. Clusters are formed from groups of adjacent charged microstrips within a 200 ns window around an event time determined by the DCH. Clusters are also formed allowing for one uncharged microstrip. The cluster time and charge are then the means over strips making up the cluster. For pitch p, strip charge Q and strip position x the cluster position is determined by

$$x = \frac{x_1 + x_n}{2} + \frac{p}{2}\left(\frac{Q_n - Q_1}{Q_n + Q_1}\right) \tag{3.6}$$

which weights interstrip distances by charge. Tracks are constructed by minimizing the χ^2 in a Kalman fit of all SVT clusters together with hits found in the DCH.

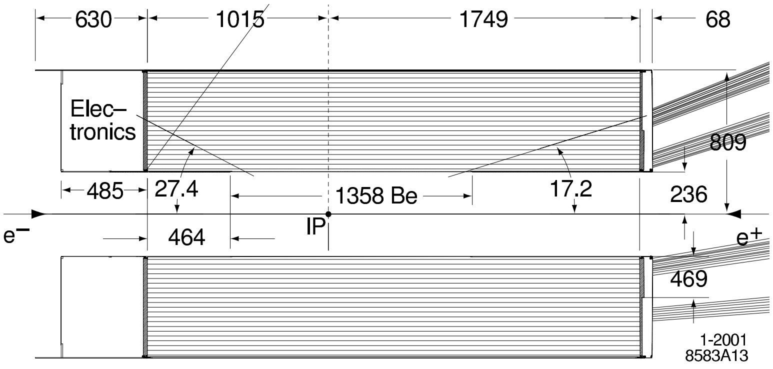

Figure 3.5: Longitudinal section of the Drift Chamber.

Drift Chamber (DCH)

Situated immediately radially outside the SVT, the DCH also also measures the position and direction of charged particle tracks, thereby improving the overall track reconstruction over the reconstruction provided by the SVT alone. The DCH also enables reconstruction of particle decays which occur outside the SVT but within the DCH active volume, in particular the decay $K_S \to \pi^+\pi^-$. Finally, the DCH provides dE/dx measurements for particle identification.

The primary constraints on the DCH are a requirement for the lowest possible multiple scattering in the walls and interior and an ability to withstand the high doses of beam induced radiation in the active volume.

The inner radius of the DCH (see Figure 3.5) lies at the interface with the support tube which houses the SVT. The wall there is a 1 mm thick Be cylinder which is only $0.28\% X_0$ thick. The outer radius of the DCH lies at 81 cm from the beamline and is made of a C fiber material 1.6 mm ($0.6\% X_0$) thick. The endplates are annuli made of Al 24 mm (back) and 12 mm (front) thick. The interior of the DCH holds $28,768$ sense, field, guard and cleaning wires in and ambient mix of He and C_4H_{10} in the ratio $80:20$ at 4 mb flowing at a rate sufficient to replace the entire volume every 36 hours. The gas and wires are $0.2\% X_0$ thick.

Sense wires are made of goldplated W-Re while the other wires are goldplated Al. The field wires are arranged in hexagonal arrays around each sense wire, making up a drift cell approximately $ll.9$ mm $\times 19$ mm. The field wires are held at ground potential and the sense wires at 1960V to guide electrons from ionization clusters onto the sense wires. There are a total of 7104 such cells, arranged into 40 layers which are then formed into 10 superlayers. Of the 40 layers, 24 are arranged at a slight angle from the beamline in order to provide stereo information for determining the z and polar angle θ with respect to the beamline. The axial information is provided in the remaining layers, yielding the track curvature κ, the radial distance from the beamline r and the azimuthal angle ϕ.

Due to the forward boost, the electronics for the DCH are mounted on the backward endplate. The primary purpose of the DCH electronics is, for each cell with a sense wire registering a signal, to provide the drift time (to locate the ionization cluster), the integrated charge collected on the cell's sense wire (to measure dE/dx) and to provide the L1 trigger with hit information. Service boards connect the sense wires to the front end assemblies where the amplifier/digitizer boards provide the

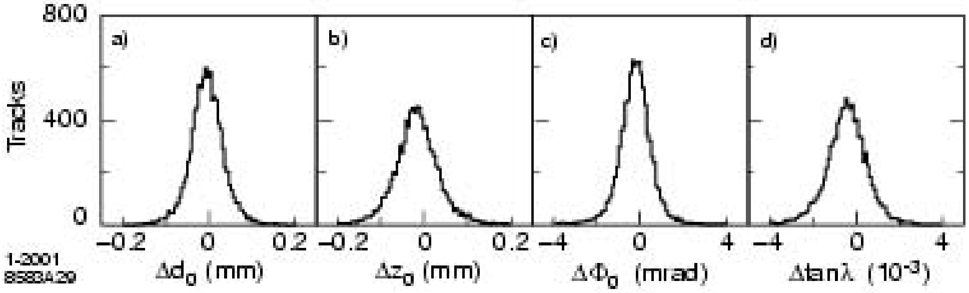

Figure 3.6: Track parameter resolutions obtained from two halves of a cosmic ray event [1].

drift time and analog signal shape. There are 48 amplifier/digitizer boards divided into 16 wedges with three boards per wedge. Inner wedges service 60 channels, outer wedges service 45 channels and intermediate wedges service 48 channels. High voltage is provided to the sense wires by the service boards.

Track Reconstruction

Track reconstruction begins with segments of four DCH sense wire hits. The four hits provide an event beginning time t_0, and together these measurements are used in a Kalman filter algorithm by utilizing a detailed magnetic field map and detector material model to determine the geometrical parameters of a helical trajectory.

The fitted helix is then extrapolated into the rest of the DCH and hits which are consistent with the track candidate are associated to it and the fitting procedure is repeated to provide a refined t_0. Then the refined helix is extrapolated into the SVT and hits there are associated to the DCH track candidate if they are consistent with the expected error using a model of the material in the SVT and the DCH. The track candidate is then refit with all associated hits in both DCH and SVT. Any remaining hits in the SVT which haven't been associated to a DCH track are fit as standalone tracks.

After the final fitting of the helix, it is extrapolated to find the point of closest approach to the beamline. At the point of closest approach, the values d_0, ϕ_0, z_0 (radial distance of closest approach, azimuthal angle and distance along the beamline) and $\omega, \tan\lambda$ (inverse transverse momentum $\omega = 1/p_t$ and dip angle) are determined. The former three quantities determine the spatial location of the track origin while the latter two are sufficient to determine the momentum transverse and parallel to the beamline. Errors on these track parameter measurements are obtained by comparing the two halves of a cosmic ray track passing close to the interaction point (see Figure 3.6). The transverse momentum resolution is found to be

$$\frac{\sigma_{p_t}}{p_t} = (0.13 \pm 0.01)\% p_t + (0.45 \pm 0.03)\% \tag{3.7}$$

If the DCH efficiency is defined as the probability that a track reconstructed in the SVT (and within the DCH acceptance) is also reconstructed in the DCH, then the efficiency is consistently higher than 95% for $p_t > 0.3$ GeV at 1960 V. For $p_t < 0.2$ GeV the DCH efficiency drops dramatically. But the standalone SVT efficiency, obtained with Monte Carlo studies, is higher than 80% down to $p_t = 0.07$ GeV. As discussed in Chapter 1, background events with two oppositely charged particles lost forward

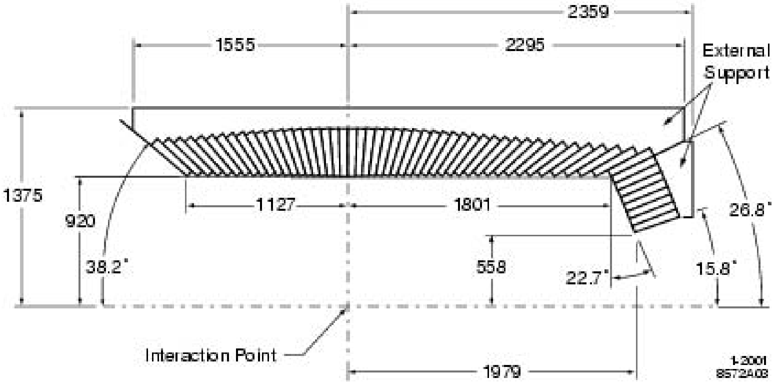
2359
1555
2295
External
Support
1375
920
1127
1801
26.8°
38.2°
558
22.7°
15.8°
Interaction Point
1979
1-2001
8572A03

Figure 3.7: Electromagnetic calorimeter in longitudinal section.

easily mimic the signal. These particles are therefore characterized by low p_t and, if they leave any hits in the tracking system, are reconstructed with low efficiency. The single vertex precision is measured to be 70 μm in the z direction, better than the design goal of 80 μm.

3.3. Electromagnetic and Hadronic Calorimetry

Electromagnetic Calorimeter (EMC)

The purpose of the EMC is to detect and measure electromagnetic showers induced by charged particles and photons in the energy range $[0.02, 9]$ GeV with high energy and angular resolution. The primary physics goals which justify these requirements are semileptonic B flavor tagging for CP studies and high neutral pion and eta detection efficiency and mass widths for rare B decays.

Several constraints influenced the design of the EMC. Simulation studies indicate that rare B decays require the statistical contribution to the energy resolution to be order $1-2\%$. Neutral pion mass widths are dominated by EMC photon energy resolution at low energy and angular resolution at high energy, and both of these must be minimal. Finally, the EMC is constrained to operate within a 1.5 T magnetic field and a high beam-induced radiation environment with stable and reliable performance for its design lifetime.

See Figure 3.7 for a cross section of the EMC. Thallium doped CsI crystal cells provide the scintillation material for photon detection. A total of 6580 CsI(Tl) wedges are inserted into thin carbon fiber composite modules, which are in turn mounted to Al supports and inserted into the crystal support barrel. In the EMC barrel, 48 rings of cells contain a total of 5760 crystals while in the EMC forward endcap, 8 rings contain the remaining 820 crystals. The Al crystal support barrel mounts just outside the DIRC and extends radially 48 cm with inner and outer walls 2.5 cm thick. The whole structure is enclosed in a Faraday cage of thin Al sheets to eliminate stray electric fields.

The crystal cells are tapered wedges 4.5 cm square at the inward end and 6.0cm square at the outward end. Within these crystals the electromagnetic show develops laterally on the order of the Moliere radius (3.8 cm) and longitudinally on the order of the radiation length ($X_0 = 1.85$ cm). Since the wedges are $16.0-17.5X_0$ in radial dimension, all electromagnetic showers are expected to be fully contained (less some leakage) in the active volume of the EMC. Each wedge is polished on its surfaces and wrapped in a thin white reflecting material in order to guide scintillation photons to the backward end of the wedge where two photodiodes are mounted. The photodiodes are 85% quantum efficient at the CsI(Tl) scintillation wavelength 565 nm. Preamplifiers then filter and provide amplification of the signal in inverse relation to the energy, giving high gain to low energy signals. After passing through a comparator and digital conversion, the signal is transmitted to readout modules via optical cables. A L1 trigger accept signal induces readout in a 1 ns window from crystals with a minimum energy of 1 MeV. The average occupancy of the cells is 16%, from noise and beam background.

Nonuniformity in the initial construction and radiation induced damage require that the energy readout from each cell must be calibrated on a weekly basis. Both light yield and leakage corrections are determined from control samples. After 20 fb^{-1} of integrated luminosity, it had been determined that the forward endcap lost 7% in gain from radiation damage [1].

EMC Cluster Reconstruction

Shower clusters are reconstructed from a minimum of one seed cell with energy larger than 10 MeV. Adjacent cells are associated to the cluster if they read out at least 1 MeV or the seed cell energy is at least 3 MeV. Multiple local maxima (or *bumps*) within a cluster may identify two overlapping showers. The energy of a bump b is calculated from a weighted sum over associated crystal cells x, at a distance r_x from the local maximum, by an iterative process:

$$\begin{aligned} E_b &= \sum_{x \in b} w_x E_x && (3.8) \\ w_x &= \frac{E_x e^{-2.5 r_x / r_M}}{\sum_{x\prime \in b} E_{x\prime} e^{-2.5 r_{x\prime} / r_M}} && (3.9) \end{aligned}$$

where r_M is the Molière radius, which is approximately 2.3 cm in CsI. The cell weights w_x are initially set to unity, but are adjusted iteratively based on cell energy and distance from the local maximum. Once the energy distribution $\{E_x\}_{x \in b}$ is converges, the location of the bump is calculated to be a logarithmically energy weighted average

$$\begin{aligned} R_b &= \sum_{x | v_x > 0} v_x R_i && (3.10) \\ v_x &= 4.0 + \ln(E_x / E_b). && (3.11) \end{aligned}$$

The reconstruction concludes by extrapolating tracks from the DCH to the EMC face and computing the distance of the intersection to the nearest bump location. If that distance is larger than a predefined cutoff value, the bump is assumed to be caused by a neutral object.

The energy and angular resolutions of the EMC are obtained with data control samples to be

$$\frac{\sigma_E}{E} = \frac{(2.32 \pm 0.20)\%}{\sqrt[4]{E/GeV}} \oplus (1.85 \pm 0.12)\% \tag{3.12}$$

$$\sigma_\theta/mr = \frac{(3.87 \pm 0.07)}{\sqrt[2]{E/GeV}} \oplus (0.00 \pm 0.05) \tag{3.13}$$

just above design goals. See Figure 3.10a for the photon energy resolution obtained from a variety of control samples.

Instrumented Flux Return (IFR)

The principal goal of the IFR is to detect neutral hadrons (mainly K_L and n) and to identify muons for use in flavor tagging B and D meson decays for CP studies. The general structure of the IFR and the neutral hadron detection performance will be evaluated here, while the muon identification performance will be evaluated in the next section.

The flux return (see Figure 3.8) for the field generated by the superconducting coil is made of a hexagonal barrel and two endcaps. The barrel extends from 1.82 m from the beamline to 3.045 m at the minimal point. The endcaps are 1.149 m thick.

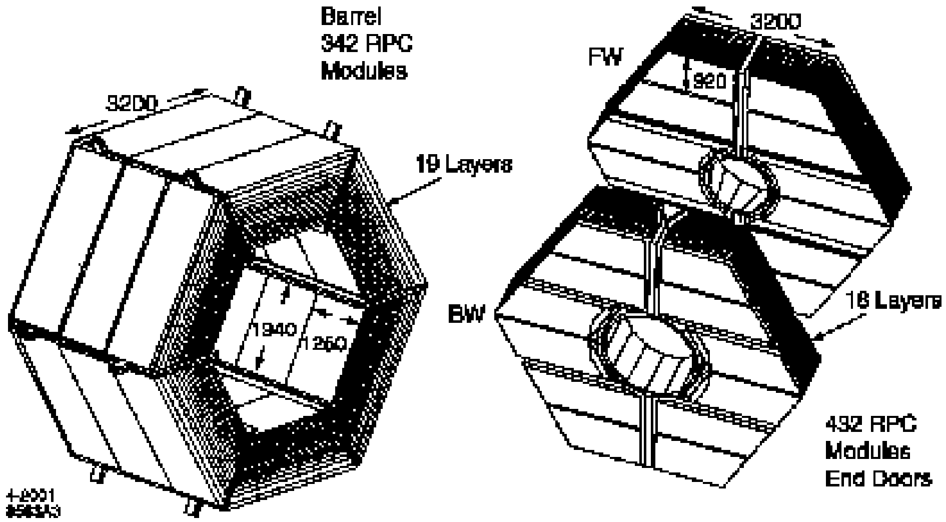
Barrel
342 RPC
Modules
3200
19 Layers
1940
1250
1-2001
8583A3
FW
3200
920
BW
18 Layers
432 RPC
Modules
End Doors

Figure 3.8: The flux return steel barrel (left) and endcaps (right).

The IFR structure provides mechanical support for the detector components inside it. Overall, the steel in the flux returns weighs 870 metric tons.

Twenty steel layers in the barrel, with widths varying between 2 cm and 10 cm, and 19 in the endcaps alternate with air gaps of 3.5 cm width. The steel provides the high Z material necessary to induce interactions between atomic nuclei and neutral hadrons traversing the steel. The charged secondary showers induced by these interactions are detected in the active elements of the hadronic calorimeter known as Resistive Plate Chambers (RPC's). More than 806 planar RPC's are installed in the air gaps in the barrel and endcaps. Cylindrical RPC's are also installed around the EMC barrel and inside the superconducting coil in order to detect hadronic showers which initiate before reaching the IFR.

The RPC is a sandwich of two highly resistive ($10^{11} - 10^{12}$ Ω/ cm) bakelite sheets, each 2 mm thick. The gap between them is filled with Ar, Freon and Isobutane in the proportion 57 : 39 : 5 respectively. The voltage between the bakelite sheets is maintained at 8kV so that, when a charged particle traverses the gap it induces breakdown. The ionization column so generated leaves a charge on Al strips mounted on the back of the bakelite sheets atop a thin graphite layer and another thin insulating layer of mylar. In the barrel, there are 32 $z-$strips and 96 $\phi-$strips for each module. Mounted in the gaps are 3300 electronics Front End Cards (FEC's) servicing a total of approximately 5.3×10^4 channels from the RPC's. The FEC's shape and discriminate pulses from the strips and provide single bits of data for the state of a strip: above or below threshold.

Tracks are extrapolated from the DCH into the IFR using the known magnetic field and expected ionization and scattering losses. If they do not associate with clusters in the IFR, then the clusters are assumed to be from neutral hadron showers. Monte Carlo studies indicate that 64% of all K_L particles with $p > 1$ GeV produce a single hit in the cylindrical RPC's or two or more hits in the planar RPC's. While the neutral hadron direction can be firmly established with the spatial information available from the $z-$ and $\phi-$strips, its energy cannot. In control samples, the detected K_L angular resolution is found to be $\sigma_\theta \sim 60$ mr.

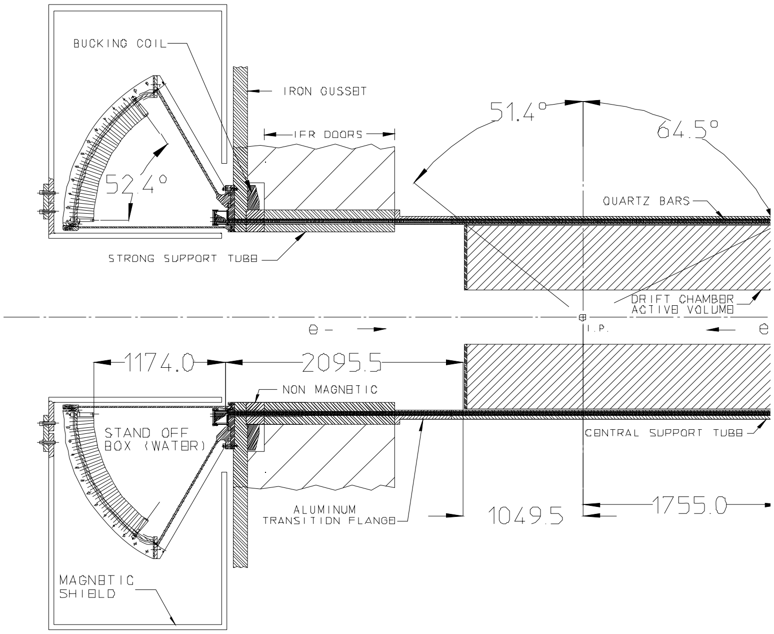
BUCKING COIL
IRON GUSSET
IFR DOORS
51.4°
64.5°
52.4°
QUARTZ BARS
STRONG SUPPORT TUBE
DRIFT CHAMBER ACTIVE VOLUME
e−
I.P.
e
1174.0
2095.5
NON MAGNETIC
STAND OFF BOX (WATER)
CENTRAL SUPPORT TUBE
ALUMINUM TRANSITION FLANGE
1049.5
1755.0
MAGNETIC SHIELD

Figure 3.9: The Detector for Internally Reflected Cherenkov radiation..

3.4. Particle Identification

Detector for Internally Reflected Cerenkov Radiation (DIRC)

The primary purpose of the DIRC is to provide separation between different particle species e, μ, π, K, p. The design goal was to obtain 4σ separation between π and K in order to tag the flavor of B mesons for CP studies in the momentum range above 0.7 GeV, where dE/dx measurements provided by the tracking system begin to lose separation power, up to 3 GeV. The design also required that the DIRC not substantially reduce the energy resolution in the EMC, the system directly outside the DIRC in the radial direction.

The DIRC is located directly outside the DCH, occupying 8 cm ($17\% X_0$) radially. See Figure 3.9 for a diagram. Within two cylindrical Al shells sit twelve boxes containing bars of fused silica running along the beam direction. The surfaces of these bars are highly polished to induce total internal reflection of photons striking them. Charged particles traversing these silica bars ($n = 1.473$) radiate Cherenkov photons which are propagated to the either end of the DIRC by a series of total internal reflections down the length of the bars.

The forward end of the DIRC is provided with a mirror to reflect the photons to the backward end, where the photons are collected with an array of 896 photomultiplier tubes situated in a standoff box filled with 6000 liters of highly purified water. Each photomultiplier tube is provided with an octagonal light catching device to reflect photons which have initially missed back into a tube. The overall Cherenkov photon efficiency in the DIRC is dominated by the photomultiplier photon efficiency, which yields approximately 28 photoelectrons for each Cherenkov photon emitted by a particle at normal incidence with $\beta = 1$. The photomultiplier tubes operate at 1140 V and provide pulse height and arrival time after amplification and pulse shaping with an eight channel integrated circuit.

Given the spatial location of a photomultiplier tube reading out a signal and the spatial location of the bar traversed by a charged particle which nominally emitted the signal photon, the Cherenkov angles polar θ_C and azimuthal ϕ_C geometrically determine sixteen possible sets of values given the ambiguities introduced by possible reflection paths. For each set (θ_C, ϕ_C), the expected arrival time is computed from tracking data and compared to the measured arrival time. Imposing a 8 ns window around the expected arrival time reduces the set of possible angles to a mean of 3. Combining signals from all photomultiplier tubes yields a distribution of angles which are each fitted for (θ_C, ϕ_C). In dimuon data events, the difference in expected and measured θ_C has a width of 10.2 mr. When all photons for a track are considered, that width is reduced to 2.5 mr. The difference in signal photon timing has a width of 1.7 ns, very close to the intrinsic limit of 1.5 ns imposed by the photoelectron transit time. The π/K separation is found to be 4.2σ at 3 GeV, very close to the design goal. See Figure 3.10b for the Cherenkov angle and timing resolutions obtained from data control samples.

Tracking and Calorimetry in Particle Identification

The tracking systems provide dE/dx measurements (see Figure 3.10c) for charged particles and the EMC provides energy deposition information for all particles interacting there. The IFR (described above) also provides μ/π separation.

Since muons do not interact strongly in the steel plates in the flux return, they are expected to penetrate the entire system with sufficient momentum. Pions, in contrast, will interact on the scale of the interaction length λ of the iron in the steel plates. The parameters found to be useful in discriminating are i) the number of interaction lengths λ traversed in the IFR, ii) the difference between the expected and measured

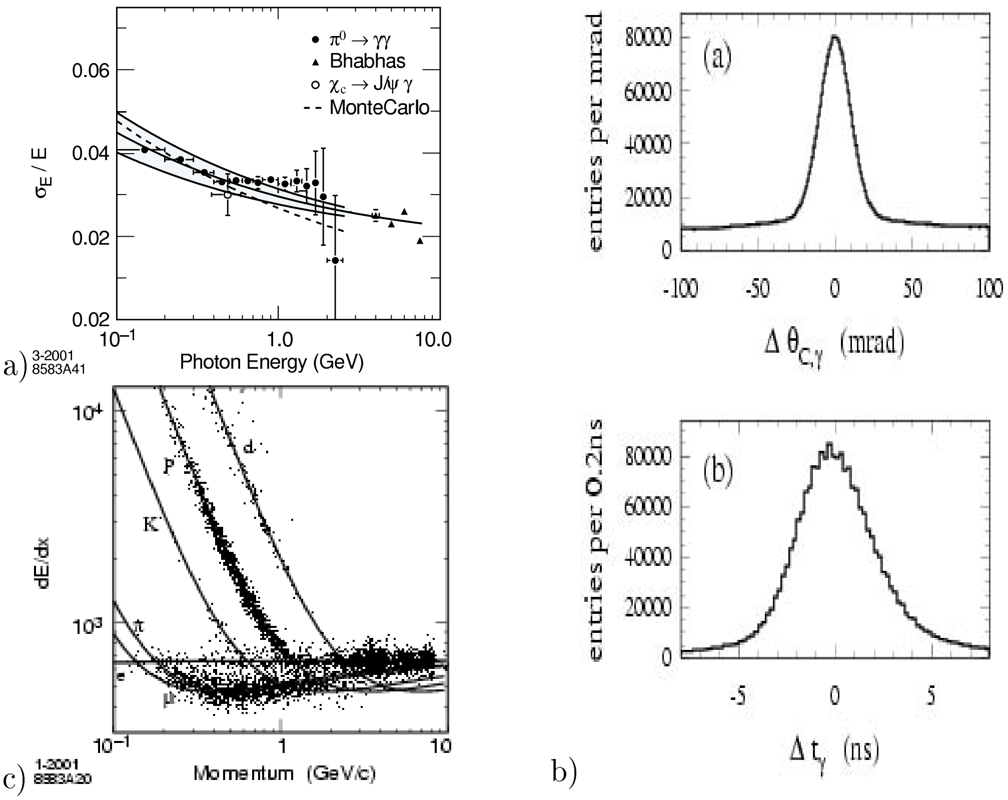

Figure 3.10: Measurement performance for the photon energy in the EMC (a), Cherenkov angle and timing in the DIRC (b) and dE/dx in the DCH (c) [1].

number of interaction lengths traversed ($\Delta\lambda$), iii) the RMS of the IFR clusters, iv) the χ^2 of the distribution of IFR clusters around the extrapolated track and v) the χ^2 of the distribution of clusters around the polynomial fit to the clusters. For muons with $p \in [1.5, 3]$ GeV efficiencies of 90% are obtainable with pion misidentification rates of $6 - 8\%$.

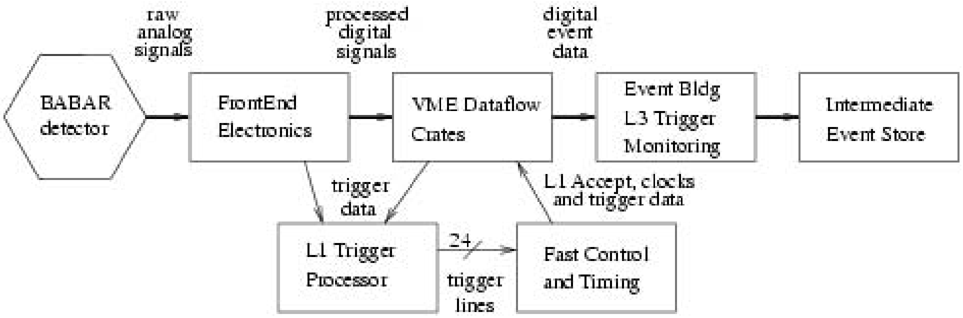
raw
analog
signals
processed
digital
signals
digital
event
data
BABAR
detector
FrontEnd
Electronics
VME Dataflow
Crates
Event Bldg
L3 Trigger
Monitoring
Intermediate
Event Store
trigger
data
L1 Accept, clocks
and trigger data
L1 Trigger
Processor
24
trigger
lines
Fast Control
and Timing

Figure 3.11: Schematic diagram of trigger, data acquisition, event reconstruction and event logging.

3.5. Global Detector Operation

The signals generated by all of the detector subsystems must be collected from the Front End Electronics (FEE), filtered for events of interest, and stored for future study. The detector parameters also need to be monitored and controlled by human operators. These requirements are met with a fast trigger in hardware, a slower trigger in software and a set of processes running on a farm of processors to coordinate data collection and detector control. See Figure 3.11 for a schematic diagram of detector control and data collection.

Beam Background

The HER and LER are brought into collision at the interaction point within the Babar detector in IR2 with quadrupole and bending magnets Qi and $B1$. After the two bunches transit the interaction region they are separated by $B1$ to prevent further collisions. Determining the luminous region produced by bunch collisions is important for rejecting background not originating there. The distribution of points of closest charged particle approach to the beamline, determined with the Babar tracking system in multiple two track events, defines the luminous region.

The beams generate radiation which induces damage in the detector systems and thereby limits the lifetime and efficiency of the detector. The effect of synchrotron radiation, generated by the bending of beam particles in bending magnets, is mostly ameliorated by diverting the photons to a dump. The impact of beam-gas scattering, due to an imperfect vacuum, however, is significant. When beam particles are scattered off of gas molecules they lose energy and are therefore sent preferentially to $\phi = 0, \pi$ by the bending magnets. To a lesser extent, radiative Bhabha events induce electromagnetic showers which generate damage. Finally, a short timescale beam background class includes background due to beam injection into the storage rings, beam loss due to an abort and beam collisions with dust particles. All forms of beam generated background radiation are monitored in the tracking (sensitive to beam gas background) and calorimetry. If levels exceed a preset threshold the tracking system can abort the beams; the electromagnetic calorimeter can inhibit injection only.

Event Trigger

The majority of events generating signals in the Babar detector are noise from beam generated background and must be separated on a very short timescale from the events of interest for either physics studies or diagnostics and calibrations. The purpose of the trigger is to select events of interest with high efficiency ($\epsilon > 0.99$ for $B\bar{B}$) and reject background which, at design luminosity, reaches 20 kHz. The trigger must also be robust with respect to noisy or dead channels.

The Babar event trigger comprises a high frequency hardware and lower frequency software trigger. These are respectively termed the level one trigger (L1) and the level three (L3) trigger, provision having been made for implementing an intermediate trigger level in the future for handling higher luminosity. At design luminosity, the L1 output rate is typically of order 1 kHz and the L3 output rate is typically of order 100 Hz. In both L1 and L3, three independent detector subsystems generate trigger information: the DCH, EMC and IFR.

In L1, the DCH and EMC triggers, each independent and robust, are used for selecting physics events while the IFR trigger is used primarily for calibration with $e^+e^- \to \mu^+\mu^-$ and cosmic ray events. Every 134 ns these triggers provide trigger *primitives* to the Global Level Trigger (GLT), whose function is to construct L1 trigger conditions and determine a trigger time from the primitives. This information is then passed to the Fast Control and Timing System (FCTS), which is configurable to mask or prescale trigger conditions from the GLT. If a trigger condition from the GLT is still valid after masking and prescaling, FCTS issues an L1 Accept signal and the event information in a time window around the trigger time is collected and stored.

The DCH trigger generates three kinds of primitives: short track, long track and high p_t. DCH track segments found within a given superlayer are linked together and classed according to highest superlayer reached. The EMC generates five primitives: low energy, medium energy, high energy, forward hit, backward hit. EMC crystals are grouped into *towers* and each tower energy is summed over crystals with energy above 20 MeV. The tower energies then determine the EMC primitives. If at least four layers in a sector have hits in a 134 ns window, the IFR generates one or more of eight primitives, each of which describes a particular event topology based on hit location and multiplicity.

Upon an L1 Accept signal, signals from the detector lying in an event window around the L1 trigger time are read and analyzed by the L3 software trigger. L3 is implemented on a farm of Sun processors and performs event classification and partial reconstruction to filter the L1 output to select for events of physics and diagnostic interest. The DCH L3 trigger generates the track helix parameters (see above) based on pattern recognition lookup tables generated with Monte Carlo simulations. Similarly, the EMC L3 trigger generates clusters with pattern recognition tables and calculates cluster centroid and shower shape information. The L3 trigger does not use the IFR.

An L3 DCH Physics Accept is generated if at least one track originates radially within 1 cm and longitudinally within 7 cm of the interaction point; or if at least two tracks originate within 1.5 cm and longitudinally within 10 cm of the interaction

Type	Composition/%
$q\bar{q}, l^+l^-(l \neq e)$	22
Other QED, $\gamma\gamma$	18
e^+e^-	25
Beam Background	35

Table 3.3: Composition of the L3 Physics Accept sample at $\mathcal{L} = 2.6 \times 10^{33}$ cm^{-2} s^{-1} [1].

point. An L3 EMC Physics Accept is generated if at least two clusters each have more than 350 MeV energy and the total cluster invariant mass is 1.5 GeV or more; or if at least four clusters are obtained and the total cluster invariant mass is 1.5 GeV or more. L3 Accepts are also issued for event topologies consistent with calibration and diagnostic e^+e^-, $e^+e^-\gamma$, $\gamma\gamma$ and cosmic ray events.

At $L = 2.6 \times 10^{33}$ cm^{-2} s^{-1}, the L3 Physics Accept frequency is 73 Hz while the L3 Diagnostics Accept frequency is 49 Hz. The composition of events passing the L3 Physics Accept is found in Table 3.3.

Event Data Processing and Detector Control

The computing environment necessary for efficient data collection and detector control requires support of L1 and L3 trigger design frequencies, calibration and diagnostic functionality, data quality monitoring and physical detector parameter (high voltage, gas flow, accelerator) monitoring. All of this must be coordinated with a simple user interface for detector control and efficient database management.

The Front End Electronics (FEE) are physically located on the detector and connected by optical cables to the L1 trigger hardware and the data acquisition VME crates termed Read Out Modules (ROMs). Upon an L1 Accept from FCTS, the software running on the ROMs collects signal information from the FEE and, after ensuring that the L1 Accept t_0 is synchronized with signal information from the FEE, passes event information on to a farm of 32 processors running software for Online Event Processing (OEP) and the L3 trigger. Basic event parameters generated in OEP are logged and monitored in realtime for comparison to normative reference sets to ensure high data quality. OEP archives event information for events satisfying an L3 Accept to a logging process running on a dedicated server for Offline Prompt Reconstruction (OPR). After OPR, the data are ready for physics analysis.

Detector control is effected in Online Run Control (ORC) with the use of Experimental Physics and Industrial Control System (EPICS) software, which interfaces directly with hardware signals from the detector and provides a simple GUI interface to the operator. Independent processes (component *proxies*) interface the dataflow and OEP processes with ORC. The proxies present a simple detector state machine (configure, begin run, running) to ORC in order to convey information about dataflow process readiness for data acquisition. The proxies also present detector conditions from ORC to dataflow and OEP and provide the interface between ORC and PEPII.

Chapter 4

SIMULATION AT BABAR

4.1. Introduction

Simulation of the physics at Babar occurs in three distinct stages: primary event generation, particle propagation through detector material and finally the electronics response and trigger simulation. See Figure 4.1 for a diagram of the simulation stages.

Event generation is carried out by generators designed specifically for the process required in the event. EvtGen [36] simulates B physics at the $\Upsilon(4S)$ resonance and was written specifically for B physics experiments. Jetset [37] simulates hadronic continuum $e^+e^- \to q\bar{q}$ for $q = u, d, s, c$. For QED processes $e^+e^- \to e^+e^-$ and $e^+e^- \to \mu^+\mu^-$ Babar employs the generator BkQED, and for $e^+e^- \to \tau^+\tau^-$ the generator is KoralB [38]. Other processes (cosmics rays, initial state radiation, gamma gamma events) are handled by specialized programs.

All generators produce the underlying event four vectors in the center-of-momentum frame. Before passing the underlying event on to particle propagation through the detector, the event is rotated and boosted to the match the PEPII beam parameters and placed spatially at the interaction point relative to the detector frame. Then the event is stored in the StdHep format [39] for detector simulation.

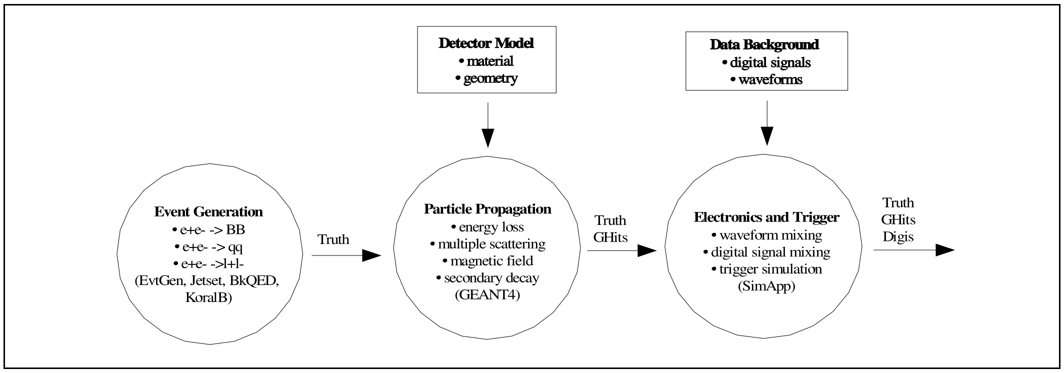
Detector Model
• material
• geometry
Data Background
• digital signals
• waveforms
Event Generation
• e+e- -> BB
• e+e- -> qq
• e+e- ->l+l-
(EvtGen, Jetset, BkQED, KoralB)
Truth
Particle Propagation
• energy loss
• multiple scattering
• magnetic field
• secondary decay
(GEANT4)
Truth
GHits
Electronics and Trigger
• waveform mixing
• digital signal mixing
• trigger simulation
(SimApp)
Truth
GHits
Digis

Figure 4.1: The three stages of simulation at Babar.

The detector physics simulation is carried out by Bogus (Babar Object-oriented Geant4-based Unified Simulation). Bogus is a layer of code written above the more generalized program GEANT4 (GEometry ANd Tracking) [40], a toolkit for simulating the propagation of particles through matter in user-specified geometries, which specializes it to the Babar detector.

Bogus takes the event in StdHep format at time t_0 and steps it forward in time through the detector by simulating the effects of the magnetic field, ionization energy loss, multiple scattering and secondary decays. A highly detailed model of the detector geometry and materials is necessary for accurate simulation of these processes, and therefore must be continually updated to reflect the changing configuration of the detector. Localized energy deposition (*GHits*) in all parts of the detector are saved together with the original event information (Monte Carlo *truth*) for simulation of the electronics response to the GHits in the final phase of simulation.

For all detector systems, the simulated digital response to GHits is encoded in *digis*. For the EMC, which employs analog signal response, the waveform response to GHits is simulated. Using data stored from randomly triggered real events, background digis and waveforms due to electronics noise and spurious physics processes are mixed together with those due to the underlying physics event. The mixed digis and waveforms are then subjected to the L1 trigger simulation.

After all three stages of simulation, the event record contains the Monte Carlo truth, the GHits, the mixed digis and waveforms and the L1 trigger response. The L3 software trigger is applied and reconstruction of simulation event particle candidates then proceeds precisely as it does on real data. In the following sections we will focus first on the EvtGen simulation of signal and background events. Next we consider the GEANT4 simulation of the static and dynamic properties of the Babar detector which evolves the primary event.

4.2. **Primary Event Simulation**

The EvtGen Event Generator

The task of generating the full decay tree of two B mesons at the $\Upsilon(4S)$ resonance is allocated at Babar to EvtGen, an object-oriented C++ package written with experience obtained from previous B physics experience at CLEO.

Particle	ID	Mass/GeV	$\Delta\Gamma$ /GeV	ΔM/GeV	3Q	2S	$c\tau$/mm	L-KC
e-	11	0.000510999	0	0	-3	1	0	11
e+	-11	0.000510999	0	0	3	1	0	0
nu_e	12	0	0	0	0	1	0	12
anti-nu_e	-12	0	0	0	0	1	0	0
mu-	13	0.1056584	0	0	-3	1	658654.	13
mu+	-13	0.1056584	0	0	3	1	658654.	0
nu_mu	14	0	0	0	0	1	0	14
anti-nu_mu	-14	0	0	0	0	1	0	0
tau-	15	1.7770	0	0	-3	1	0.0872	15
tau+	-15	1.7770	0	0	3	1	0.0872	0
nu_tau	16	0	0	0	0	1	0	16
anti-nu_tau	-16	0	0	0	0	1	0	0
pi0	111	0.134976	0	0	0	0	0	111
pi+	211	0.139570	0	0	3	0	7804.5	101
pi-	-211	0.139570	0	0	-3	0	7804.5	0
rho0	113	0.7685	0.151	0.48	0	2	0	131
rho+	213	0.7685	0.151	0.48	3	2	0	121
rho-	-213	0.7685	0.151	0.48	-3	2	0	0
K0	311	0.49767	0	0	0	0	0	102
anti-K0	-311	0.49767	0	0	0	0	0	0
K_S0	310	0.49767	0	0	0	0	26.762	222
K_L0	130	0.49767	0	0	0	0	15510.	221
K+	321	0.49368	0	0	3	0	3713.	103
K-	-321	0.49368	0	0	-3	0	3713.	0
D+	411	1.8693	0	0	3	0	0.315	104
D-	-411	1.8693	0	0	-3	0	0.315	0
D0	421	1.8645	0	0	0	0	0.1234	105
anti-D0	-421	1.8645	0	0	0	0	0.1234	0
D*+	413	2.010	0.000080	0.0004	3	2	0	124
D*-	-413	2.010	0.000080	0.0004	-3	2	0	0
D*0	423	2.0067	0.000061	0.0003	0	2	0	125
anti-D*0	-423	2.0067	0.000061	0.0003	0	2	0	0
B0	511	5.2794	0	0	0	0	0.462	107
anti-B0	-511	5.2794	0	0	0	0	0.462	0
B+	521	5.2791	0	0	3	0	0.502	108
B-	-521	5.2791	0	0	-3	0	0.502	0
Upsilon(4S)	70553	10.57500	0.019	0.014	0	2	0	404

Table 4.1: Particle properties used by EvtGen for a few select particles. Taken from the EvtGen evt.pdl file.

EvtGen maintains the particle properties required for simulation in the evt.pdl file. The particle number (according to Particle Data Group convention), particle mass, width, maximum mass error, charge, spin, lifetime, and Lund particle number are maintained in this file, which can be easily updated with most recent measurements. See Table 4.1 for the evt.pdl listings for a few select particles. Particles are represented as scalars (spin 0, one state), Dirac particles (spin 1/2, two states), neutrinos (spin 1/2, one state), massive vectors (spin 1, three states), massless vectors (spin 1, two states), and tensors (spin 2, five states).

A complete decay list for B and D mesons is contained in the DECAY.DEC file, which defines the branching ratio and decay model for each known decay of stable particles found at the $\Upsilon(4S)$. See Tables 4.3 for a select list of B decays and 4.5 for a select list of D decays taken from the DECAY.DEC file. Given a B meson to fully decay, EvtGen first consults the DECAY.DEC file to determine which specific decay to implement based on the branching ratios maintained for each. Then kinematics are generated according to phase space and subject to requirements (for example, spin correlations) imposed by the decay model specified in DECAY.DEC. Then for each daughter particle which isn't stable, the process is repeated.

Three categories of decay model are implemented in EvtGen. The *incoherent* models do not include spin correlations between decay products and generate spin averaged particles. The generic phase space model PHSP and the JETSET model, which implements the interface with Jetset, are the two primary incoherent models.

For this category EvtGen simply generates decay daughter particles and initializes their kinematic values randomly such that they satisfy energy and momentum conservation laws. In the JETSET model, EvtGen passes the decay to Jetset to simulate hadronic showering. Decays in which the initial and finals states contain only scalar particles use incoherent models since there are no spin correlations to simulate. Approximately 40% of all B decays are decayed with incoherent models.

The *probability* models also do not include spin correlations between daughter particles, which are unpolarized. Such models are slightly more sophisticated than the incoherent models in that, after generating daughter particles and initializing phase space, they define probabilities based on the generated kinematics for use in a veto algorithm. If the probability assigned to the generated kinematics falls below some randomly generated number on the unit interval, the kinematics are rejected and regenerated repeatedly until the kinematics pass the veto. For example, the model D_DALITZ, which models $D \to K\pi\pi$, is a probability model. The probabilities in this model are obtained from the density of the Dalitz plot of $m^2_{K\pi_1}$ against $m^2_{K\pi_2}$ obtained experimentally from the MARK III and E691 experiments, ensuring that the K^* resonance contributions are accurately modeled. Only a handful of decays in EvtGen are generated with probability models.

Most decays in EvtGen are implemented with *amplitude* models. These fully include all spin correlations in the kinematics because they employ the full amplitudes for the decay. For example, consider the decay $a \to b(\to b_1 b_2)c(\to c_1 c_2)$ [41]. The example generalizes easily. Denote the spin degrees of freedom for b by λ_b and for c by λ_c. Let $\mathcal{M}_p$ denote the amplitude for the process p, which is specified in the decay model for p. First generate kinematics for the a decay and apply the veto algorithm using the probability $P_a = |\mathcal{M}_{a\to bc}|^2$ for the specified a decay. Kinematics are regenerated until they pass the veto algorithm using P_a. Next generate $b \to b_1 b_2$ kinematics, the spin density matrix for b and the corresponding probability for the $b \to b_1 b_2$ decay:

$$\rho_b^{\lambda_b \lambda_b'} = \sum_{\lambda_c} \mathcal{M}_{a\to bc}^{\lambda_b,\lambda_c} (\mathcal{M}_{a\to bc}^{\lambda_b',\lambda_c})^{\star} \tag{4.1}$$

$$P_b = \frac{1}{Tr\rho_b} \sum_{\lambda_b \lambda_b'} \rho_b^{\lambda_b \lambda_b'} \mathcal{M}_{b\to b_1 b_2}^{\lambda_b} (\mathcal{M}_{b\to b_1 b_2}^{\lambda_b'})^{\star}. \tag{4.2}$$

EvtGen applies the veto algorithm using P_b and regenerates kinematics as necessary. Finally, EvtGen generates kinematics for $c \to c_1 c_2$, the spin density matrix for c and the probability for the $c \to c_1 c_2$ decay:

$$\tilde{\rho}_b^{\lambda_b,\lambda_b'} = \mathcal{M}_{b\to b_1 b_2}^{\lambda_b} (\mathcal{M}_{b\to b_1 b_2}^{\lambda_b'})^{\star} \tag{4.3}$$

$$\rho_c^{\lambda_c \lambda_c'} = \sum_{\lambda_b,\lambda_b'} \tilde{\rho}_b^{\lambda_b,\lambda_b'} \mathcal{M}_{a\to bc}^{\lambda_b,\lambda_c} (\mathcal{M}_{a\to bc}^{\lambda_b',\lambda_c'})^{\star} \tag{4.4}$$

$$P_c = \frac{1}{Tr\rho_c} \sum_{\lambda_c \lambda_c'} \rho_c^{\lambda_c \lambda_c'} \mathcal{M}_{c\to c_1 c_2}^{\lambda_c} (\mathcal{M}_{c\to c_1 c_2}^{\lambda_c'})^{\star}. \tag{4.5}$$

The spin correlations between b and c are captured in the ρ_b, $\tilde{\rho}_b$ and ρ_c spin density matrices. EvtGen applies the veto algorithm using P_c and regenerates kinematics as necessary. Many amplitude models take parameters specified in the DECAY.DEC file. For example, the SVV_HELAMP model takes six parameters: the magnitudes and phases for each coefficient in the helicity state expansion of a vector particle. In the HQET decay model for semileptonic decays $B \to D^{\star} l \nu_l$, the parameters are the form factor slope ρ_A^2 and form factor ratios R_1 and R_2. Their default values are taken from CLEO measurements [4].

For final state QED corrections, EvtGen employs the package PHOTOS [42]. Bremsstrahlung from any final state particle in a decay process p introduces a photon and alters the four-momentum of the particle, reducing the width Γ_p at higher momenta and increasing it at lower momenta. If $x \equiv E/E_{max}$ is the energy fraction of the particle, the differential width without bremsstrahlung $d\Gamma_p^0/dx$ is modified by a correction term $d\Gamma_p/dx - d\Gamma_p^0/dx$. In two decay processes ($B^+ \to D^0 e^+ \nu(\gamma)$ and $\tau \to e\nu\bar{\nu}(\gamma)$) where the analytical expression for $d\Gamma_p/dx$ is known to $\mathcal{O}(\alpha^2)$, the agreement between the PHOTOS correction term and the analytical correction factor is good to 1% [43]. Bremsstrahlung with two or more photons is not implemented, nor is interference due to multiple charged particles in the final state. Bremsstrahlung simulation is important for the $B^0\tau^+\tau^-$ analysis described in Chapters 5-7 because the residual photon energy unassigned to reconstructed particles is a strong indication in the background that unreconstructed neutral pions are present, and it is required to be minimal for the signal selection. If the bremsstrahlung simulation was deficient, it would be necessary to assign a systematic error.

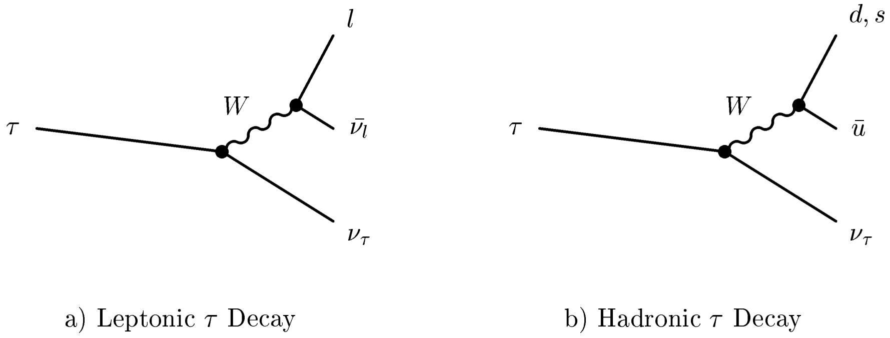

a) Leptonic τ Decay

b) Hadronic τ Decay

Figure 4.2: Feynman diagrams for the two dominant classes of tau decay. Leptonic decays ($\tau \rightarrow e\nu_e\nu_\tau$ and $\tau \rightarrow \mu\nu_\mu\nu_\tau$) account for approximately 35.2% of all tau decays, while hadronic decays of the type depicted ($\tau \rightarrow \pi\nu_\tau$, $\tau \rightarrow \rho\nu_\tau$, $\tau \rightarrow a_1\nu_\tau$, $\tau \rightarrow K\nu_\tau$ and $\tau \rightarrow K^\star\nu_\tau$) account for approximately 57.2% of all tau decays.

Signal Simulation: Tau Physics and $B^0 \rightarrow \tau^+\tau^-$ in EvtGen

The tau lepton decays via the weak interaction with a lifetime of 290.6 ± 1.1 fs. Tau decays may be classified as either leptonic or hadronic (semileptonic decays have not been observed). In both cases, the tau undergoes a transition $\tau \rightarrow W\nu_\tau$. The W boson then couples to either a $l\nu_l$ pair (leptonic) or a qq' pair, which hadronizes into a meson (hadronic). See Figure 4.2 for the Feynman diagrams for tau decay. The tau mass is 1.7770 ± 0.0003 GeV, forbidding decays to top, bottom and charm mesons but allowing decays to strange and up/down mesons and both muons and electrons.

The leptonic decays $\tau \to e\nu_e\nu_\tau$ and $\tau \to \mu\nu_\mu\nu_\tau$ are theoretically very clean and straightforward to model. In EvtGen they are implemented with the amplitude model TAULNUNU. The W propagator

$$P^{\mu\nu}(q) \quad = \quad i\frac{-g^{\mu\nu} + q^\mu q^\nu/m_W^2}{q^2 - m_W^2} \tag{4.6}$$

can first be approximated. Since the virtual W produced in the $b \to Wq$ transition is very light compared to the onshell W ($q^2 << m_W^2$), the W propagator can be approximated by $P^{\mu\nu}(q) \approx ig^{\mu\nu}/m_W^2$. Then using the Fermi constant $G_F \equiv (\sqrt{2}/8)g_w^2/m_W^2$, the amplitude for leptonic decays may be written as a product of two leptonic currents

$$\mathcal{M}_{\tau\to l\bar{\nu}\nu} \quad = \quad \frac{G_F}{\sqrt{2}} l^\mu L_\mu \tag{4.7}$$

$$L^\mu \quad = \quad \langle\nu_\tau|\gamma^\mu(1-\gamma^5)|\tau\rangle \tag{4.8}$$

$$l^\mu \quad = \quad \langle\nu_l|\gamma^\mu(1-\gamma^5)|l\rangle \tag{4.9}$$

where the τ, l are represented as Dirac particles (spin 1/2, two states) and the ν_τ, ν_l are represented as neutrinos (spin 1/2, one state) in EvtGen. Since the overall multiplicative factor in any amplitude in EvtGen is irrelevant to the decay kinematics, the factor is neglected and each amplitude is normalized to its maximum value over phase space. QED radiative corrections to the partial width are of order $\alpha(m_\tau^2)$, but these are accounted for with PHOTOS. The correction for the full W propagator is of order m_τ^2/m_W^2 [44].

The hadronic tau decays are considerably more complex than the leptonic decays. Several effects alter the contribution to the total tau width from the many hadronic decay channels: Cabibbo suppression, phase space suppression, helicity suppression and isospin suppression [44]. These effects are neglected in the EvtGen amplitudes but are included implicitly in the widths defined by the branching ratios in DECAY.DEC.

The strange decay widths for $\tau \to K\nu_\tau$ and $\tau \to K^\star\nu_\tau$ are Cabibbo suppressed relative to the nonstrange decay widths by a factor $|V_{us}/V_{ud}|^2 \approx 0.05$. Since the phase space goes continuously to zero at the tau mass, the heavy meson decays are phase space suppressed relative to the light meson decays. The suppression is greater for $J = 0$ than it is for $J = 1$ mesons:

$$d\Gamma \propto (1 - q^2/m_\tau^2)^2(1 + 2q^2/m_\tau^2)^J \tag{4.10}$$

for meson transfer momentum q and meson spin J [44].

Since the W couples to lefthanded quarks and righthanded antiquarks, hadronic tau decays predominantly produce mesons whose valence quarks have opposite helicity and are therefore in a $J = 1$ state. The nonzero quark masses allow a helicity suppressed $J = 0$ contribution to final states, with a partial width suppression factor of order $(m_q + m_{q'})/M$ where M is the meson mass [44]. Finally, isospin effects suppress scalar meson decay widths over pseudoscalar meson decay widths by a factor $(m_q - m_{q'})^2/(m_q + m_{q'})^2$

The amplitude for hadronic tau decays may be written as a product of a leptonic current with a hadronic current

$$\mathcal{M}_{\tau\to h\nu} = \frac{G_F}{\sqrt{2}} V_{uq} h^\mu L_\mu \quad (4.11)$$

$$L^\mu = \langle \nu_\tau | \gamma^\mu (1-\gamma^5) | \tau \rangle \quad (4.12)$$

$$h^\mu_{J=0} = f_h q^\mu \quad (4.13)$$

$$h^\mu_{J=1} = f_h \epsilon^\mu \quad (4.14)$$

for $q = d, s$. Here V_{uq} is the CKM element V_{ud} or V_{us}, q is the momentum transfer and ϵ is the meson polarization vector. Since QCD final state interactions greatly complicate the amplitude calculation, the hadronic current is parameterized with decay constants f_h which describe the overlap of the valence quarks in the meson.

In EvtGen, the $J = 0$ hadronic decays ($\tau \to \pi\nu_\tau$ and $\tau \to K\nu_\tau$) are modeled with the TAUSCALARNU (scalar represented by spin 0, one state) model while the $J = 1$ hadronic decays ($\tau \to \rho\nu_\tau$, $\tau \to a_1\nu_\tau$ and $\tau \to K^\star\nu_\tau$) are modeled with the TAUVECTORNU (vector represented by spin 1, three states) model. Nonresonant decays with two and three pion final states are modeled with the JETSET model.

In some simulated data at Babar[1], the hadronic decays $\tau \to \rho\nu_\tau$ and $\tau \to a_1\nu_\tau$ were implemented with the TAUHADNU model rather than the TAUVECTORNU model. In the TAUHADNU model, the hadronic current for resonant two and three pion final states is parameterized by Breit-Wigner resonance shapes. For the two pion final state,

$$h^\mu_{2\pi} = \sqrt{2}F_1^{2\pi}(q^2)(q_1^\mu - q_2^\mu) \tag{4.15}$$

$$F_1^{2\pi}(q^2) = \frac{BW_\rho + \beta BW_{\rho'}}{1+\beta} \tag{4.16}$$

$$BW_\rho = \frac{m_\rho^2}{m_\rho^2 - q^2 - iq\Gamma_\rho(q^2)} \tag{4.17}$$

where the q_1, q_2 are the four momenta of the pions and $q = q_1 + q_2$. For the three pion final state,

$$h^\mu_{3\pi} = -i\frac{2\sqrt{2}}{3f_\pi}BW_{a_1}\left[F_1^{2\pi}(s_1)\left(q_1^\mu - q_3^\mu - q^\mu\frac{q(q_1-q_3)}{q^2}\right)\right] \tag{4.18}$$

$$-i\frac{2\sqrt{2}}{3f_\pi}BW_{a_1}\left[F_1^{2\pi}(s_2)\left(q_2^\mu - q_3^\mu - q^\mu\frac{q(q_2-q_3)}{q^2}\right)\right] \tag{4.19}$$

where $s_1 = (q_2 + q_3)^2$ and $s_2 = (q_1 + q_3)^2$. The parameters β, m_ρ, Γ_ρ, $m_{\rho'}$, $\Gamma_{\rho'}$, m_{a_1} and $\Gamma_{a_1}$are taken from experimental fits to data.

The remaining hadronic tau decays comprise approximately 7.6% of all tau decays and are modeled with either JETSET or PHSP models. See Table 4.2 for a complete list of tau decay modes simulated by EvtGen.

---

[1] Early in the simulation production cycle SP4 the model switched from TAUVECTORNU to TAUHADNU. All subsequent SP cycles use TAUHADNU.

EvtGen uses the SLL amplitude model to simulate $B^0 \to \tau^+\tau^-$. This model is appropriate for the decay of any scalar or pseudoscalar particle to two leptons. The amplitude is written as a product of two currents:

$$\mathcal{M}^{\lambda_1\lambda_2}_{s\to l_1 l_2} = \frac{G_F}{\sqrt{2}} V^{\star}_{qq'} V_{q'q''} L^{\mu} H_{\mu} \tag{4.20}$$

$$L^{\mu} = \langle l_{\lambda_2} | (1-\gamma^5)^{\dagger} \gamma^{\mu} (1-\gamma^5) | l_{\lambda_2} \rangle \tag{4.21}$$

$$H^{\mu} = f p^{\mu}_B \tag{4.22}$$

where f is some multiplicative constant and p^{μ}_B is the B momentum.

In EvtGen,the signal B^0 decay specified in DECAY.DEC is superseded by the specification

```
decay B0
1.0 tau+ tau- PHOTOS SLL
enddecay
```

to implement the $B^0 \to \tau^+\tau^-$ decay with final state radiation and the SLL model. In the `init` method of the `EvtSll` class, SLL ensures that the particle to decay is a scalar (or pseudoscalar) (spin 0, one state) and that there are two daughters, each a Dirac particle (spin 1/2, two states). In the `decay` method, SLL initializes phase space by assigning momenta to the taus, constructs the leptonic V-A current and the B four momentum, then returns the amplitude $\mathcal{M}^{\lambda_1\lambda_2}_{B^0\to\tau^+\tau^-}$.

BR	Decay Mode	Decay Model
0.1778	e- anti-nu_e nu_tau	PHOTOS TAULNUNU
0.1731	mu- anti-nu_mu nu_tau	PHOTOS TAULNUNU
0.1095	pi- nu_tau	TAUSCALARNU
0.2531	pi- pi0 nu_tau	TAUHADNU
		-0.108 0.775 0.149 1.364 0.400
0.09234	pi- pi- pi+ nu_tau	TAUHADNU
		-0.108 0.775 0.149 1.364 0.400 1.23 0.4
0.0910	pi0 pi0 pi- nu_tau	TAUHADNU
		-0.108 0.775 0.149 1.364 0.400 1.23 0.4
(0.2515)	rho- nu_tau	TAUVECTORNU
(0.1790)	a_1- nu_tau	TAUVECTORNU
0.00686	K- nu_tau	TAUSCALARNU
0.0134	K*- nu_tau	TAUVECTORNU
0.0450	nu_tau pi- pi+ pi- pi0	JETSET 41
0.0100	nu_tau pi- pi0 pi0 pi0	JETSET 41
0.0015	nu_tau K- pi- K+	JETSET 41
0.0015	nu_tau K0 pi- anti-K0	JETSET 41
0.0015	nu_tau K- pi0 K0	JETSET 41
0.0005	nu_tau K- pi0 pi0	JETSET 41
0.0050	nu_tau K- pi+ pi-	JETSET 41
0.0055	nu_tau pi- anti-K0 pi0	JETSET 41
0.0017	nu_tau eta pi- pi0	JETSET 41
0.0013	nu_tau gamma pi- pi0	JETSET 41
0.0009	nu_tau pi- pi- pi+ pi0 pi0	PHSP
0.0008	nu_tau pi- pi- pi- pi+ pi+	PHSP
0.0003	nu_tau pi- pi- pi- pi+ pi+ pi0	PHSP
0.0005	nu_tau pi- pi- pi+ pi0 pi0 pi0	PHSP
0.0010	nu_tau pi- pi0 pi0 pi0 pi0	PHSP
0.0039	nu_tau pi- omega pi0	JETSET 41
0.0010	nu_tau K- K0	JETSET 41
0.0010	nu_tau K- omega	JETSET 41

Table 4.2: The complete list of tau decay modes simulated by EvtGen together with their branching ratios and decay models. The branching ratios sum to unity. The parameters in the TAUHADNU decay model are β, the ρ mass and width, the ρ' mass and width, and the a_1 mass and width. The branching ratios in brackets () signify that the models for $\tau \to \rho\nu_\tau$ and $\tau \to a_1\nu_\tau$ were changed from TAUVECTORNU to TAUHADNU between simulation production cycles. Taken from the EvtGen DECAY.DEC file.

In order to validate the simulation of $B^0 \to \tau^+\tau^-$ with the SLL model in EvtGen, the resultant tau daughter kinematics can be compared to those generated with Tauola [45], the program used by KoralB to decay taus. For purposes of the validation, one B^0 is generated and decayed in EvtGen. In 10^6 events, for both Tauola and EvtGen, each tau is required to decay to a e, μ, π or ρ with equal probability. In Tauola the τ^+ polarized randomly to be either $+1$ or -1 and then is decayed with the `DEXAY` subroutine with the requisite momentum for ditau B decay. The τ^- is polarized with the opposite sign and then decayed with `DEXAY`. This produces taus with the same helicity as required for a spin zero decay. The tau daughter momenta and the angle between the tau daughters is plotted in Figures 4.3, 4.4, 4.5 and 4.6. The correlations between tau daughter momenta are shown in Figures 4.7 and 4.8.

Background Simulation: B and D Physics in EvtGen

The B^0 (B^+) meson decays via the weak interaction with a lifetime of $1.548 \pm 0.032\,\mathrm{ps}$ ($1.653 \pm 0.028\,\mathrm{ps}$). The mass of the B^0 (B^+) is approximately $5.2790 \pm 0.0005\,\mathrm{GeV}$ ($5.2794 \pm 0.0005\,\mathrm{GeV}$) which, together with energy conservation, forbids B decays to top mesons but allows decays to charm, strange, up/down mesons and all three leptons. B meson decays may be categorized according to flavor of their decay products: leptonic, semileptonic and hadronic (or non-leptonic). See Figure 4.9 for Feynman diagrams for leptonic, semileptonic, and two body hadronic decays.

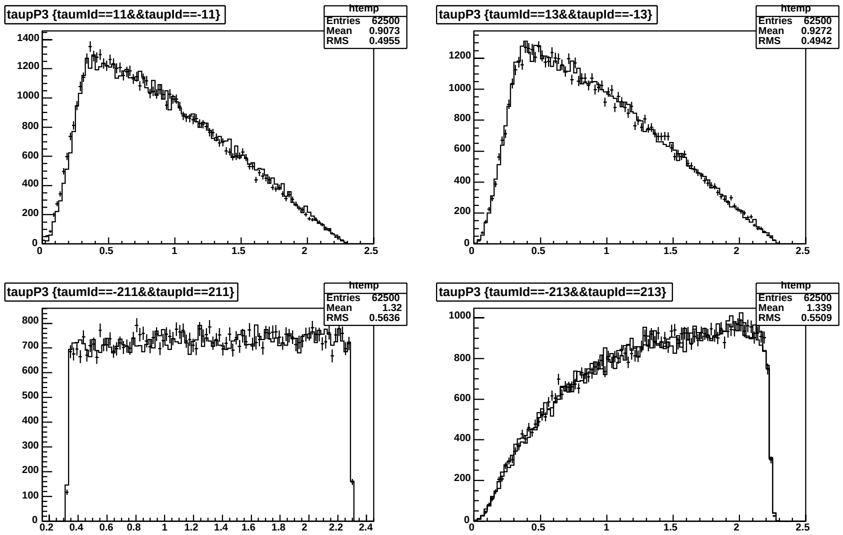

Figure 4.3: Tau momentum in the B frame with EvtGen (solid line) and Tauola (error bars). Clockwise from top left are $\tau\tau \rightarrow ee\nu_e\bar{\nu}_e\nu_\tau\bar{\nu}_\tau$, $\tau\tau \rightarrow \mu\mu\nu_\mu\bar{\nu}_\mu\nu_\tau\bar{\nu}_\tau$, $\tau\tau \rightarrow \rho\rho\nu_\tau\bar{\nu}_\tau$ and $\tau\tau \rightarrow \pi\pi\nu_\tau\bar{\nu}_\tau$. For the ρ mode, the EvtGen results using TAUHADNU and TAUVECTORNU are superimposed.

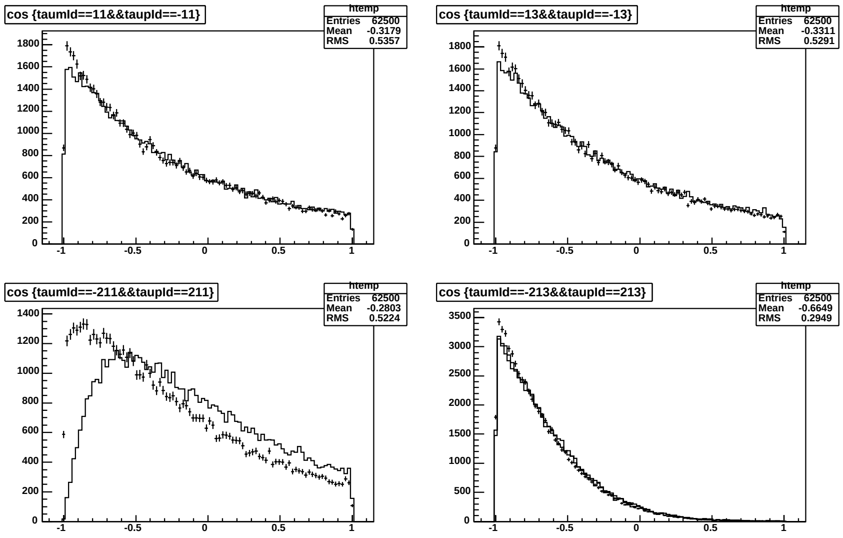

Figure 4.4: Cosine of the angle between tau daughters in the B frame with EvtGen (solid line) and Tauola (error bars). Clockwise from top left are $\tau\tau \rightarrow ee\nu_e\bar{\nu}_e\nu_\tau\bar{\nu}_\tau$, $\tau\tau \rightarrow \mu\mu\nu_\mu\bar{\nu}_\mu\nu_\tau\bar{\nu}_\tau$, $\tau\tau \rightarrow \rho\rho\nu_\tau\bar{\nu}_\tau$ and $\tau\tau \rightarrow \pi\pi\nu_\tau\bar{\nu}_\tau$. For the ρ mode, the EvtGen results using TAUHADNU and TAUVECTORNU are superimposed.

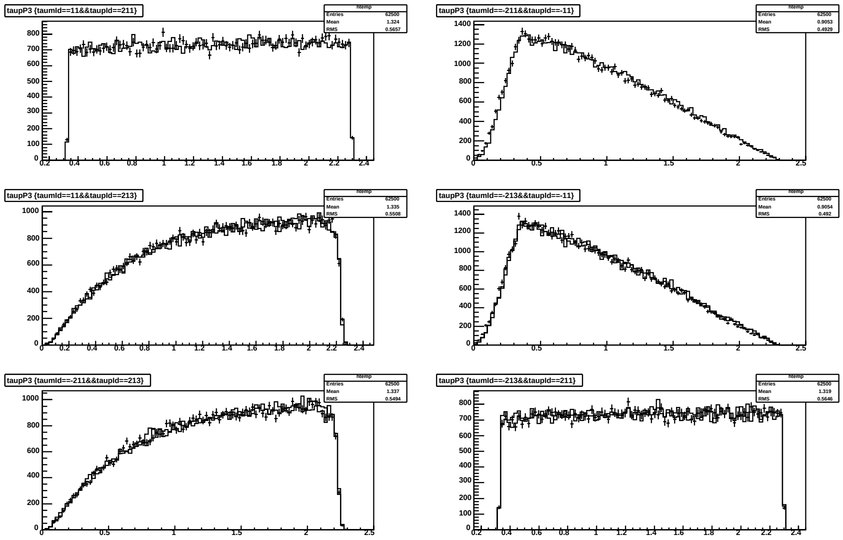

Figure 4.5: Tau momentum in the B frame with EvtGen (solid line) and Tauola (error bars). From top to bottom are $\tau\tau \to e\pi\nu_e\nu_\tau\bar{\nu}_\tau$, $\tau\tau \to e\rho\nu_e\nu_\tau\bar{\nu}_\tau$ and $\tau\tau \to \pi\rho\nu_\tau\bar{\nu}_\tau$. Charge conjugate modes are horizontally opposed. Charge conjugate modes are horizontally opposed. For the ρ mode, the EvtGen results using TAUHADNU and TAUVECTORNU are superimposed.

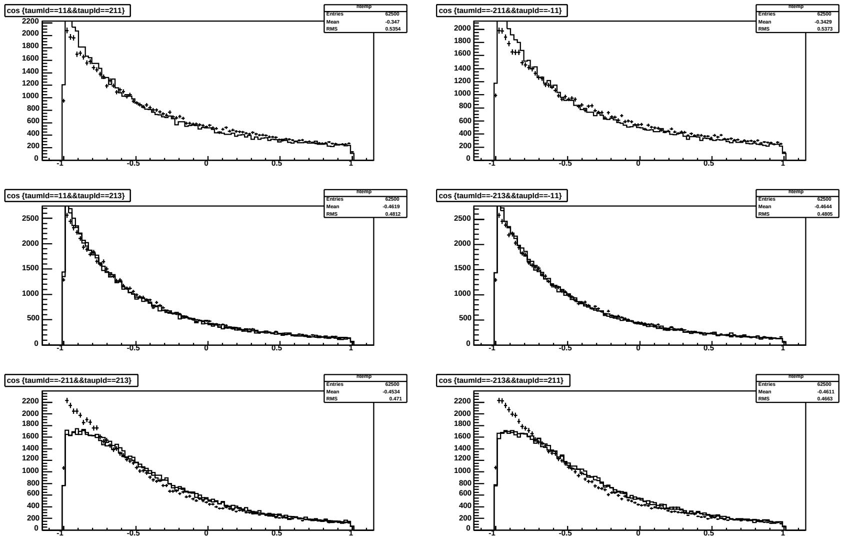

Figure 4.6: Cosine of the angle between tau daughters in the B frame with EvtGen (solid line) and Tauola (error bars). From top to bottom are $\tau\tau \to e\pi\nu_e\nu_\tau\bar{\nu}_\tau$, $\tau\tau \to e\rho\nu_e\nu_\tau\bar{\nu}_\tau$ and $\tau\tau \to \pi\rho\nu_\tau\bar{\nu}_\tau$. Charge conjugate modes are horizontally opposed. For the ρ mode, the EvtGen results using TAUHADNU and TAUVECTORNU are superimposed.